A Thesis for the Degree of Ph.D. in Engineering

Electrodeposition of Cadmium and Selenium in 1-Butyl-1-methylpyrrolidinium Bis(trifluoromethylsulfonyl)amide Ionic Liquid

August 2016

Graduate School of Science and Technology
Keio University

SAHA, Shimul

Abstract

Aprotic room-temperature ionic liquids (RTILs) have gained significant attention as a medium for electrodeposition of metals and alloys due to their several attractive properties. Among aprotic RTILs, 1-butyl-1-methylpyrrolidinium bis(trifluoromethylsulfonyl)amide (BMPTFSA) is one of the promising RTILs for electrodeposition of a wide variety of metals. However, the mechanism of electrodeposition of metals in BMPTFSA has not been revealed in depth. In this study, electrodeposition of cadmium (Cd) and selenium (Se) has been investigated in BMPTFSA with and without the presence of excess chloride.

In chapter 1, the backgrounds of electrodeposition, ionic liquids and electrodeposition of metals and alloys in ionic liquids are introduced briefly.

Chapter 2 explains the general experimental techniques of the present work.

Chapter 3 deals with electrodeposition of cadmium in BMPTFSA. The divalent Cd(II) in BMPTFSA was found to be coordinated by three $TFSA^{-}$ and probably exist as $[Cd(TFSA)_3]^{-}$. Electrochemical reaction of Cd(II)/Cd on a GC electrode was an electrochemically irreversible process, probably involving 2 one-electron transfer steps. The nucleation process and morphology of the electrodeposits were found to be affected by the applied potential under diffusion-controlled region, suggesting the influence of the potential on the electric double layer structure due to the difference in accumulation of cations led to the change in surface processes.

Chapter 4 describes the electrochemical behavior of Se(IV) species in BMPTFSA in the absence and presence of excess chloride. The electrodeposition of metallic Se was possible in BMPTFSA in both absence and presence of excess chloride. $SeCl_4$ was found to be dissolved in the RTIL with excess Cl^{-} by forming $[SeCl_6]^{2-}$. Morphology and crystal structure of Se deposits were found to be related with the temperature. Reduction of Se to Se(–II) was confirmed at the potential more negative than the reduction of $[SeCl_6]^{2-}$. However, proportionation reaction of Se(–II) and $[SeCl_6]^{2-}$ led to deposition of Se.

Chapter 5 is concerned with electrochemical behavior of Cd(II) species in BMPTFSA in the presence of excess chloride. Cyclic voltammograms of $[CdCl_4]^{2-}$ showed unusual electrochemical behavior, regardless of electrode materials and ionic liquids, probably related to the adsorption of BMP^{+} on the electrode surface. The

possibility of electrodeposition of CdSe alloy was also examined in BMPTFSA containing both $[CdCl_4]^{2-}$ and $[SeCl_6]^{2-}$.

Chapter 6 summarizes the results obtained in this study and describes the perspectives of electrodeposition of metals and alloys using BMPTFSA.

Table of Contents

List of Symbols Used in this Thesis

Symbol	Meaning
C	Concentration
D	Diffusion coefficient
$E^{0'}$	Formal potential
E_p	Cathodic peak potential
F	Faraday constant
I_f	Integrated intensity of free TFSA^- in the bulk
j	Current density
n	Number of electrons involved in an electrode reaction (except eq. 3.1, where n is the number of TFSA^- bound to Cd(II))
n_a	Number of electrons involved in an electrode reaction in the rate-determining process
R	Gas constant
t	Time
T	Absolute temperature
ε_f	Molar absorption coefficient
α	Transfer coefficient
l	Effective path length
k^0	Heterogeneous rate constant
v	Scan rate
χ_s	Crystallite size
λ	Wavelength of X-ray (0.154 nm)
θ	Diffraction angle

Chapter 1

General Introduction

1.1.1 Electrodeposition

Electrodeposition, a branch of electrochemistry, refers to a film growth process which consists in the formation of a metallic coating onto a base material occurring through the electrochemical reduction of metal ions from an electrolyte. Electrodeposition is also known as electrolytic deposition or electroplating.[1]

Electrodeposition of metals is one of the most fascinating domains of current research because of its technological importance for manifold applications, which *inter alia*, includes: corrosion-resistant, electronic, optic and sensor materials, automobile, aerospace systems, and so on. The modern electrodeposition technology has a long and productive history. The early history of electrodeposition may be traced back to around 1800. It is widely recognized that in 1803 Luigi Brugnatelli, first electrodeposited gold.[2] By 1839, however, scientist in Britain as well as in Russia had independently devised copper deposition process similar to those of Luigi Brugnatelli. With the increased understanding of the subject of electrochemistry and its importance, the ability to electrodeposit various metals was significantly improved. By 1850s electrodeposition methods of bright nickel, brass, tin, and zinc were commercialized and were applied for engineering and specific commercial purposes.[3] Although several physical and chemical methods, such as physical vapor deposition (PVD), chemical vapor deposition (CVD), atomic layer deposition (ALD) and sputtering have been realized for thin film deposition of metals and alloys, electrodeposition technique nowadays is still expanding in scope and is finding more and more usage in the production of a variety of goods and services due to various advantages of this technique (shortly described below) over the other techniques.[4,5]

1.1.2 Advantages of Electrochemical Technique

The main advantages of electrodeposition technique over other deposition techniques are as follows:

Simplicity and scalability: The electrodeposition is usually carried out in normal laboratory condition without requiring any special atmospheric condition. Due to such simplicity, electrodeposition can be carried out using large tanks as electrolytic cells and therefore large-area thin films can be produced.

Cost effectiveness: The most attractive feature of electrodeposition technique is its cost effectiveness. The cell construction and peripheral equipment are generally simple and, if properly designed, inexpensive. Therefore, electrodeposition offers the production of good quality product at relatively low cost compared to other techniques.

Tuning efficiency: The properties of the deposited film such as thickness, crystallographic orientation, composition and mass can be controlled easily by varying the deposition parameters. Electrodeposition technique also provides scope to synthesis nanoparticles with controlled characteristics.

Band-gap engineering: It is also possible to engineer the bandgap of alloy semiconductors. Such engineering therefore enables the effective absorption of a major part of the solar spectrum using multilayer graded band-gap structures.

1.1.3 An Overview on Electrodepostion Process

Electrodeposition is analogous to a galvanic cell acting in reverse. Electrochemical deposition of metals and alloys involves the reduction of metal ions from aqueous, organic, and fused salt (ionic liquid) electrolytes. At the earlier stage of electrodeposition, two-electrode, cathode and anode, electrolytic cells were used as shown in Figure 1.1 (a).

The deposition of a metal onto a substrate (cathode) is achieved by immersing it into a solution, which contains a salt of the metal to be deposited and applying a negative charge on the substrate to be coated. In appropriate condition, the metal ions receive electrons from the negatively charged substrate. The electroreduction of metal ion, M^{x+}, can be represented as:

$$M^{x+}_{\text{electrolyte}} + ne^{-} \rightarrow M_{\text{lattice}} \qquad (1.1)$$

For the process represented by eq. 1.1, it is necessary to consider four types of fundamental subjects; (1) metal (working electrode)–solution interface where the deposition process takes place, (2) kinetics and mechanism of the deposition process, (3) nucleation and growth processes of the metal lattice ($M_{lattice}$), and (4) structure and properties of the deposits.[6]

On the other hand, there are two kinds of anodes; (1) sacrificial or consumable anode and (2) non-consumable anode. If the anode is made of the metal to be coated and gradually dissolves into the electrolytic solution, then the anode is called a sacrificial or consumable anode. The anode is also known as a counter/auxiliary electrode. Although such two-electrode electrochemical cell arrangement is a viable setup, it has a number of shortcomings. Most significantly, during potentiostatic electrodeposition the potential of the counter electrode changes readily as the counter electrode needs to pass current to the working electrode at the same time. In order to minimize this problem, the role of supplying electrons and referencing potential has been divided between two separate electrodes; a counter and reference electrode. The reference electrode is a half-cell with a known potential. Its only role is to act as reference in measuring and controlling the potential of the working electrode. The counter electrode passes all the current needed to balance the current observed at the working electrode. These working, reference, and auxiliary electrodes make up the classical three-electrode system as shown in Figure 1.1 (b).

The electrodeposition process is known to be greatly affected by the structure of working electrode–solution interface and the surface of the working electrode. In aqueous system the working electrode–solution interface structure has been shown experimentally to behave like a capacitor. The metal working electrode is made up of a lattice of positive ions and free electrons. At a given potential, there will be an excess charge on the working electrode surface (could be positive or negative). The excess charge on the electrode surface is known to be counterbalanced by an equal amount of oppositely charged ions in the solution side. Therefore, the electrode–solution interface structure becomes comparable with a capacitor and known as “electric double layer” structure as shown in Figure 1.2. Several layers make up the solution side of the electric double layer. The first layer is generally occupied by the solvent molecules and some "specifically adsorbed” anions. The locus of the electrical centers of the specifically adsorbed ions is known as *inner Helmholtz plane* (IHP). The second layer is made up by solvated ions and the locus of the electrical centers of the solvated ions is known as *outer Helmholtz plane* (OHP).

Electrodeposition process occurs through individual atomistic process as represented by eq. 1.1. The atomistic process largely depends on the electrode surface condition. The real electrode surface is different from that of ideal one. An ideal electrode surface exhibits no surface defects whereas, a real electrode surface has a variety of defects like, steps, kinks, vacancies, and clusters of ad-atoms as shown in Figure 1.3. A metal species is reduced to its metal ad-atom and the metal ad-atom is adsorbed on the electrode surface at terraces, steps or kinks of the electrode surface. It is generally assumed that the ad-atoms are attached to the crystal via a kink site. Therefore, the ad-atoms adsorbed on the electrode surface at a position other than kinks diffuse on the surface towards kinks. Thus, the state of the electrode surface is very important in electrodeposition process and can play a vital roll on the morphology of the deposit.

1.1.4 Electrodepostion Media-Choice of Ionic Liquid

There are several factors, such as nature of the solution, bath composition, temperature, solution concentration, current density, current wave form, presence of additives, physical and chemical nature of substrate surface, that affect the electrodeposition process as well as the morphology, composition and crystal structure of the electrodeposited metal.

Among them, the solvent is one of the most important factors to be considered in electrodeposition process, as electrodeposition is a solvent-based technique. From the beginning of electrodeposition technique, water has been used as the most common solvent. Certainly, water has been used till now for several advantages such as non-flammability, high solubility of metal salts, high conductivity and low viscosity. Nevertheless, use of aqueous solutions for the electrodeposition process ultimately faces some unavoidable drawbacks:[3]

1. The most common limitation is its relatively narrow electrochemical potential window. After a certain value of negative potential, water itself was reduced and therefore, metals having more negative reduction potentials than water cannot be electrodeposited from aqueous solution.
2. During electrodeposition from aqueous solutions, hydrogen evolution is the second reaction at the cathode. In some cases, it can be ignored while in other cases it cannot. Hydrogen evolution results in hydrogen embrittlement, which

consequently deteriorates the electrodeposited film and decreases the current efficiency.

Some other problems, such as electrode passivation, necessity of complexing agents and low thermal stability, are also often encountered. With a view to overcoming these problems, researchers have searched for new non-aqueous solvents to electrodeposit materials. Although electrodeposition of metals from non-aqueous solvents has been practiced from the end of 18th century,[7] electrodeposition in non-aqueous solvents has been studied extensively for last few decades.

There are a range of non-aqueous solvents that could be used for electrodeposition of metals. Practically, polar molecules are desirable to be used as an electrolyte solution. Electrodeposition of several metals and alloys has been reported from various organic solvents.[8,9] Recently, there have been concerns that many organic solvents are toxic or hazardous to human health and/or to the environment. Many of the commonly used organic solvents are known as volatile organic compounds (VOCs) and therefore, triggering several environmental problems by their evaporation. In recent years, numerous efforts have been made to avoid the toxic solvents and gradually the environmentally hazardous solvents are being replaced by harmless ones.

Besides classical molecular solvents, a salt melted down (‘liquefied’) by providing heat, to counterbalance the salt lattice energy, can also be used as an alternative electrodeposition medium. Such systems are usually known as molten salts. In general, molten salts are liquids (like water), having good heat capacity, high thermal stability, high ionic conductivity, and wide electrochemical potential windows.[2,8] However, high temperature molten salts clearly suffer from the major limitation that the operational conditions are difficult to be achieved. Therefore, ionic substances that melt at a low temperature have drawn significant attention and the term “ionic liquids” is generally used to distinguish these lower temperature molten salts from the high temperature analogues.

1.2.1 Ionic Liquid

Ionic liquids (ILs) are, quite simply, liquids that are comprised entirely of ions.[10] By careful choice of the starting materials, it is possible to prepare ionic liquids that are liquid at and below room temperature.[11,12] Such ionic liquids are known as room temperature ionic liquids (RTILs) nowadays, although there is no universal agreement upon the definition. In our present study, aprotic RTILs have been used. Therefore, discussion on ILs in the following sections has been made focusing aprotic RTILs.

Although research in ionic liquids has been expanding from the last few decades, historically ionic liquids are not new. In general, it is well accepted that the first report on an ionic liquid was, by Walden in 1914, the synthesis of ethylammonium nitrate, $[C_2H_5NH_3]NO_3$, with a melting point of 12°C.[13] After that, Hurley and Weir[14,15] stated that a room temperature ionic liquid could be prepared by mixing aluminum chloride ($AlCl_3$) and 1-ethylpyridinium halides, mainly the bromide, at a mole fraction of $X(AlCl_3) = 0.66$ (1:2 ratio). In 1978, Osteryoung et al.[16] and Hussey et al.[17] reported the synthesis of ionic liquids, known as all chloride system, by mixing 1-butylpyridinium chloride and aluminium chloride. This ionic liquids were liquid at room temperature over a composition range from $X(AlCl_3) = 0.66$ to 0.43. In 1970s and 1980s, several researchers carried out extensive research on chloroaluminate ($AlCl_3$)-based ionic liquids. The Lewis acidity of these $AlCl_3$-based ionic liquids can be adjusted by changing the mole fraction of $AlCl_3$. If the mole fraction of $AlCl_3$, $X(AlCl_3)$, is > 0.5, the mixture is acidic due to the presence of extra $AlCl_3$ (Lewis acid) which consequently forms $[Al_2Cl_7]^-$. If the mole fraction of $AlCl_3$, $X(AlCl_3)$, is < 0.5, the mixture is basic due to the presence of R^+Cl^- (Lewis base) (R^+ is the organic cation of the relevant IL). If the mole fraction of $AlCl_3$, $X(AlCl_3)$, is = 0.5, the mixture is regarded as neutral. However, the hygroscopic nature of $AlCl_3$-based ionic liquids has limited their use in many applications since they must be prepared and handled under inert gas atmosphere. Thus, the synthesis of air- and water-stable ionic liquids attracted further interest in the use of ionic liquids in various fields. In 1992, Wilkes and Zaworotko[18] reported the synthesis of non-chloroaluminate ionic liquids based on 1-ethyl-3-methylimidazolium cation. They used nitrate (NO_3^-), nitrite (NO_2^-), sulfate (SO_4^{2-}), methyl carbonate ($CH_3CO_2^-$), and tetrafluoroborate (BF_4^-) anions, alternatively. Since then, a wide range of non-chloroaluminate ionic liquids have been developed by altering the combination of cations and anions. Later, ILs based on water- and moisture-stable hydrophobic anions, such as bis(trifluoromethanesulfonyl)amide, $(CF_3SO_2)_2N^-$, and their derivatives, have been developed.[19,20] Yet, altering the combination of cation and anion, or even modifying the nature of one or more alkyl chains on a single class of cation, the possibility of fine tuning of the solvent properties of ILs to the particular task is a highly expanding area of research.

1.2.2 Electrochemical Aspects of Ionic Liquids

ILs possess a set of unique properties that make them very attractive for electrochemical studies. Some of the important basic properties of ILs are presented in the following sections.

1.2.2.1 Electrochemical Window

For electrochemical applications, the potential window of the electrolyte solution is one of the most important properties. By definition, the electrochemical window is the potential range over which the electrolyte is neither reduced nor oxidized at an electrode. This value determines the electrochemical stability of the solvents. The potential window is determined not only by the chemical structure of the solvent used but also by the electrode materials, such as sweep rate of potential, temperature, atmosphere, and impurity. A series of potential windows and the conditions of measurement for a series of ILs have been reported and reviewed by some pioneering researchers in IL research field.[2,11,21] In general, the potential windows of aprotic RTILs are larger compared to that of conventional aqueous system, for example the potential windows are; about 4 V for 1-ethyl-3-methylimidazolium tetrafluoroborate ($EMIBF_4$),[22] 4.1 V for 1-butyl-3-methylimidazolium tetrafluoroborate ($BMIBF_4$),[23] 4.15 V for 1-butyl-3-methylimidazolium hexafluorophosphate ($BMIPF_6$),[23] about 5.5 V for 1-butyl-1-methylpyrrolidinium bis(trifluoromethylsulfonyl)amide (BMPTFSA),[24] 5.8 V for 1-methyl-1-propylpiperidinium bis(trifluoromethylsulfonyl)amide ($PP_{13}TFSA$).[25] Even, ionic liquid with a potential window of 7 V has also been reported.[26] Due to their large electrochemical potential windows compared with aqueous and conventional organic media, aprotic RTILs have been explored as an attractive alternative medium for electrochemical studies.

1.2.2.2 Viscosity

The viscosity of an ionic liquid is an important consideration in electrochemical studies due to its strong effect on the rate of mass transport. There are some basic studies and reviews on the viscosity of ILs in the literature.[3,11,27] The viscosity of ILs is typically 10 to 100 times higher than that of water or organic solvents as a result of the strong electrostatic and other interactions like van der Waals forces and hydrogen bonding. However, in general, all ILs show a significant decrease in viscosity with an increase in temperature.

1.2.2.3 Ionic Conductivity

As like other media employed in an electrochemical process, the conductivity of ionic liquids is of vital importance. Although ILs have reasonably good ionic conductivities when compared with those of organic solvents/electrolyte systems,[11] at room temperature their conductivities are usually lower than those of concentrated aqueous electrolytes. As RTILs are composed entirely of ions, high conductivity might initially be predicted. However, the conductivity of any system depends not only on the number of charge carriers but also on their mobility, and the large size of ions of ILs reduces the ion mobility, leading to lower conductivities. Furthermore, high coulombic interaction between the ions of the ILs may also be a reason behind their low ionic conductivity.

1.2.2.4 Density

Since ILs are composed only of ions; almost all ILs in general are denser than water with values ranging from 1 to 1.6 g cm^{-3}. The densities of imidazolium-based RTILs has been found to decrease with increasing alkyl chain length on the imidazolium cation.[28] Similarly, in the ammonium and sulfonium salts, the density decreases with increasing alkyl chain length. Therefore, the density of ILs is tunable to some extent. The densities of ILs are also affected by the type of anions.

1.2.2.5 Thermal Stability

The thermal stability of ILs is known to vary with the constituent cation and anion. It has been mentioned that the thermal stability of ILs is limited by the strength of their heteroatom–carbon and their heteroatom–hydrogen bonds.[29] High thermal stability of several RTILs has been also reported, for example, Wilkes et al.[30] reported that $EMIBF_4$, $BMIBF_4$ and 1,2-dimethyl-3-propylimidazolium bis(trifluoromethylsulfonyl)amide (DMPITFSA) are stable up to temperatures of 445, 423 and 457°C, respectively. However, Endres et al.[31] mentioned that such high temperatures are only tolerated by most liquids for a short time and that long time exposure to such high temperatures inevitably leads to decomposition.

1.2.3 Advantages of Ionic Liquid for Electrodeposition

In the previous section, some important properties of RTILs have been discussed shortly. Such properties introduce RTILs as an excellent alternative medium for electrochemical studies. However, in order to use RTILs as electrodeposition medium instead of conventional aqueous or organic media, it is necessary to have a look on the advantages of using RTILs for electrodeposition of metals and alloys. The key advantages are mentioned below:

Wide potential windows: Electrodeposition of a range of metals, *e.g.* Al, Ti, Ta, Nb, Mo, and W, is impossible from water due to decomposition. Since aprotic RTILs have wide electrochemical potential window, they offer the potential to deposit these metals.

Free from hydrogen embrittlement: Hydrogen embrittlement during metallic coatings using aqueous solvents often becomes a serious problematic issue to be overcome. Since aprotic RTILs are non-aqueous system, there is negligible hydrogen evolution during electroplating and therefore, the coatings possess much superior mechanical properties of the pure metal.

High thermal stability: Due to high thermal stability, ionic liquids can be used in a wide range of temperature. On the other hand, electrodeposition at high temperature provides scope to accelerate the electrodeposition process such as mass transfer, charge transfer, nucleation, surface diffusion and crystallization. Thus, control over the morphology and crystalline structure of the deposit can be achieved by using ionic liquids as the medium for electrodeposition of metals.

Possibility of alloy and nano-deposition: Metals have significantly different reduction potentials in IL systems compared to water. One consequence of this characteristic is that some noble alloys may be electrodeposited easily from IL systems. Moreover, nano-crystalline metals and alloys can be deposited from RTILs by adjusting the deposition parameters.

Acceptable viscosity and conductivity: Although, the viscosity of ILs is higher than that of water or organic solvents and the conductivity is lower than those of conventional aqueous and organic solvents at room temperature, most of the values are within acceptable range for performing electrodeposition of metals and alloys. Also, the viscosity and the conductivity can be adjusted by increasing the bath temperature. Moreover, viscosity and conductivity can be tuned by changing the combination of cation and anion, and hence mass transport of metal ions to the electrode surface can be controlled.

1.3 Electrodeposition from Ionic Liquid

RTILs are being used as an electrolyte for electrodeposition over the last several decades. The first experiment using RTIL as an electrolyte was the electrodeposition of aluminium from $AlCl_3$-based ionic liquid by Hurley and Wier in 1950s.[14,15] From then a large number of studies on eletrodeposition of metals from chloroaluminate-type ionic liquid have been reported. Although, historically chloroaluminate ionic liquids have been used for electrodeposition of various metals and alloys, electrodeposition from chloroaluminate ILs suffers from several disadvantages. The principal drawback of chloroaluminate RTILs is their very high sensitivity to atmospheric moisture. Additionally, co-deposition of aluminum during electrodeposition of metals is often unavoidable.

Therefore, non-chloroaluminate hydrophobic RTILs have been explored as a more practical choice for the electrodeposition of a variety of metals. These ILs have received extensive attention because of not only their low reactivity with water and moisture, but also their large electrochemical windows. Until now, a wide ranges of metals have been electrodeposited from a number of RTILs. There are several review articles and books regarding the electrodeposition of metals from ionic liquids by some pioneering researchers in the field of ionic liquid.[3,31,21,32–35] In the Figure 1.4, a summary of electrodeposited single metals and alloys has been shown on the basis of previous reports.

1.4 Objective of this Study

From the above discussion, it is clear that aprotic RTILs have gained significant attention to the researchers as a medium for electrodeposition of metals and alloys due to their several attractive properties as discussed above. Among aprotic RTILs, the ILs having bis(trifluoromethylsulfonyl)amide ($TFSA^-$) as an anion are known as typical hydrophobic ionic liquids. They are relatively more stable against moisture and less miscible with water compared to the ILs based on BF_4^-, PF_6^- and $CF_3SO_3^-$ anoins.[19,32,36] Thus, $TFSA^-$ anion-based molten salt systems can be a good choice for various electrochemical processes including electrodeposition. Especially, the $TFSA^-$ anion-based IL of 1-butyl-1-methylpyrrolidinium (BMP^+) cation is one of the promising RTILs because of its wide electrochemical potential window, low melting point and low viscosity. [20,24,37] The structure of BMPTFSA has been shown in the figure 1.5.

However, the mechanism of electrodeposition of metals in BMPTFSA has not been studied in depth. In order to use ionic liquids for practical electrodeposition processes, the fundamental knowledge, like the redox reaction of the metal ion species, the double layer structure between the electrodes and the ionic liquids, the nucleation and growth mechanisms of the metals and the state of the metal ions in the ionic liquids should be studied in details.

Fundamental electrochemical behavior and morphological tunability of several metals in BMPTFSA have already been reported in our research group. As a continuity of this research, and of course due to several attractive properties and practical uses, exploring the electrochemical behavior of cadmium (Cd) and selenium (Se) species in BMPTFSA was the initial purpose of the present study.

A detail electrochemical investigation of Cd(II) and Se(IV) species in BMPTFSA in the presence of excess chloride ion was attempted. Along with electrochemical studies, solvation states of Cd(II) and Se(IV) species in BMPTFSA were also studied as it is well known that electrochemical behavior of the examining species is directly related to its coordination environment.

Moreover, morphology and crystal structure are very important characteristics, which influence several properties of the deposits. In the present study, effect of applied current and potential on the morphology and crystal structure of deposited Cd and the effect of temperature on Se deposition have been discussed.

The use of cadmium selenide (CdSe) thin film in photovoltaic cells is well known. The possibility of synthesizing CdSe alloys in BMPTFSA in the presence of excess chloride ion was the ultimate purpose of the present study.

1.5 Outline of this Thesis

Chapter 2 explains the general experimental techniques of the present work. Synthesis and evaluation of BMPTFSA was described in details. Construction of the electrochemical cell was also discussed in chapter 2.

In chapter 3, electrodeposition of cadmium was performed from the hydrophobic RTIL, BMPTFSA. The coordination environment of Cd(II) in this ionic liquid was investigated by FT-IR spectroscopy. Redox behavior of Cd(II) species was studied by cyclic voltammetric technique. The diffusion coefficient of the metal complex was calculated and nucleation and/or growth mechanism of Cd electrodeposition in the ionic liquid was analyzed from chronoamperometric results. Galvanostatic and potentiostatic electrodeposition of metallic Cd at several current density and potential was performed and the morphology of the deposits was compared.

Chapter 4 describes the electrochemical behavior of Se(IV) species in BMPTFSA in the absence and presence of excess chloride. Electrochemical behavior of Se(IV) species was studied by cyclic voltammetric technique. The diffusion coefficient of the selenium species in BMPTFSA in the absence of excess chloride was calculated from cyclic voltammetric and chronoamperometric results. The coordination environment of Se(IV) in BMPTFSA in the presence of excess chloride was investigated by Raman spectroscopy. Morphology and crystal structure of the electrodeposited selenium obtained at different temperatures were characterized by several analytical techniques.

In chapter 5, electrochemical behavior of Cd(II) species was studied in BMPTFSA in the presence of excess chloride. Several kinds of working electrode and also a different type of RTIL, 1-butyl-3-methylimidazolium bis(trifluoromethylsulfonyl)amide (BMITFSA), were employed to understand the redox behavior of Cd(II) species. The possibility of electrodeposition of CdSe alloy was also examined in BMPTFSA.

Chapter 6 summarizes the results obtained in this study and describes the perspectives of electrodeposition of metals and alloys using BMPTFSA.

1.6 References

1. Y. D. Gamburg and G. Zangari, *Theory and Practice of Metal Electrodeposition*, Springer Science+Business Media, LLC, New York, (2011).
2. L. B. Hunt, *Gold Bull.*, **6**, 16–27 (1973).
3. F. Endres, D. MacFarlane, and A. Abbott, Eds., *Electrodeposition from Ionic Liquids*, Wiley-VCH Verlag GmbH & Co. KGaA, Weinheim, (2008).
4. W. Schwarzacher, *Electrochem. Soc. Interface*, 32–35 (2006).
5. I. M. Dharmadasa and J. Haigh, *J. Electrochem. Soc.*, **153**, G47–G52 (2006).
6. M. Paunovic and M. Schlesinger, *Fundamentals of Electrochemical Deposition*, 2nd ed., John Wiley & Sons, Inc., Hoboken, New Jersey, (2006).
7. L. F. Audrieth and H. W. Nelson, *Chem. Rev.*, **8**, 335–352 (1931).
8. W. Simka, D. Puszczyk, and G. Nawrat, *Electrochim. Acta*, **54**, 5307–5319 (2009).
9. K. Izutsu, *Electrochemistry in nonaqueous solutions*, Wiley-VCH Verlag GmbH & Co. KGaA, Weinheim, (2002).
10. K. R. Seddon, *J. Chem. Technol. Biotechnol.*, **68**, 351–356 (1997).
11. P. Wasserscheid and T. Welton, Eds., *Ionic Liquids in Synthesis*, Wiley-VCH Verlag GmbH & Co. KGaA, Weinheim, (2002).
12. T. Welton, *Chem. Rev.*, **99**, 2071–2084 (1999).
13. P. Walden, *Bull. Acad. Imper. Sci. (St. Petersburg)*, **8**, 405–422 (1914).
14. F. H. Hurley and T. P. Wier, *J. Electrochem. Soc.*, **98**, 203–206 (1951).
15. F. H. Hurley and T. P. Wier, *J. Electrochem. Soc.*, **98**, 207–212 (1951).
16. R. J. Gale, B. Gilbert, and R. A. Osteryoung, *Inorg. Chem.*, **17**, 2728–2729 (1978).
17. J. C. Nardi, C. L. Hussey, and L. A. King, 4,122,245 (1978).
18. J. S. Wilkes and M. J. Zaworotko, *J. Chem. Soc. Chem. Commun.*, **04**, 965–967 (1992).
19. P. Bonhote, A. P. Dias, N. Papageorgiou, K. Kalyanasundaram, and M. Gratzel, *Inorg. Chem.*, **35**, 1168–1178 (1996).
20. D. R. MacFarlane, P. Meakin, J. Sun, N. Amini, and M. Forsyth, *J. Phys. Chem. B*, **103**, 4164–4170 (1999).
21. H. Ohno, Ed., *Electrochemical Aspects of Ionic Liquids*, John Wiley & Sons, Inc., New Jersey, (2005).
22. Y. Katayama, S. Dan, T. Miura, and T. Kishi, *J. Electrochem. Soc.*, **148**, C102–C105 (2001).

23. U. Schroder, J. D. Wadhawan, R. G. Compton, F. Marken, P. A. Z. Suarez, C. S. Consorti, R. F. d. Souza, and J. Dupont, *New J. Chem.*, **24**, 1009–1015 (2000).
24. D. McFarlane, J. Sun, J. Golding, P. Meakin, and M. Forsyth, *Electrochim. Acta*, **45**, 1271–1278 (2000).
25. H. Sakaebe and H. Matsumoto, *Electrochem. commun.*, **5**, 594–598 (2003).
26. N. V. Ignatev, U. W. Biermann, A. Kucheryna, G. Bissky, and H. Willner, *J. Fluor. Chem.*, **126**, 1150–1159 (2005).
27. K. R. Seddon, A. Stark, and M. J. Torres, in *American Chemical Society Symposium Series*,, vol. 819, p. 34–49 (2002).
28. S. V. Dzyuba and R. A. Bartsch, *ChemPhysChem*, **3**, 161–166 (2002).
29. P. Wasserscheid and W. Keim, *Angew. Chemie*, **39**, 3772–3789 (2000).
30. M. E. V. Valkenburg, R. L. Vaughn, M. Williams, and J. S. Wilkes, *Thermochim. Acta*, **425**, 181–188 (2005).
31. F. Endres and S. Zein E. Abedin, *Phys. Chem. Chem. Phys.*, **8**, 2101–2116 (2006).
32. A. P. Abbott and K. J. McKenzie, *Phys. Chem. Chem. Phys.*, **8**, 4265–4279 (2006).
33. A. P. Abbott, G. Frisch, and K. S. Ryder, *Annu. Rev. Mater. Res.*, **43**, 335–358 (2013).
34. Q. Zhang, Q. Wang, S. Zhang, X. Lu, and X. Zhang, *ChemPhysChem*, **17**, 335–351 (2016).
35. M. C. Buzzeo, R. G. Evans, and R. G. Compton, *ChemPhysChem*, **5**, 1106–1120 (2004).
36. J. G. Huddleston, A. E. Visser, W. M. Reichert, H. D. Willauer, G. A. Broker, and R. D. Rogers, *Green Chem.*, **3**, 156–164 (2001).
37. H. Matsumoto, M. Yanagida, K. Tanimoto, M. Nomura, Y. Kitagawa, and Y. Miyazaki, *Chem. Lett.*, **29**, 922–923 (2000).

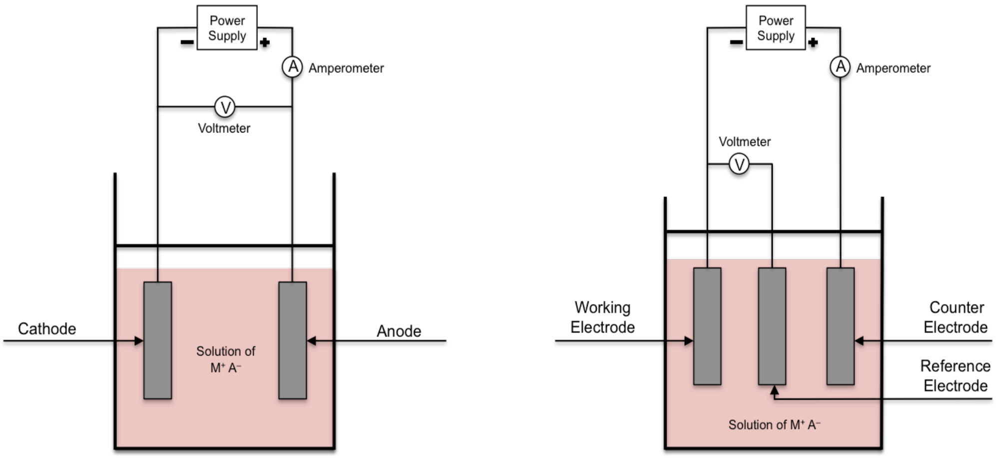

(a) Two electrode / electrolytic cell

(b) Three electrode / electrolytic cell

Figure 1.1: Schematic diagram of (a) two electrode and (b) three electrode cell, for electrodeposition of metal, M, from a solution of metal salt, MA.

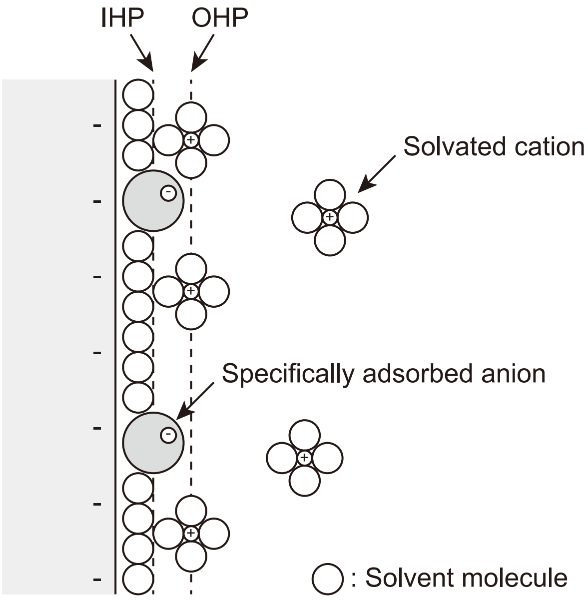

Figure 1.2: Schematic illustration of the electric double layer structure in conventional solvents.

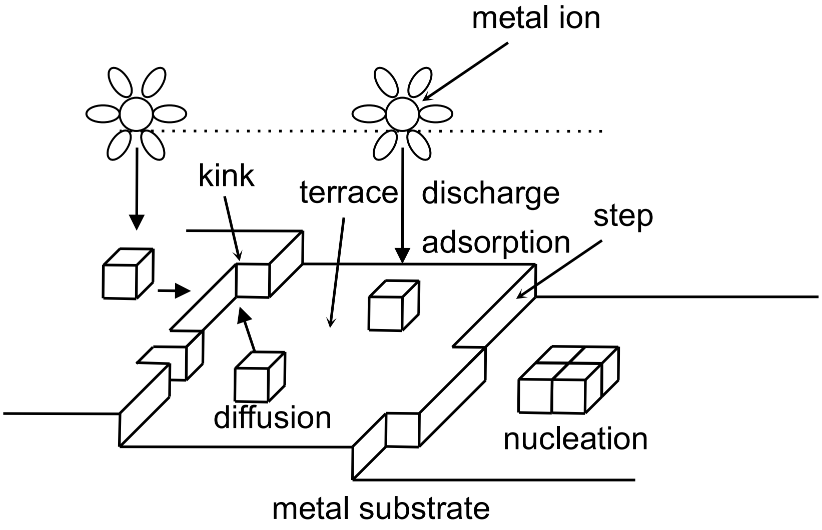

Figure 1.3: Schematic illustration of the real electrode surface and diffusion of metal ad-atoms on the surface.

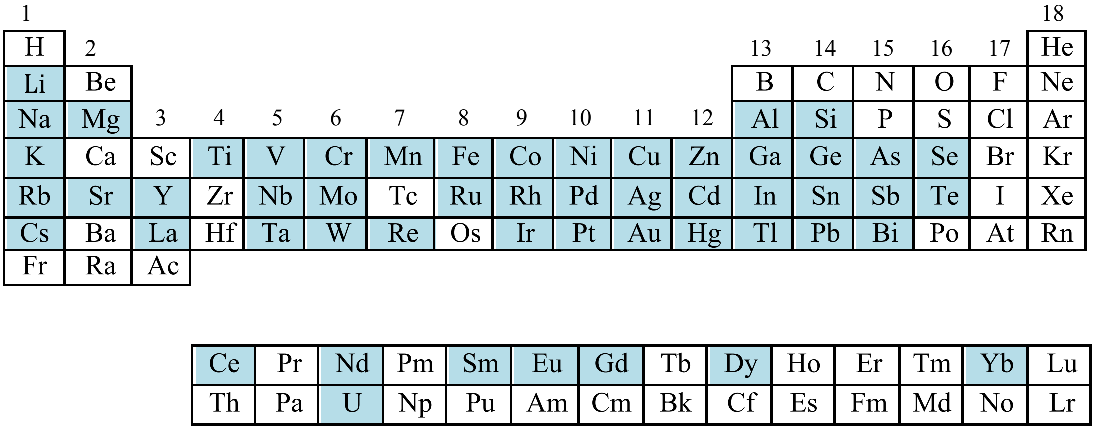

1	2	3	4	5	6	7	8	9	10	11	12	13	14	15	16	17	18
H																	He
Li	Be											B	C	N	O	F	Ne
Na	Mg											Al	Si	P	S	Cl	Ar
K	Ca	Sc	Ti	V	Cr	Mn	Fe	Co	Ni	Cu	Zn	Ga	Ge	As	Se	Br	Kr
Rb	Sr	Y	Zr	Nb	Mo	Tc	Ru	Rh	Pd	Ag	Cd	In	Sn	Sb	Te	I	Xe
Cs	Ba	La	Hf	Ta	W	Re	Os	Ir	Pt	Au	Hg	Tl	Pb	Bi	Po	At	Rn
Fr	Ra	Ac															

Ce	Pr	Nd	Pm	Sm	Eu	Gd	Tb	Dy	Ho	Er	Tm	Yb	Lu
Th	Pa	U	Np	Pu	Am	Cm	Bk	Cf	Es	Fm	Md	No	Lr

Figure 1.4: Summary of elements (colored) electrodeposited as single metals and/or alloys.

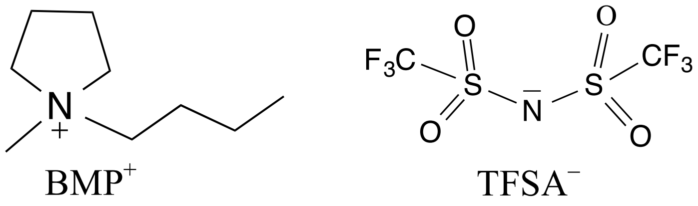

Figure 1.5: Structure of BMPTFSA ionic liquid.

Chapter 2

Materials and General Experimental Techniques

2.1 List of Materials and Reagents

The materials and reagents used in this study have been listed in the Table 2.1.

Table 2.1: List of materials and reagents used in this study.

Material and Reagent	**Company and Purity**
1-Methylpyrrolidine	Tokyo Chemical Industry, >95%
Butyl bromide	Tokyo Chemical Industry, >98%
Acetonitrile	Kanto Chemical, 99.5%
Lithium bis(trifluoromethylsulfonyl)amide (LiTFSA)	Kanto Chemical, 99.7%
Dichloromethane	Junsei Chemical, 99.5%
Cadmium oxide (CdO)	Kanto Chemical, 99%
Selenium tetrachloride ($SeCl_4$)	Alfa Aesar, 99%
Bis(trifluoromethylsulfonyl)amide (HTFSA)	Morita Kagaku, >99%
Silver trifluoromethanesulfonate ($AgCF_3SO_3$)	Aldrich, >99.0%
Cadmium sheet	Nilaco, 99.9%
Platinum wire	Tokuyama Kagaku, 99.9%
Silver wire	Sanwa Kinzoku, >99.5%
Copper rod	Nilaco, 99.9%
Glassy carbon	Tokai Carbon, GC-20SS
Silver paste	Tokuriki
Alumina paste	Baikowski
Alumina powder	Struers

2.2 List of Equipments

The equipments used in this study have been listed in the Table 2.2.

Table 2.2: List of equipments used in this study.

Equipment	Company and Model
Glove box	Miwa MFG, DB0-1K-SH Miwa MFG, DB0-1KP-KO3
Potentiostat/Galvanostat	Hokuto Denko, HABF-501 Hokuto Denko, HSV-110 Ivium Technologies, CompactStat.e
Digital oscillographic recorder	Yokogawa, OR100E
Analytical balance	Mettler Toledo, AB204-S Mettler Toledo, AE240-S
Karl Fischer coulometer	Metrohm, 831 KF Coulometer
Thermogravimetric-differential thermal analyzer (TG-DTA)	Rigaku, Thermoplus 8120
Inductively coupled plasma-optical emission spectrometer (ICP-OES)	Agilent Technologies, 5100
Nuclear magnetic resonance (NMR) spectrometer	JEOL, ECA-500
Ultraviolet-visible (UV-vis) spectrometer	JASCO Corporation, V-530 JASCO Corporation, V-770
Fourier transform-infrared spectroscopy (FT-IR) spectrometer	Shimadzu, IRPrestige-21
Raman spectrometer	Renishaw, InVia Raman Microscope
Ion chromatography system	Shimadzu, LC 20-AT
Scanning electron microscope (SEM)	Keyence, VE-9800
Energy dispersive X-ray analyzer (EDX)	Oxford Instruments, INCA-E250X3K
X-ray diffractometer (XRD)	Rigaku, Miniflex600
X-ray photoelectron spectrometer (XPS)	JEOL, JPS-9010TR
Transmission electron microscope (TEM)	FEI TECNAI Spirit

1. *Glove box*

   Handling of all the hygroscopic reagents was performed in an argon-filled glove box with a continuous gas purification apparatus. The concentrations of H_2O and O_2 in the gas were kept under 0.8 and 1 ppm, respectively.
2. *UV-vis spectrometer*

   The absorption spectra of all the hygroscopic reagents were measured by using an air-tight quartz cell with the light path length of 1 mm.

2.3 Synthesis and Evaluation

2.3.1 Synthesis of 1-Butyl-1-methylpyrrolidinium Bis(trifluoromethylsulfonyl)amide (BMPTFSA)

1-butyl-1-methylpyrrolidinium bromide (BMPBr) was prepared by the reaction of 1-methylpyrrolidine and butyl bromide in dehydrated acetonitrile at room temperature under N_2 atmosphere.[1]

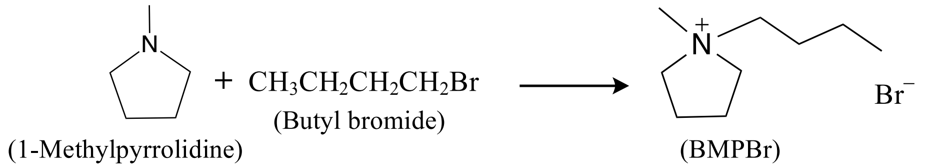

(2.1)

As the formation reaction of BMPBr is exothermic, 1-methylpyrrolidine was diluted with acetonitrile and butyl bromide was added dropwise into the 1-methylpyrrolidine and acetonitrile mixture in order to suppress the elevation of temperature. The schematic illustration of the reaction apparatus was shown in Figure 2.1.

The mixture of 1-methylpyrrolidine and butyl bromide in acetonitrile was kept stirring for about 12 hours at room temperature under N_2 atmosphere in order to complete the reaction. Then the resulted solution was recrystallized by ethyl acetate three times. The final product was dried under vacuum at 100°C for 24 hours and stored in the glove box for further use.

Figure 2.2 shows the ^{1}HNMR spectrum of the synthesized BMPBr. The ^{1}HNMR spectrum showed signals only assignable to BMP^+ cation except very week signals of water and acetone.[2] Acetone-d6 was used as the solvent to dissolve BMPBr. Therefore, the signals corresponding to water and acetone in the ^{1}HNMR spectrum may arise due to acetone-d6.

BMPTFSA was obtained by the metathesis reaction of BMPBr with LiTFSA in deionized water.

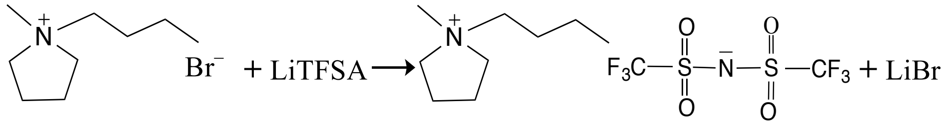

(BMPBr) (BMPTFSA) (2.2)

The mixture of BMPBr and LiTFSA in deionized water was stirred overnight at room temperature until two phases formed. The upper phase was aqueous solution of LiBr and the lower phase was crude BMPTFSA. The water phase was discarded by decantation. BMPTFSA was extracted by an equal volume of dichloromethane and then washed three times with distilled water. The resulting BMPTFSA was dried on a rotatory evaporator for 1 hour at 60°C in order to remove dichloromethane. The residual dichloromethane and water was removed using vacuum line at 100°C for 24 hours. A colorless transparent liquid, BMPTFSA, was obtained and stored in the glove box.

2.3.2 Evaluation of BMPTFSA

Purity of the synthesized BMPTFSA was checked before utilizing it for the experimental purpose. The water content of BMPTFSA was checked by Karl Fischer titration. The water content was typically below 10 ppm. The presence of bromide or other impurities was examined by UV-vis spectroscopy and cyclic voltammetry. Figure 2.3 and 2.4 show the UV-vis absorption spectrum and cyclic voltammorgams of a platinum (Pt) and glassy carbon (GC) electrode of the synthesized BMPTFSA, respectively. The UV-vis absorption spectrum of the synthesized BMPTFSA was similar to that of pure BMPTFSA reported in literature.[3] The cyclic voltammograms of both Pt and GC electrode in BMPTFSA showed that the ionic liquid was stable within a wide potential range. No current due to impurities like Br^-, O_2, H_2O, was observed.[1,4,5] The UV-vis absorption spectrum and the cyclic voltammograms therefore indicated that the purity of the BMPTFSA was acceptable for utilizing it to the experimental purpose.

2.3.3 Synthesis and Evaluation of BMPCl

BMPCl was prepared by the reaction of 1-methylpyrrolidine and butyl chloride in acetonitrile at 75°C for 24 hours.[2] Then the synthesized BMPCl was purified by recrystallization and finally dried under vacuum at 100°C for 24 hours. The procedure of BMPCl synthesis was similar to that of BMPBr.

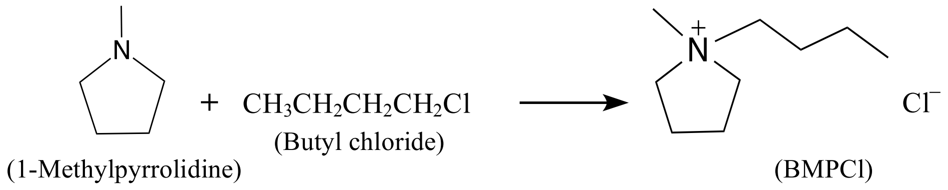

(2.3)

Formation of BMP^+ was confirmed by the ^{1}HNMR spectroscopic analysis of the BMPCl; similar to that of BMPBr (data not shown).

2.4 Electrochemical Measurement

All the electrochemical measurements and electrodeposition experiments were conducted with an air-tight three-electrode cell using potentiostat/galvanostat. For the electrochemical measurements, a glassy carbon (GC) disk electrode (7.07×10^{-2} cm^2), a platinum (Pt) disk electrode (7.07×10^{-2} cm^2) or a cadmium (Cd) disk electrode (3.14×10^{-2} cm^2) was employed as a working electrode after mirror polishing. A platinum wire was used as a counter electrode. A silver wire immersed in BMPTFSA containing 0.1 M $AgCF_3SO_3$ was used as a reference electrode, of which the inner electrolyte was separated from the main electrolyte by porous glass (Vycor). All the potentials in this study were referred to this Ag/Ag(I) electrode. The potential of ferrocenium/ferrocene (Fc^+/Fc) was –0.43 V versus this reference electrode.[6] For the electrodeposition of cadmium, a glassy carbon (1.54 cm^2) substrate after mirror polishing and Cd sheet were used as a working and counter electrode, respectively. The reference electrode was the same as described above. Whereas, the electrodeposition experiments of selenium were conducted with a two-compartment three-electrode cell. A glassy carbon (1.54 cm^2) plate after mirror polishing was used as a working electrode. The counter and reference electrode were same as used for the electrochemical experiments. The counter electrode was placed in the compartment separated from the electrolyte with a membrane filter made of polytetrafluoroethylene (PTFE). Figure 2.6 shows the schematic diagram of the single- and double-compartment electrochemical cells.

2.5 References

1. Y. Katayama, H. Onodera, M. Yamagata, and T. Miura, *J. Electrochem. Soc.*, **151**, A59–A63 (2004).
2. E. E. L. Tanner, R. R. Hawker, H. M. Yau, A. K. Croft, and J. B. Harper, *Org. Biomol. Chem.*, **11**, 7516–7521 (2013).
3. N. Chandrasekhar, F. Endres, and A.-N. Unterreiner, *Phys. Chem. Chem. Phys.*, **8**, 3192–3196 (2006).
4. M. Yamagata, N. Tachikawa, Y. Katayama, and T. Miura, *Electrochim. Acta*, **52**, 3317–3322 (2007).
5. S. Randström, G. B. Appetecchi, C. Lagergren, A. Moreno, and S. Passerini, *Electrochim. Acta*, **53**, 1837–1842 (2007).
6. Y. Yamato, Y. Katayama, and T. Miura, *J. Electrochem. Soc.*, **160**, H309–H314 (2013).

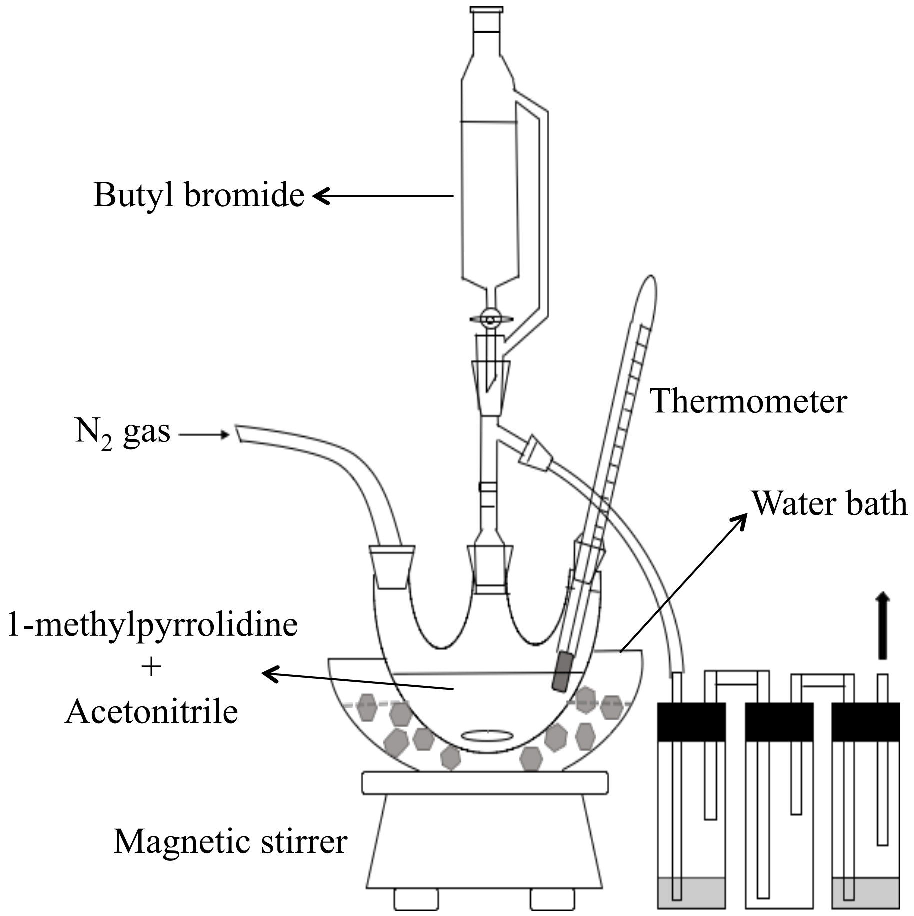

Figure 2.1: Schematic illustration of the apparatus for synthesis of BMPBr.

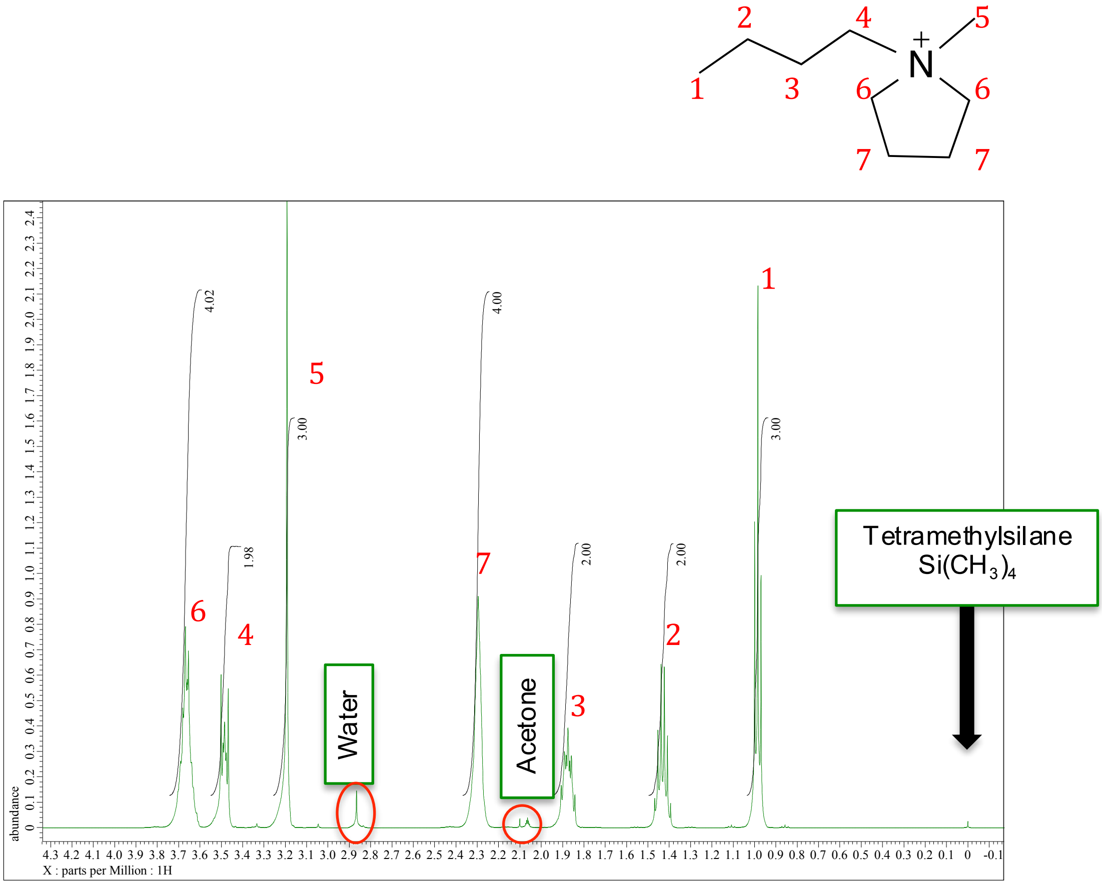

Figure 2.2: ^{1}HNMR spectrum of BMPBr. Solvent: Acetone-d6.

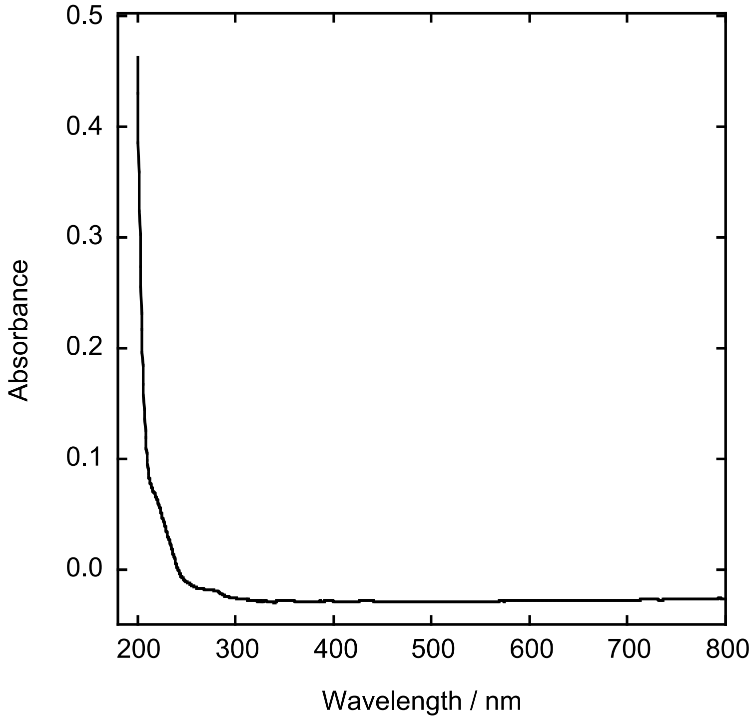

Figure 2.3: UV-vis absorption spectrum of neat BMPTFSA.

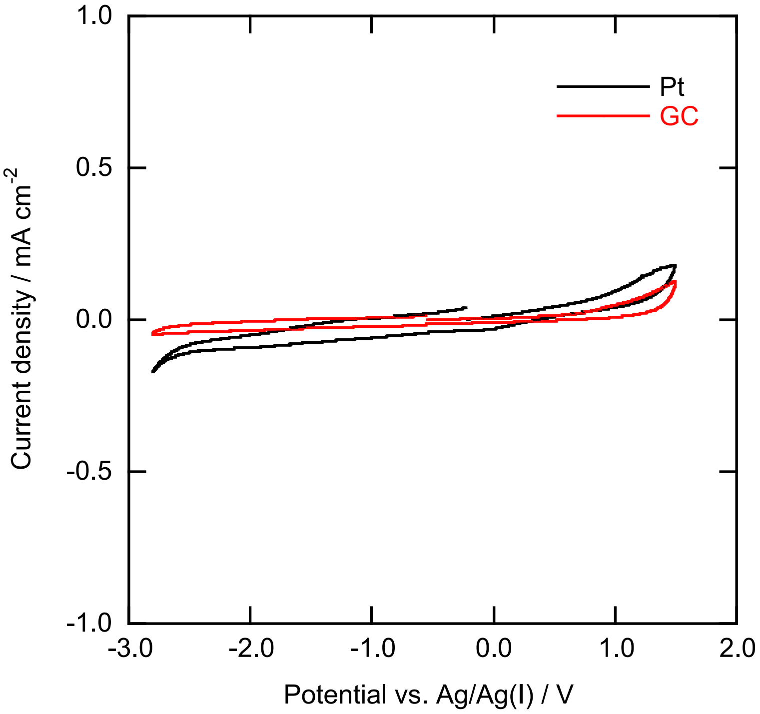

Figure 2.4: Cyclic voltammograms of a Pt (black) and GC (red) electrode in BMPTFSA at the scan rate of 50 mV s^{-1}. Temperature: 25°C.

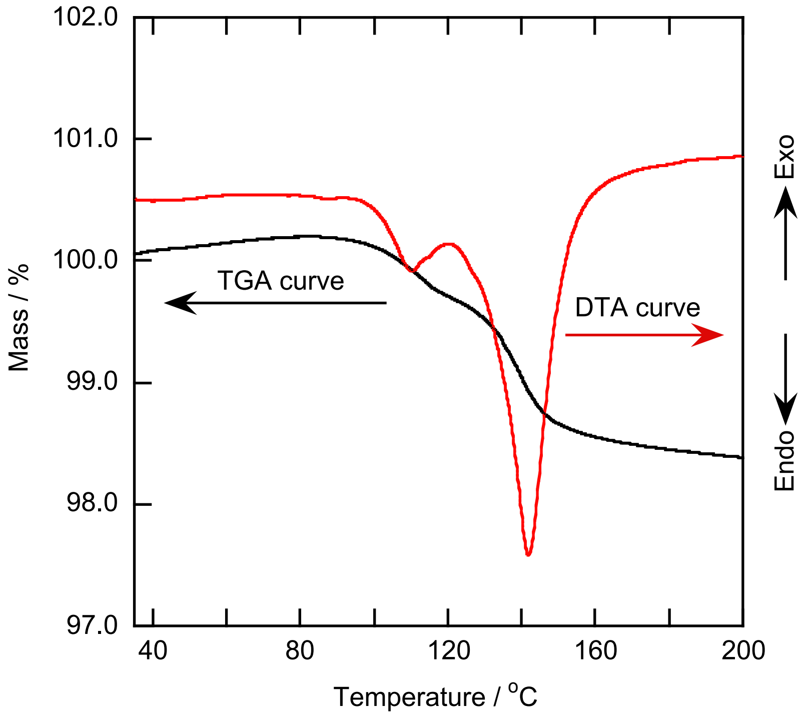

Figure 2.5: TG-DTA curves of Cd(TFSA)$_2$. Scan speed: 10°C min^{-1}.

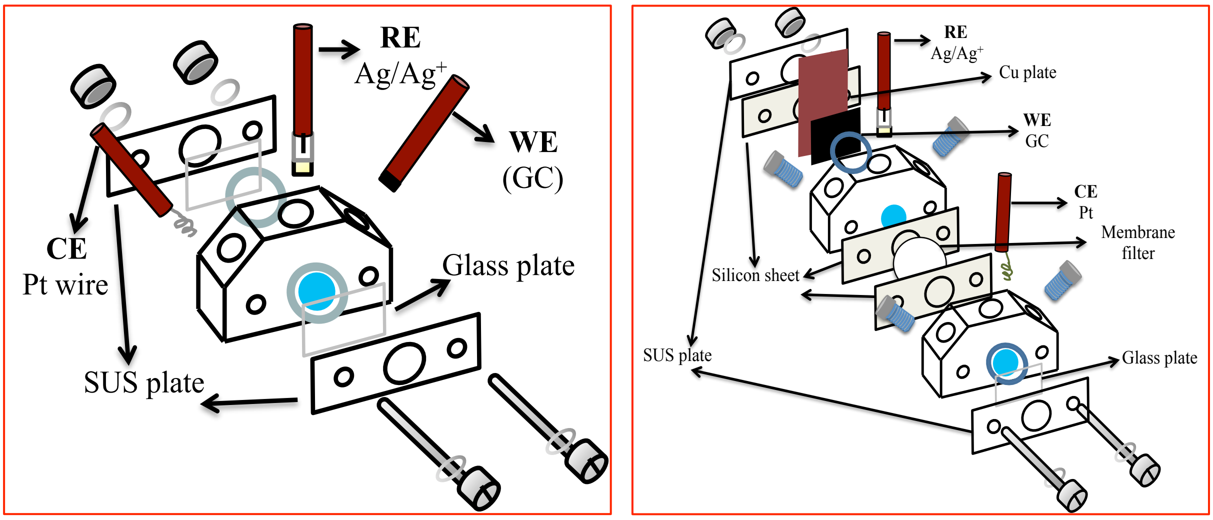

Figure 2.6: Schematic diagram of the single-compartment (left) and double-compartment (right) electrochemical cells.

Chapter 3

Electrodeposition of Cadmium in a Hydrophobic Room-temperature Ionic Liquid

3.1 Introduction

Cadmium (Cd) is a soft ductile metal with a silvery-white appearance. Cd is an important metal due to its manifold applications in rechargeable batteries, solar energy devices, nuclear reactor, electroplating industries, and so on.[1–5] Especially in plating industries, Cd is electrodeposited for a wide variety of applications particularly in the marine, automobile and aerospace field due to its high corrosion resistance and superior lubricity. Therefore, it is important to investigate the electrodeposition process of Cd in depth. Electrochemical behavior of cadmium has been studied widely in aqueous solutions. Effect of electrode materials on cadmium reduction mechanism has been analyzed by several researchers.[6–9] Other than electrode materials, effect of bath composition and additives on electrodeposition of cadmium has been investigated extensively.[10–14] However, hydrogen evolution during electrodeposition of cadmium in aqueous solutions often leads to embrittlement of the electrodeposits.

In that case, some room-temperature ionic liquids (RTILs) are expected to be the alternative aprotic media for electrodeposition, since they generally have a set of advantageous physicochemical properties as mentioned in the chapter 1. Although the electrodeposition of various metals and alloys has been attempted in RTILs, only a few studies on the electrochemical behavior of cadmium have been reported in RTILs. Wilkes et al.[3] reported the electrode process of Cd(II)/Cd in a basic 1-methyl-3-ethylimidazolium chloride–aluminum chloride. Noel and Osteryoung[15] showed that the $[CdCl_4]^{2-}$/Cd couple can be used as a buffer for a neutral 1-ethyl-3-methylimidazolium chloride–aluminum chloride. Chen and Sun[16] investigated the electrochemistry of cadmium species in a basic 1-ethyl-3-methylimidazolium chloride–tetrafluoroborate room temperature molten salt. Hung and Sun[17] reported electrochemistry and electrodeposition of cadmium and cadmium-zinc codeposit in a Lewis acidic 1-ethyl-3-methylimidazolium chloride–zinc chloride. Pan and Freyland[18] investigated the under potential deposition of Cd on a gold electrode in a Lewis acidic 1-methyl-3-butylimidazolium chloride–aluminum chloride room-temperature ionic liquid. In the previous studies, mostly, Cd electrodeposition has been investigated in chloroaluminate/zincate RTILs. In the case of these ILs, co-deposition of aluminum or zinc is unavoidable at the negative potential region. Therefore, the use of non-chloroaluminate/zincate RTILs is expected to be favorable for the electrodeposition of pure Cd. Among non-chloroaluminate/zincate RTILs, BMPTFSA has received much attention because of its several attractive properties as described earlier ("General Introduction" section). In the present study, the electrodeposition of Cd(II)/Cd was investigated in BMPTFSA. The morphology of the deposits and the nucleation process were examined at different potentials and current densities. Furthermore, formation of Cd nanoparticles was also attempted in this IL.

3.2 Experimental

3.2.1 Synthesis and Evaluation of Cd(TFSA)$_2$

3.2.1.1 Synthesis of Cd(TFSA)$_2$

Cd(TFSA)$_2$ was prepared by reacting CdO with HTFSA in deionized water at room temperature with agitation for 24 hours.

$$\mathrm{CdO + 2HTFSA \longrightarrow Cd(TFSA)_2 + H_2O} \qquad (2.4)$$

The solution was filtered in order to separate the unreacted CdO from Cd(TFSA)$_2$. A colorless transparent solution was obtained after filtration. The water in the solution was evaporated to yield a colorless solid, Cd(TFSA)$_2$. Finally, the Cd(TFSA)$_2$ was dried under vacuum at 100°C for 24 hours and stored in a glove box.

3.2.1.2 Evaluation of Cd(TFSA)$_2$

Cd(TFSA)$_2$ was a colorless powder and its purity was checked before further use. Figure 2.5 shows the TG-DTA curves of Cd(TFSA)$_2$. The TG curve showed weight loss in two steps. The first step of weight loss was found between 80 to 110°C and the second step of weight loss was found to be started from about 130°C. The DTA curve also showed two endothermic peaks at about 110 and 140°C. The first weight loss indicated the elimination of adsorbed free water in the reagent, while the second weight loss may be caused by the removal of crystal water in the sample. Therefore, the prepared $Cd(TFSA)_2$ was further dried under vacuum at 140°C in order to remove water completely. The purity of the prepared $Cd(TFSA)_2$ was estimated to be about 99% by ion chromatography.

3.2.2. Preparation of $Cd(TFSA)_2$/BMPTFSA Electrolyte

Calculated amounts of $Cd(TFSA)_2$ were dissolved into BMPTFSA to obtain $Cd(TFSA)_2$/BMPTFSA electrolyte of different concentration. A colorless electrolyte was obtained.

3.2.3 Solvation Study

Infrared (IR) spectra of BMPTFSA with and without $Cd(TFSA)_2$ were obtained using a Fourier transform IR (FT-IR) spectrometer with a attenuated total reflectance (ATR) attachment using a diamond prism.

3.2.4 Characterization of the Deposits

All the electrochemical measurements and electrodeposition experiments were conducted with a single-compartment three-electrode cell as described in chapter 2 (section 2.4). The electrodeposits washed with dehydrated acetonitrile and dried in the air were characterized by SEM, EDX and XRD. TEM was used for observation of nanoparticles in the IL. The TEM sample was prepared by putting one or two drops of the IL after electrolysis on a TEM grid and the excess IL was washed out by acetonitrile. The sample was dried before observation.

3.3 Results and Discussion

3.3.1 Solvation Structure of Cd(II) in BMPTFSA

Electrochemical behavior of a metal ion is known to be significantly influenced by its coordination environment. Therefore, the solvation structure is an important factor for the electrochemical behavior of metal ions in ILs. In RTILs, divalent Cd cation is known to form a tetra-chlorocomplex, $[CdCl_4]^{2-}$, in the presence of excess chloride ion.[3,16,19] Figure 3.1 shows the IR spectra of BMPTFSA containing $Cd(TFSA)_2$ of various concentrations. The intense bands at 740 and 790 cm^{-1} can be assigned to the S-N stretching ν(SNS) and the CF_3 bending $\delta(CF_3)$ vibration, respectively, of free

TFSA$^-$.[20] It can be seen from the spectra that the ν(SNS) and δ(CF_3) vibrations weakened with increasing the concentration of Cd(TFSA)$_2$ and new bands appeared at 747 and 796 cm^{-1}. According to the literature,[20] these new bands at 747 and 796 cm^{-1} can be ascribed due the S-N stretching ν(SNS) and the CF_3 bending δ(CF_3) vibration for the TFSA$^-$ bound to Cd(II). The peak for δ(CF_3) vibration was deconvoluted by the least square method with Voigt functions. Figure 3.2 shows the deconvuleted IR spectra of the peak corresponding to the CF_3 bending δ(CF_3) vibration of TFSA$^-$ in BMPTFSA containing Cd(TFSA)$_2$ of different concentrations. In the deconvoluted IR spectra, the experimental data is shown as black dots while the red line represents the sum of all deconvoluted areas. The blue and green lines represent the deconvoluted bands of CF_3 bending δ(CF_3) vibration for the free TFSA$^-$ and the TFSA$^-$ bound to Cd(II), respectively. The number of TFSA$^-$ bound to Cd(II), n, is able to be evaluated from the following equation;[20]

$$I_\mathrm{f} / c_\mathrm{M} = \varepsilon_\mathrm{f} l (c_\mathrm{T} / c_\mathrm{M} - n) \tag{3.1}$$

where c_M is the concentration of Cd^{2+} and c_T is the concentration of total TFSA$^-$. Figure 3.3 shows the plot of $I_\mathrm{f}/c_\mathrm{M}$ against $c_\mathrm{T}/c_\mathrm{M}$ for the intensity of δ(CF_3) vibration. The n value calculated from the intercept of the regression line was found to be 3.0, implying three TFSA$^-$ solvate Cd(II) in the IL. On the other hand, it has already been reported that Ni(II) and Co(II) are octahedrally coordinated by six oxygen atoms of three TFSA$^-$ in BMPTFSA.[21,22] Cd(II) was also reported to form an octahedral complex in water.[23] Therefore, the divalent Cd(II) cation was considered to be octahedrally coordinated probably by six oxygen atoms of three TFSA$^-$ to form an anionic complex like [Cd(TFSA)$_3$]$^-$. Figure 3.4 shows the schematic illustration of the structure of [Cd(TFSA)$_3$]$^-$.

3.3.2 Cyclic Voltammetry

Figure 3.5 shows the cyclic voltammograms of a GC electrode in 0.05 M Cd(TFSA)$_2$/BMPTFSA with various scan rates at 30°C using IR compensation. In the cyclic voltammograms, a cathodic and anodic current peak were observed at about –1.3 and –0.5 V, respectively. The cathodic and anodic peaks were found only in the presence of of Cd(II). Moreover, the deposit obtained by the potentiostatic cathodic reduction at −1.4 V was confirmed as metallic Cd by XRD and EDX as shown in Figure

3.6. Thus, the cathodic peak was ascribed to the reduction of Cd(II) to Cd(0) while the anodic current peak was assignable to the anodic dissolution of the deposited Cd.

The formal potential of Cd(II)/Cd in BMPTFSA was determined by measuring the open circuit potential of a Cd electrode immersed in BMPTFSA containing Cd(II) at various concentrations. Figure 3.7 shows the open circuit potentials of a Cd electrode immersed in BMPTFSA containing $Cd(TFSA)_2$ at various concentrations at 25°C. A linear relationship was found between the open circuit potentials and the logarithms of Cd(II) concentration, as represented by the following equation.

$$E = E^{0'} + \frac{RT}{nF} \ln C_{\mathrm{Cd(II)}} \qquad (3.2)$$

The linear relationship between the open circuit potentials and the logarithms of Cd(II) concentration indicated that the electrode potential was determined by the redox equilibrium between Cd(II) and Cd. The formal potential of Cd(II)/Cd was found to be –0.71 V from the intercept. The formal potential of Cd(II)/Cd vs. Fc/Fc^+ in different conventional solvents was calculated from the literature[24,25] as listed in Table 3.1 along with that found in BMPTFSA. Figure 3.8 shows the plots of formal potentials of Cd(II)/Cd vs. Fc/Fc^+ in different conventional solvents including BMPTFSA against their donor numbers. The donor number of BMPTFSA has already been reported in literature.[26] It can be seen from Figure 3.8 (also from Table 3.1) that the formal potential of Cd(II)/Cd in BMPTFSA was more positive than those in other conventional solvents, verifying the weak coordination ability of $TFSA^-$.

Table 3.1: Formal potential of Cd(II)/Cd vs. Fc/Fc$^+$ in BMPTFSA and in different conventional solvents.

Solvent	**Formal potential vs. Fc/Fc$^+$ / V**
BMPTFSA	–0.28
Propylene carbonate (PC)	–0.48
Acetonitrile (AN)	–0.55
Benzonitrile (BN)	–0.59
Acetone (AC)	–0.62
Tetramethylene sulfone (TMS)	–0.67
N,N-Diethylformamide (DEF)	–0.88
Formamide (FA)	–0.92
Trimethyl phosphate (TMP)	–0.98
N-Methylformamide (NMF)	–1.01
N,N-Diethylacetamide (DEA)	–1.02
Hexamethylphosphoric triamide (HMP)	–1.07
Dimethyl sulfoxide (DMSO)	–1.11

The slope of the line shown in Figure 3.7 was found to be 28 mV decade^{-1}. The theoretical values for a two-electron transfer reaction at 25°C is 30 mV decade^{-1}. Therefore, the electroreduction of Cd(II) can be represented as a two electron transfer process as shown below.

$$\mathrm{Cd(II)} + 2e^- \rightleftharpoons \mathrm{Cd} \qquad (3.3)$$

In the cyclic voltammograms shown in Figure 3.5, the integrated electric charges of the anodic peaks were smaller than those of the cathodic ones, suggesting the electrodeposited Cd during the cathodic scan was not stripped completely during the anodic scan. Such incomplete stripping was also known for the cyclic voltammetry of some other metal species[27,28,22] in BMPTFSA. If the concentration of Cd(II) during anodic scan near the electrode surface increased up to its saturated concentration quickly then the anodic dissolution could be suppressed. As a result, complete stripping of the deposited Cd was impossible during anodic scan. On the other hand, the large separation between the cathodic and anodic peak current and the shifting of cathodic peak potential towards negative direction with an increase in the scan rates indicated the reduction of Cd(II) at a GC electrode was electrochemically irreversible. Figure 3.9 shows the dependence of the cathodic peak potential, E_{p}, on the logarithm of scan rate for the reduction of Cd(II) on a GC electrode. For an irreversible electrode reaction, the peak potential is known to be related with the scan rate, v, by the following equation.[29]

$$E_{\mathrm{p}} = E^{0'} - \frac{RT}{\alpha n_{\mathrm{a}} F}\left[0.780 + \ln\left(\frac{D^{1/2}}{k^{0}}\right) + \ln\left(\frac{\alpha n_{\mathrm{a}} F v}{RT}\right)^{1/2}\right] \qquad (3.4)$$

E_{p} was found to be shifted negatively more than 100 mV per 10-fold increase in the scan rate, indicating the electrode process for the reduction of Cd(II) is electrochemically irreversible.[29] The product of the transfer coefficient, α, and the number of electrons in the rate-determining process, n_{a}, was estimated to be 0.21 from the slope. This αn_{a} value may imply the rate-determining step of reduction of Cd(II) to Cd(0) is one-electron transfer process since the value of α is generally in the range from 0.3 to 0.7. However, the nucleation process on a GC electrode may affect the rate of charge transfer process in the present study.

3.3.3 Chronoamperommetry

In order to study the mechanism of cadmium nucleation and/or growth process, chronoamperometric experiments were performed. These experiments were carried out by stepping the potential of the working electrode from a value where no reduction of Cd(II) would occur to the potentials sufficiently negative to initiate nucleation/growth process after a short induction time, t_{o}. Figure 3.10 shows the chronoamperograms (j-t) of a GC electrode in 0.05 M Cd(TFSA)$_2$/BMPTFSA at different step potentials. The chronoamperograms exhibit the typical shape for nucleation and growth process.[30,31] A current peak characteristic of nucleation and growth process was observed just after the charging current for each potential steps. After the peaks, the current densities converged with the elapse of time, indicating the reduction of Cd(II) satisfied the Cottrell's criteria and can be regarded as the diffusion-limited process. The diffusion coefficient of Cd(II) was calculated from the chronoamperometric data using the Cottrell's equation, as follows.

$$j(t) = \frac{nFD^{1/2}C}{\pi^{1/2}t^{1/2}} \qquad (3.5)$$

Figure 3.11 shows the Cottrell plot for the chronoamperogram of a GC electrode in 0.05 M Cd(TFSA)$_2$/BMPTFSA at –1.9 V. From the slope of the Cottrell plot, the diffusion coefficient of Cd(II) at 25°C was estimated to be 9×10^{-8} $\mathrm{cm^2\,s^{-1}}$, which is close to those for some other divalent metal species in BMPTFSA, as listed in Table 3.2.

Table 3.2: Diffusion coefficients (*D*) of some divalent species in BMPTFSA at 25°C.

Species	**C / mol L^{-1}**	**10^8 *D* / cm^2 s^{-1}**	**Ref.**
Cd(II)	0.05	9	This work
Pb(II)	0.05	8	32
Co(II)	0.1	10	28
Ni(II)	0.1	9	22

The solvation structure of Co(II) and Ni(II) in BMPTFSA has already been reported as $[\mathrm{Co(TFSA)_3}]^-$ and $[\mathrm{Ni(TFSA)_3}]^-$, respectively.[22,21] Since the diffusion coefficient of Cd(II) is close to those of Co(II) and Ni(II), the coordination environment of Cd(II) is expected to be similar to those of Co(II) and Ni(II). Thus, the diffusion coefficient value of Cd(II) also supports the IR result as described above.

The observed peaks in the chronoamperograms were further analyzed to examine the initial stage of nucleation and crystal growth for the electrodeposition of Cd on a GC electrode according to three-dimensional nucleation and crystal growth model under diffusion control by Scharifker and Hills.[31] It was considered that a set of hemispherical nuclei randomly deposits on the electrode surface and grows under 3D diffusion control, as shown in Figure 3.12. However, the radii of diffusion zones grow and overlap with time and then the depositing species can reach to the electrode surface only through one-dimensional perpendicular diffusion.

Two limiting case for the initial stage of 3D nucleation and crystal growth on an electrode surface, instantaneous and progressive nucleation, were specified by the following dimensionless equations;

$$\left(j / j_\mathrm{m}\right)^2 = \frac{1.9542}{\left(t / t_\mathrm{m}\right)}\left[1 - \exp\left\{-1.2564\left(t / t_\mathrm{m}\right)\right\}\right]^2 \quad \text{(instantaneous nucleation)} \quad (3.6)$$

$$\left(j / j_\mathrm{m}\right)^2 = \frac{1.2254}{\left(t / t_\mathrm{m}\right)}\left[1 - \exp\left\{-2.3367\left(t / t_\mathrm{m}\right)^2\right\}\right]^2 \quad \text{(progressive nucleation)} \quad (3.7)$$

where j_m is the peak current density and t_m is the time at j_m. Figure 3.13 shows the dimensionless plots of $(j/j_\mathrm{m})^2$ and t/t_m for a series of step potentials with the theoretical curves according to eqs. (3.6) and (3.7). The experimental plots for the step potentials more positive than –1.8 V were distributed closely to the theoretical curve for progressive nucleation, indicating the nucleation is preferable to crystal growth. On the other hand, the experimental plot for the step potential of –1.9 V laid between the progressive and instantaneous nucleation curves, suggesting the crystal growth is preferred to nucleation at the more negative potentials. Although the current density is considered to reach the limiting current density at the potentials more negative than –1.5 V, as described above, the nucleation process was found to change depending on the applied potential. The dependence of nucleation process on the applied potential is considered due to the difference in accumulation of cations on the negatively polarized electrode surface. The influence of accumulation of cations against the electrode reactions in BMPTFSA has been already reported for electrodeposition of Ag and Pb.[33,32] The dependence of the structure of electric double layer in ionic liquids on the potential has been investigated by atomic force microscopy[34] and various spectroscopic methods.[35,36]

3.3.4 Electrodeposition of Cd

3.3.4.1 Influence of Current Density

Galvanostatic electrodeposition of Cd on a GC substrate in 0.05 M $\mathrm{Cd(TFSA)_2}$/BMPTFSA was carried out with the current densities of –30 and –80 μA cm^{-2} at 30°C. A grayish black deposit obtained at –30 μA cm^{-2} was confirmed to be metallic Cd by XRD and EDX analysis, as shown in Figure 3.14. The oxygen peak observed in the EDX spectrum may be due to the formation of cadmium oxide on the surface of the electrodeposit during washing and exposure to the air before the EDX analysis.

Figure 3.15 shows the SEM images of the electrodeposited Cd. Spongy-like deposit was obtained at the lower (–30 μA cm^{-2}) current density (Figure 3.15 (a) and (c)) whereas flower-like deposit was found at the higher (–80 μA cm^{-2}) current density (Fig. 3.15 (b) and (d)). The crystallite size was calculated for (101) plane using Scherrer equation as follows;

$$\chi_\mathrm{s} = \frac{0.9\lambda}{\mathrm{FWHM}\cos\theta} \tag{3.8}$$

where FWHM is the full width at half maximum. The crystallite size of the deposit obtained at the low current density (26.9 nm) was found to be smaller than that for the deposit obtained at the high current density (46.6 nm), indicating the difficulty of coarse grain formation at the low current density, as seen in the SEM image. Since the overpotential was small at the lower current density, the accumulation of BMP^+ on the surface was not so significant and nucleation became faster than crystal growth. On the other hand, crystal growth was more facile than nucleation under the larger overpotential at the higher current density, resulting in formation of flower-type structure. The steady-state potential during the galvanostatic electrodeposition was also found to be more negative at the high current density ($-80\ \mu A\ cm^{-2}$) than that at the low current density ($-30\ \mu A\ cm^{-2}$). Thus, the morphology of the electrodeposits is considered affected by the change in the double layer structure with the steady-state potential, as described below.

3.3.4.2 Influence of Potential

Figure 3.16 shows the SEM images of the electrodeposited Cd in 0.05 M $Cd(TFSA)_2$/BMPTFSA at different potentials. The morphology of the deposits was found to change with the applied potentials. A dramatic change in morphology was found for the deposit obtained at the more negative potential (–2.6 V). Secondary spherical particles consisted of primary nanoparticles were found at this potential, as shown in Figures 3.16(d) and 3.16(e). Since the analysis of initial stage of nucleation and crystal growth showed (Figure 3.13) a change of nucleation process with the applied potential, a correlation between the morphological variation of the deposits with the applied potential and the change of nucleation process with the reduction potential is moderately acceptable. Therefore, a change in the electric double layer structure due to the difference in the population of cations and anions of IL with the applied potential seems to play the key role on the morphological variation. The excess negative charge of the negatively polarized electrode has to be compensated by the cationic species in the IL. As BMP^+ is only the cationic species in the IL, the charge compensation at the electrode surface is expected to be achieved by an increase in the molar ratio of BMP^+ near the electrode surface. Therefore, with changing the potential to the more negative side, the electrode surface is expected to be covered by more BMP^+ cation, which in turn may hinder some surface processes, such as nucleation, crystal growth and surface diffusion of Cd adatoms, resulting in the change of the morphology and even formation of nanoparticles.

Figure 3.17 shows the current density observed during the potentiostatic cathodic reduction on a glassy carbon electrode in BMPTFSA containing 0.05 M $Cd(TFSA)_2$ at different electrolysis potentials. The steady-state current densities at –1.4, –1.6 and –1.8 V showed similar trends, indicating the reduction rate of Cd(II) was determined by diffusion of Cd(II) to give the limiting current density. However, at –2.6 V an increase in the current density with time was observed probably due to the increased surface area as a result of nanoparticle formation.

In our research group, dispersion of nanoparticles in the bulk IL have already been reported for some metals during potentiostatic electrolysis at relatively more negative potentials.[33,37,38] Accordingly, 0.05 M $Cd(TFSA)_2$/BMPTFSA after potentiostatic electrolysis at –2.6 V was analyzed using TEM. Figure 3.18 shows the TEM images of the nanoparticles formed in the IL. The sizes of nanoparticles were in the range from 5 to 10 nm, which are slightly larger than those for Pt[39] and Au[40] nanoparticles prepared in the same IL. In addition, there were the large particles, which are considered the aggregates of the nanoparticles. Since the growth of nuclei is hindered by the accumulation of the organic cations at much negative potentials, some nuclei are expected to be detached from the surface of electrode and stabilized in the ionic liquid.[33]

3.4 Conclusions

The divalent Cd(II) in BMPTFSA was found to be coordinated by three $TFSA^-$ and probably exists as $[Cd(TFSA)_3]^-$. The electrodeposition of metallic Cd was possible in an amide-type RTIL, BMPTFSA. Electrochemical reaction of Cd(II)/Cd on a GC electrode was an electrochemically irreversible process probably involving 2 one-electron transfer steps. Diffusion coefficient of Cd(II) was estimated to be 9×10^{-8} cm^2 s^{-1} at 25°C. The nucleation process and morphology of the electrodeposits were found to be affected by the applied potential under diffusion-controlled region, suggesting the influence of the potential on the electric double layer structure due to the difference in accumulation of cations leads to the change in surface processes and morphology. Formation of Cd nanoparticles was confirmed during the potentiostatic cathodic reduction at the more negative potential region. Moreover, Cd nanoparticles obtained at the more negative potential region were dispersed and stabilized in the IL. Therefore, BMPTFSA can be a promising electrolyte for electrodeposition of metals with tunable morphology. Furthermore, this IL can be a medium for electrochemical preparation of various metals nanoparticles without any additional stabilizer.

3.5 References

1. R. H. Bube and K. W. Mitchell, *J. Electron. Mater.*, **22**, 17–25 (1993).
2. G. Hodes, I. D. J. Howell, and L. M. Peter, *J. Electrochem. Soc.*, **139**, 3136–3140 (1992).
3. C. J. Dymek, G. F. Reynolds, and J. S. Wilkes, *J. Electrochem. Soc.*, **134**, 1658–1663 (1987).
4. M. Mirzaii, S. Seyyedi, M. Sadeghi, and Z. Gholamzadeh, *J. Radioanal. Nucl. Chem.*, **284**, 333–339 (2010).
5. M. J. Scoullos, Ed., *Mercury, Cadmium, Lead: Handbook for Sustainable Heavy Metals Policy and Regulation*, Kluwer Academic Publishers, Netherlands, (2001).
6. J. A. Harrison and D. R. Sandbach, *J. Electroanal. Chem. Interfacial Electrochem.*, **85**, 125–133 (1977).
7. G. Gunawardena, G. Hills, and I. Montenegro, Intergovernmental Panel on Climate Change, Editor. *J. Electroanal. Chem. Interfacial Electrochem.*, **184**, 371–389 (1985).
8. F. J. C. Bijl, M. S. Rehbach, and J. H. Sluyters, *J. Electroanal. Chem.*, **435**, 137–147 (1997).
9. R. Vidu and S. Hara, *Surf. Sci.*, **452**, 229–238 (2000).
10. A. M. A. El-Halim and M. I. Sobahi, *Surf. Technol.*, **19**, 45–57 (1983).
11. T. C. Franklin, *J. Electrochem. Soc.*, **143**, 2759–2764 (1996).
12. T. S. N. S. Narayanan, *Met. Finish.*, **97**, 94–99 (1999).
13. T. Montiel, O. Solorza, and H. Sanchez, *J. Electrochem. Soc.*, **147**, 1031–1037 (2000).
14. A. Dolati, A. Afshar, and H. Ghasemi, *Mater. Chem. Phys.*, **94**, 23–28 (2005).
15. M. A. M. Noel and R. A. Osteryoung, *J. Electroanal. Chem. Interfacial Electrochem.*, **293**, 139–150 (1990).
16. P. Y. Chen and I. W. Sun, *Electrochim. Acta*, **45**, 3163–3170 (2000).
17. J. F. Huang and I. W. Sun, *J. Electrochem. Soc.*, **149**, E348–E355 (2002).
18. G. B. Pan and W. Freyland, *Phys. Chem. Chem. Phys.*, **9**, 3286–3290 (2007).
19. M. A. M. Noel and R. A. Osteryoung, *J. Electroanal. Chem. Interfacial Electrochem.*, **284**, 413–429 (1990).
20. K. Fujii, T. Nonaka, Y. Akimoto, Y. Umebayashi, and S. Ishiguro, *Anal. Sci.*, **24**, 1377–1380 (2008).
21. Y. Katayama, R. Fukui, and T. Miura, *J. Electrochem. Soc.*, **154**, D534–D537

(2007).

22. Y. L. Zhu, Y. Kozuma, Y. Katayama, and T. Miura, *Electrochim. Acta*, **54**, 7502–7506 (2009).
23. H. Ohtaki and G. Johansson, *Pure & Appl. Chem.*,**53**, 1357–1364 (1981).
24. G. Gritzner, *J. Phys. Chem.*, **90**, 5478–5485 (1986).
25. T. Mussini, P. Longhi, and S. Rondinini, *Pure Appl. Chem.*, **57**, 169–179 (1985).
26. M. Yamagata, Y. Katayama, and T. Miura, *J. Electrochem. Soc.*, **153**, E5–E9 (2006).
27. M. J. Deng, P. Y. Chen, and I. W. Sun, *Electrochim. Acta*, **53**, 1931–1938 (2007).
28. R. Fukui, Y. Katayama, and T. Miura, *Electrochemistry*, **73**, 567–569 (2005).
29. A. J. Bard and L. R. Faulkner, *Electrochemical Methods, Fundamentals and Applications*, 2nd ed., John Wiley & Sons, Inc., New York, (2001).
30. B. R. Scharifker and J. Mostany, *J. Electroanal. Chem. Interfacial Electrochem.*, **177**, 13–23 (1984).
31. B. Scharifker and G. Hills, *Electrochim. Acta*, **28**, 879–889 (1983).
32. Y. Katayama, R. Fukui, and T. Miura, *J. Electrochem. Soc.*, **160**, D251–D255 (2013).
33. R. Fukui, Y. Katayama, and T. Miura, *J. Electrochem. Soc.*, **158**, D567–D572 (2011).
34. R. Hayes, N. Borisenko, M. K. Tam, P. C. Howlett, F. Endres, and R. Atkin, *J. Phys. Chem. C*, **115**, 6855–6863 (2011).
35. S. Baldelli, *Acc. Chem. Res.*, **41**, 421–431 (2008).
36. W. Zhou, S. Inoue, T. Iwahashi, K. Kanai, K. Seki, T. Miyamae, D. Kim, Y. Katayama, Y. Ouchi, *Electrochem. commun.*, **12**, 672–675 (2010).
37. Y. L. Zhu, Y. Katayama, and T. Miura, *Electrochem. Solid-State Lett.*, **14**, D110–D115 (2011).
38. Y. Katayama, R. Fukui, and T. Miura, *Electrochemistry*, **81**, 532–534 (2013).
39. Y. Katayama, T. Endo, T. Miura, and K. Toshima, *J. Electrochem. Soc.*, **160**, D423–D427 (2013).
40. Y. Katayama, T. Endo, T. Miura, and K. Toshima, *J. Electrochem. Soc.*, **161**, D87–D91 (2014).

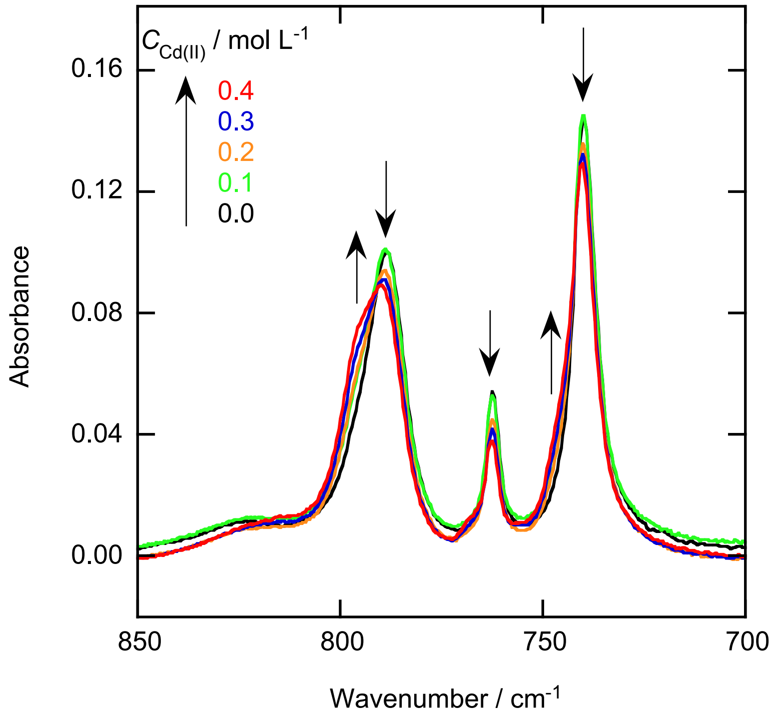

Figure 3.1: IR spectra of BMPTFSA containing Cd(TFSA)$_2$ of various concentrations.

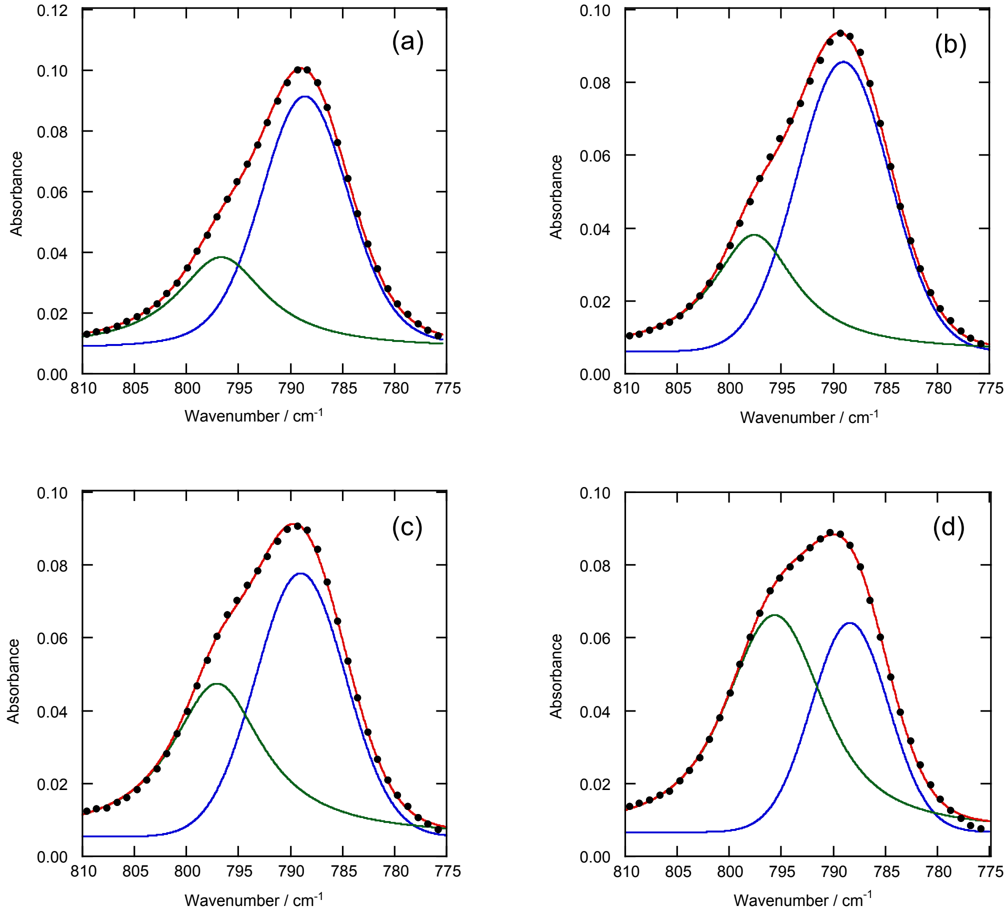

Figure 3.2: Deconvoluted IR spectra of the peak corresponding to the CF_3 bending $\delta(CF_3)$ vibration of $TFSA^-$ in BMPTFSA containing (a) 0.1, (b) 0.2, (c) 0.3, and (d) 0.4 M $Cd(TFSA)_2$.

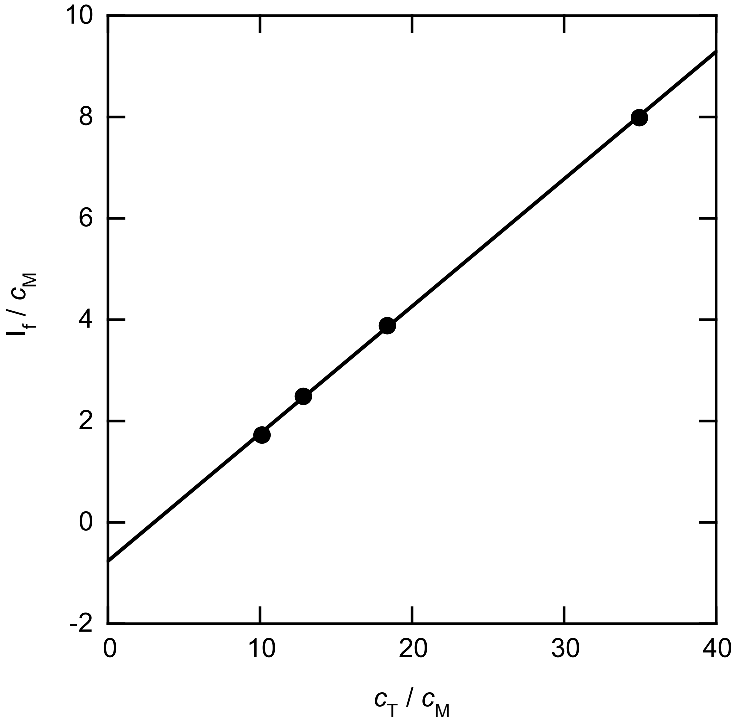

Figure 3.3: The I_f / c_M vs. c_T / c_M plots.

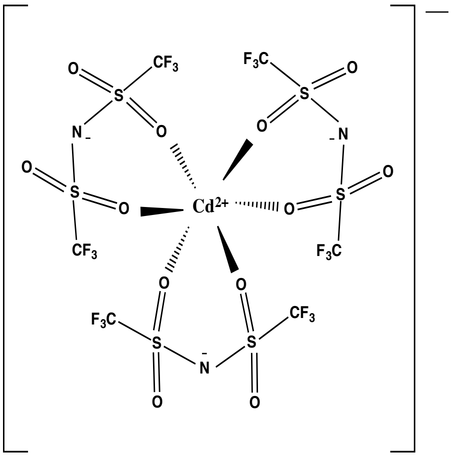

Figure 3.4: Structure of $[Cd(TFSA)_3]^-$.

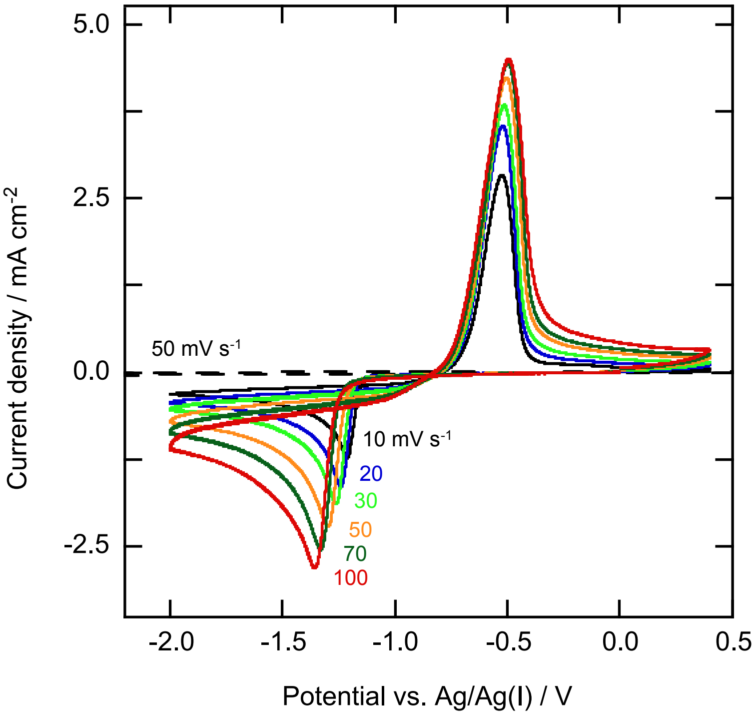

Figure 3.5: Cyclic voltammograms of a GC electrode in 0.05 M $Cd(TFSA)_2$/BMPTFSA with various scan rates at 30°C. The dashed line shows the cyclic voltammogram in neat BMPTFSA.

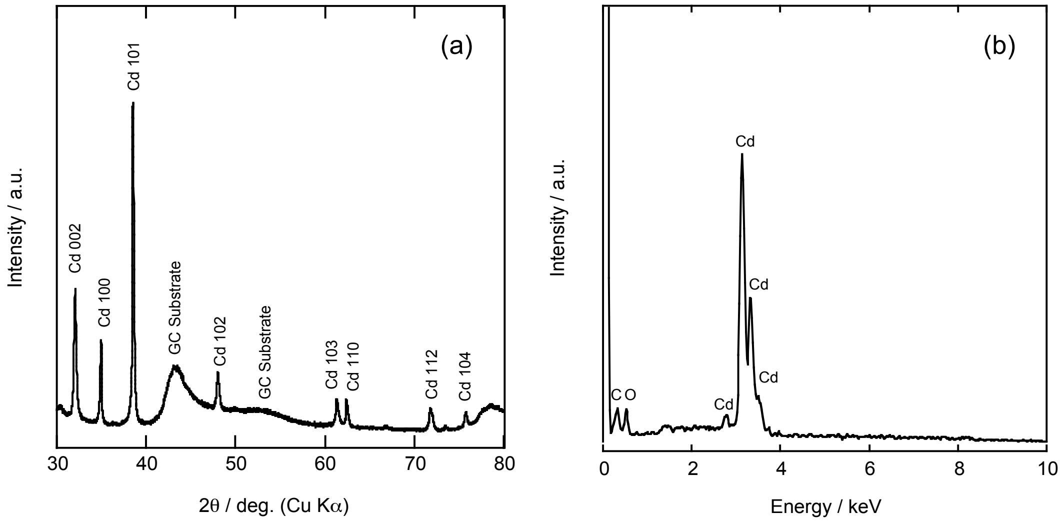

Figure 3.6: (a) XRD pattern and (b) EDX spectrum of the electrodeposit obtained by potentiostatic electrolysis on a GC electrode in 0.05 M $Cd(TFSA)_2$/BMPTFSA at –1.4 V (Temperature: 30°C, Electric charge: 3 C).

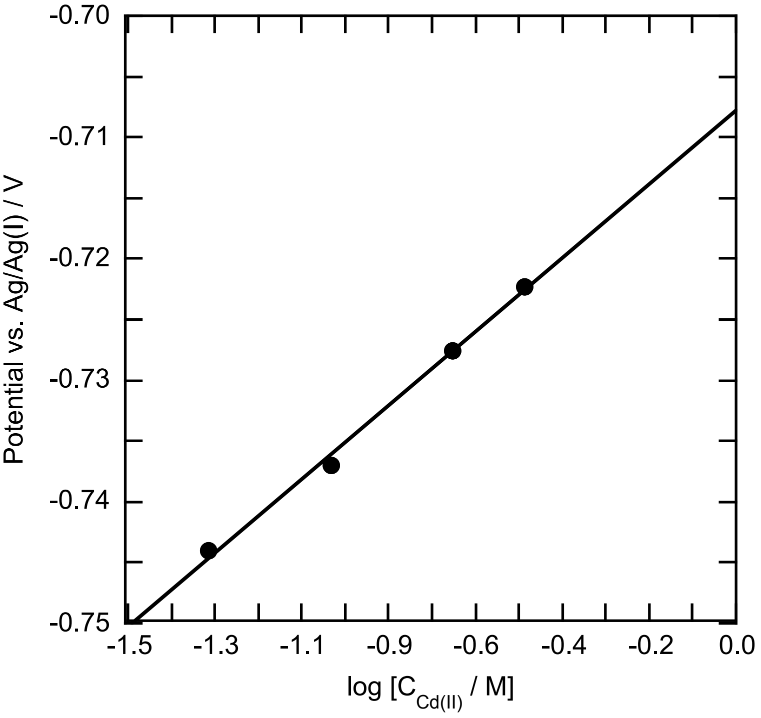

Figure 3.7: Open circuit potentials of a Cd electrode immersed in BMPTFSA containing $Cd(TFSA)_2$ at various concentrations at 25°C.

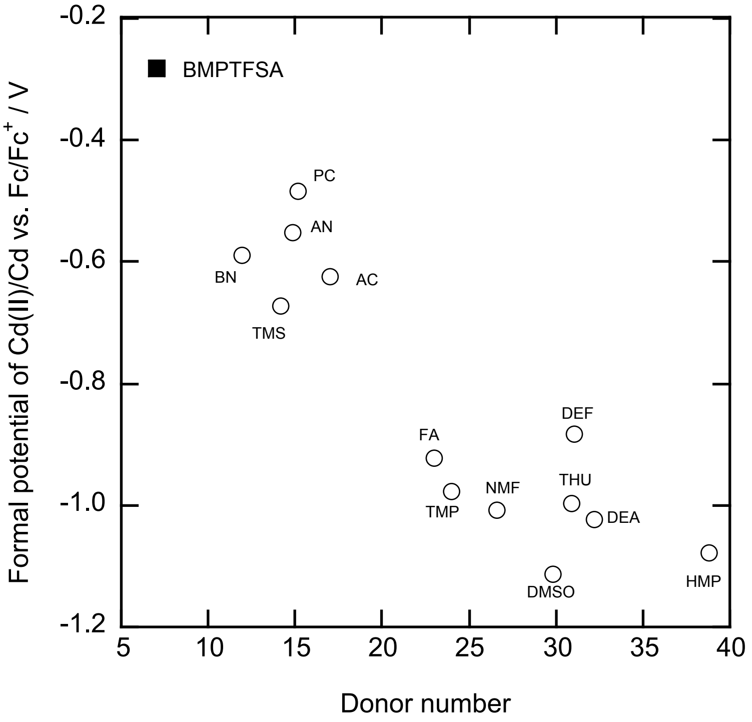

Figure 3.8: Formal potential of Cd(II)/Cd vs. Fc/Fc^+ in different conventional solvents including BMPTFSA as a function of their donor numbers.

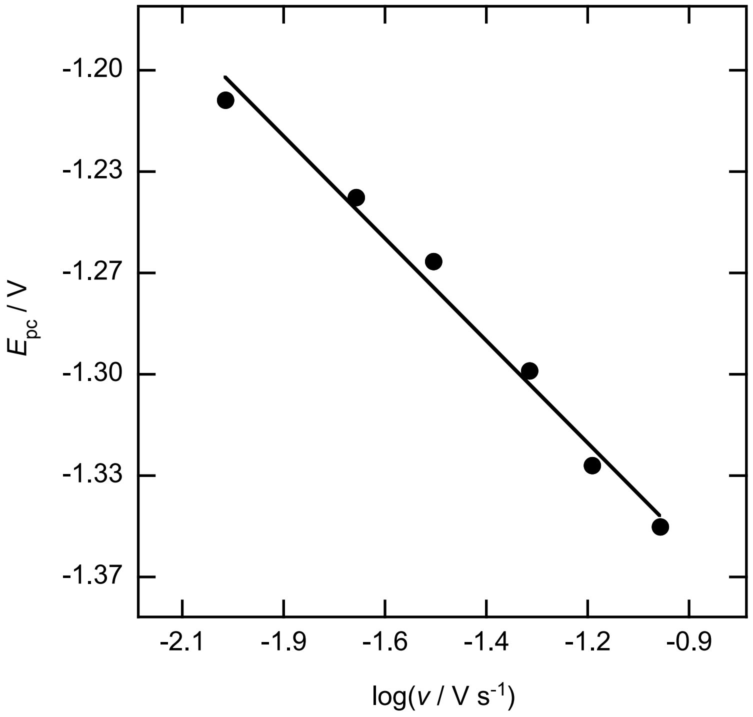

Figure 3.9: Variation of cathodic peak potentials with the logarithms of scan rates for the cyclic voltammograms of a GC electrode in 0.05 M Cd(TFSA)$_2$/BMPTFSA at 30°C.

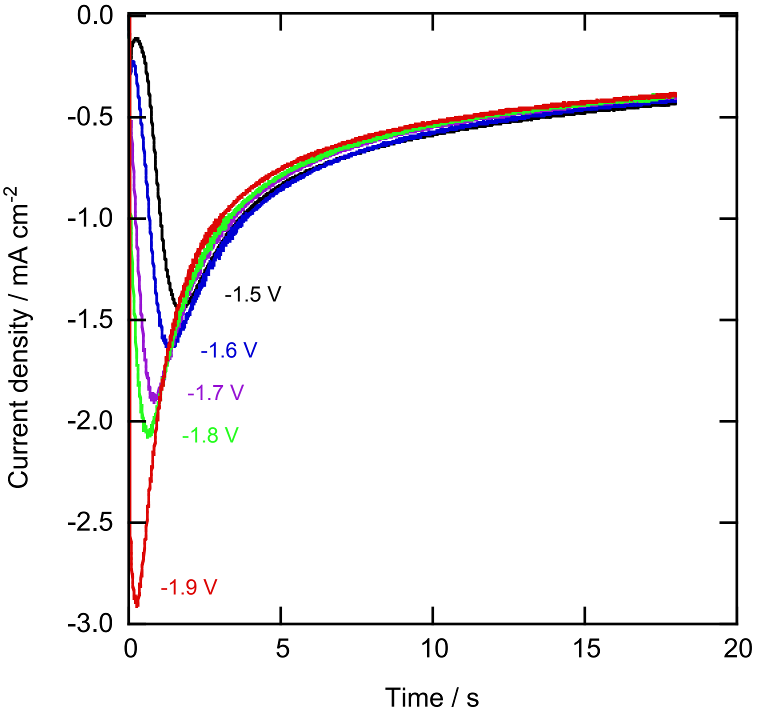

Figure 3.10: Chronoamperograms of a GC electrode in 0.05 M Cd(TFSA)$_2$/BMPTFSA at a series of step potentials at 25°C.

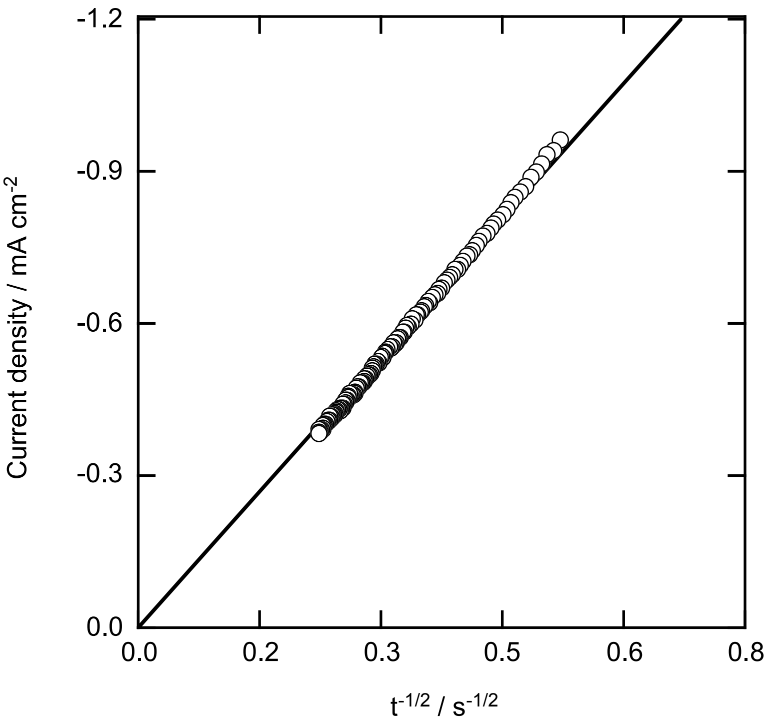

Figure 3.11: Cottrell plot for the chronoamperogram of a GC electrode in 0.05 M Cd(TFSA)$_2$/BMPTFSA at –1.9 V.

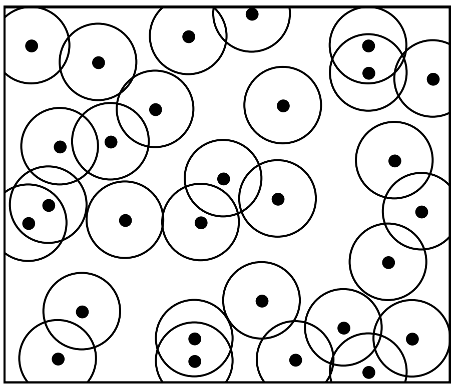

Figure 3.12: Plane view of hemispherical nuclei (•) randomly distributed on the electrode surface. The surrounding circles represent their diffusion zones.

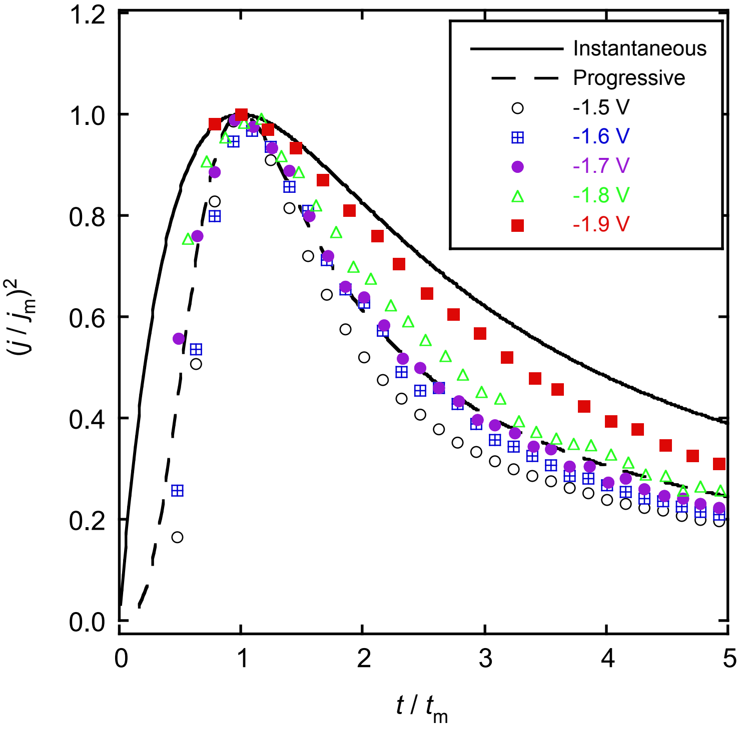

Figure 3.13: Dimensionless plots of $(j/j_m)^2$ vs. t/t_m based on the chronoamperograms.

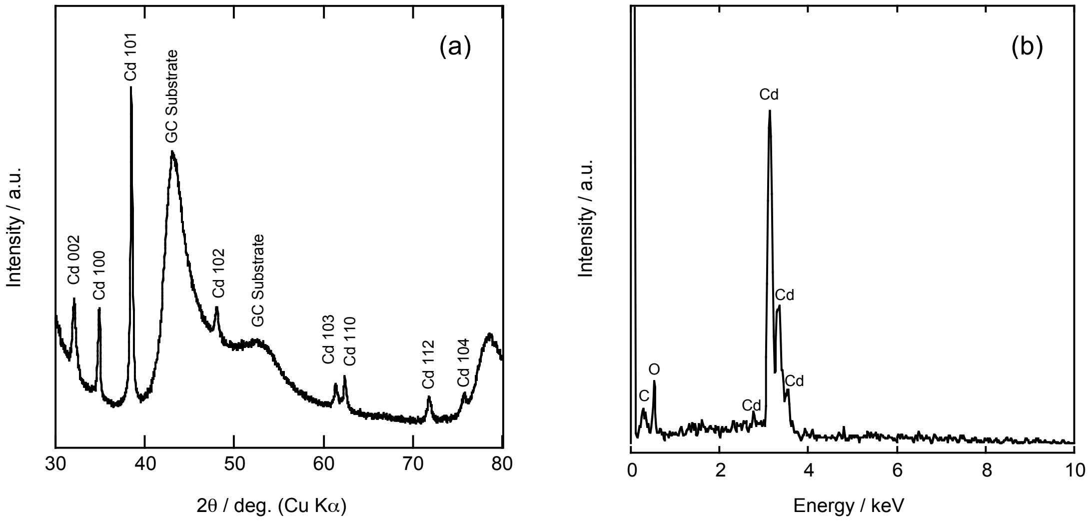

Figure 3.14: (a) XRD pattern and (b) EDX spectrum of the electrodeposit obtained by galvanostatic cathodic reduction on a GC electrode in 0.05 M $Cd(TFSA)_2$/BMPTFSA at $-30\ \mu A\ cm^{-2}$ (Temperature: 30°C, Electric charge: 3 C).

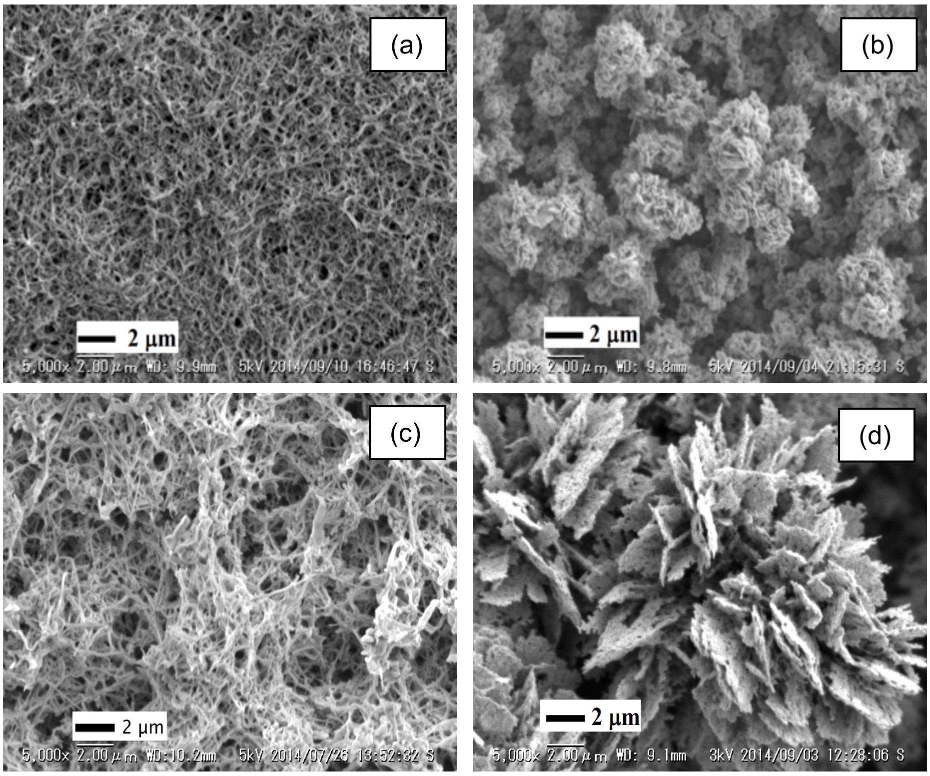

Figure 3.15: SEM images of the electrodeposits obtained by galvanostatic cathodic reduction on a GC electrode in 0.05 M Cd(TFSA)$_2$/BMPTFSA at –30 μA cm^{-2} ((a) 3C and (c) 5.8 C) and –80 μA cm^{-2} ((b) 3C and (d) 5.8 C); (Temperature: 30°C).

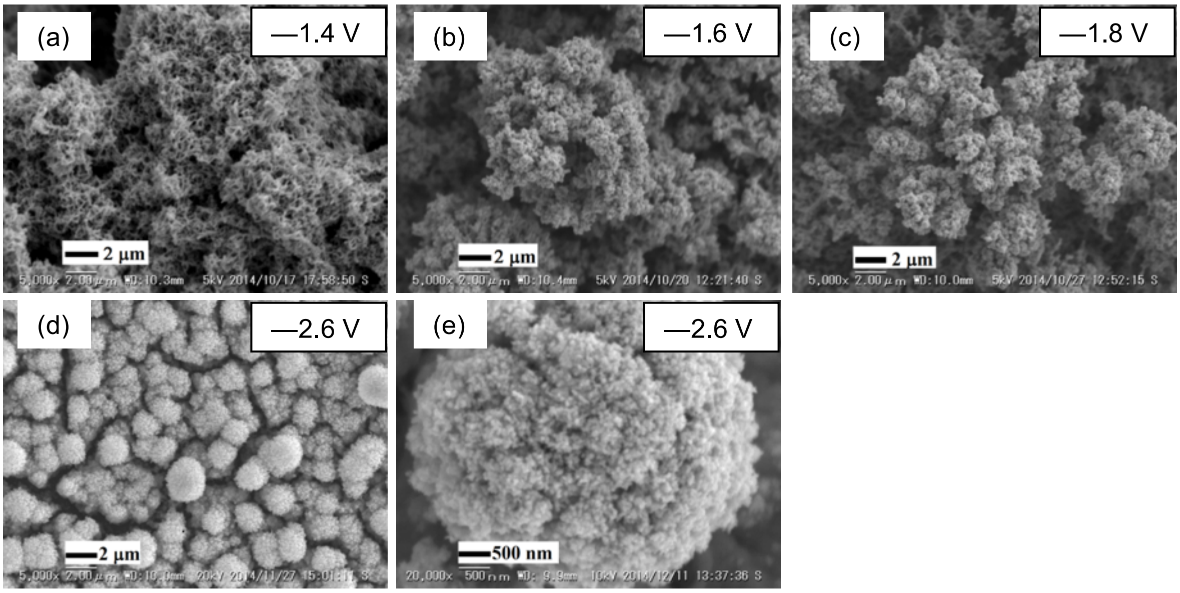

Figure 3.16: SEM images of the electrodeposits obtained by potentiostatic electrolysis on a GC electrode in 0.05 M Cd(TFSA)$_2$/BMPTFSA at different potentials (Temperature: 30°C, Electric charge: 3 C).

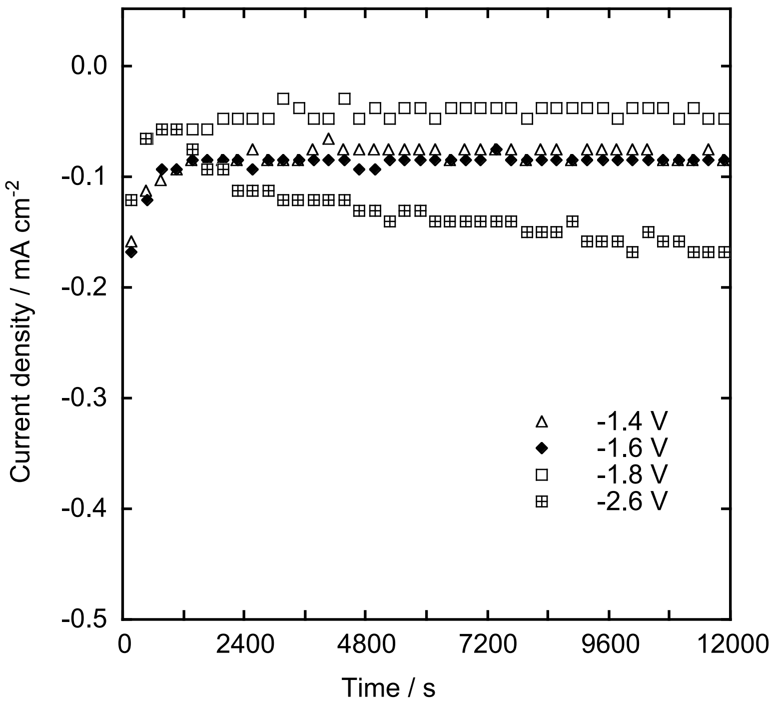

Figure 3.17: The current density during the potentiostatic cathodic reduction on a GC electrode in 0.05 M Cd(TFSA)$_2$/BMPTFSA at different electrolysis potentials. (Temperature: 30°C)

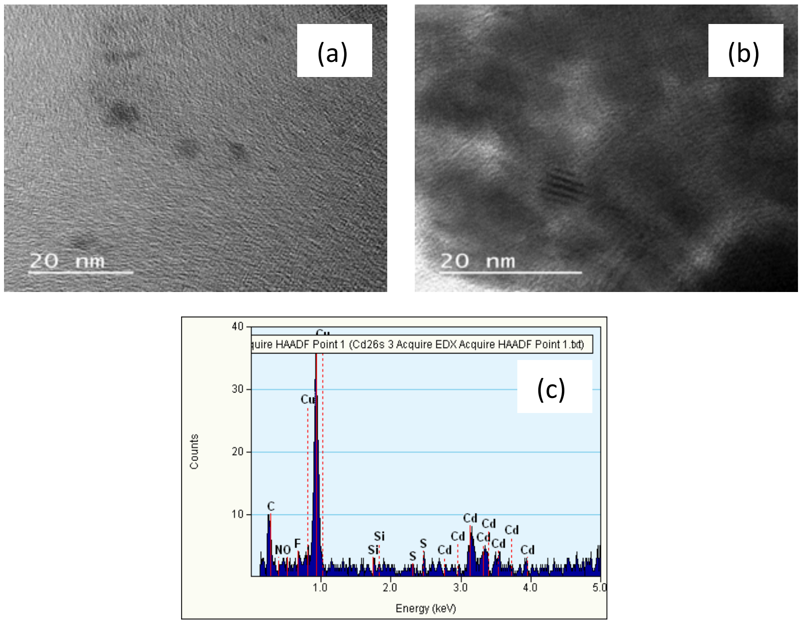

Figure 3.18: (a), (b) TEM images and (c) EDX spectrum of the Cd nanoparticles dispersed into the IL after the potentiostatic cathodic reduction at –2.6 V (vs. Ag/Ag(I)) on a GC electrode in 0.05 M Cd(TFSA)$_2$/BMPTFSA (Temperature: 30°C, Electric charge: 3 C).

Chapter 4

Electrodeposition of Selenium in a Hydrophobic Room-temperature Ionic Liquid

4.1 Introduction

Selenium (Se) is a group 16 (6A or chalcogens) element and can have different allotropic forms in the solid state. The crystalline allotropes include the hexagonal (thermodynamically stable), monoclinic, rhombohedral, orthorhombic and cubic forms. The non-crystalline allotropes can be amorphous or vitreous. The principal oxidation states of Se are +VI (selenate), +IV (selenite), 0 (elemental Se) and –II (selenide). Selenium is an important element due to its manyfold applications including electrocatalysis,[1] X-ray imaging,[2] glass deoxidizing, grain refining,[3,4] and so on. Electrically, selenium is a p-type semiconductor and exhibits photovoltaic action (the conversion of light to electric current) and photoconductivity (the variation of electrical conductivity with the intensity of light incident on the semiconductor). Therefore, Se has been widely used in the production of photovoltaic cells.[5,6] Furthermore, such compound semiconductors containing selenium, as CdSe, ZnSe or $CuInSe_2$ (CIS),[7–9] have also been studied widely for various optoelectric applications. Various approaches including photodeposition,[10] chemical bath deposition,[11] and chemical vapor deposition[12,13] have been developed for preparation of selenium thin films. Electrodeposition is expected to be an alternative technique for preparation of Se thin films at lower cost as compared with other techniques. The electrodeposition of selenium has been studied intensively in aqueous system.[14–19] However, the deposition process of Se has been known to be complicated due to several interrelated factors, such as under potential deposition (UPD), formation of compounds with electrode materials, formation of H_2Se, coupled chemical reactions, and requirement of extreme pH conditions. Furthermore, the electrodeposition of selenium in aqueous solutions at room temperature often leads to formation of amorphous Se. Crystalline Se is able to be obtained at elevated temperature, where volatility of water becomes a serious issue from a practical point of view. Therefore, aprotic room-temperature ionic liquids (RTILs) can be used for electrodeposition of selenium due to their advantageous properties, including wide electrochemical potential window, acceptable conductivity compared to non-aqueous electrolytes and negligible vapor pressure (up to 300°C).[20–22] Several groups have investigated electrodeposition of both amorphous and crystalline selenium using different ionic liquids and selenium species. Gray crystalline Se was obtained from 1-butyl-1-methylpyrrolidinium bis(trifluoromethylsulfonyl)amide containing $SeCl_4$ above 100°C, whereas red amorphous Se was found at room-temperature.[5] Electrodeposition of the polycrystalline Se film was successfully performed in 1-ethyl-3-methylimidazolium chloride-tetrafluoroborate at 30°C.[23] The electrochemical behavior, morphology and structure of Se deposits have been reported to be influenced by Se(IV) species in 1-ethyl-3-methylimdazolium tetrafluoroborate/chloride[24] and zinc chloride-1-ethyl-3-methylimdazolium chloride ionic liquid.[8] Recently, selenium electrodeposition has been studied in 1-butyl-1-methylpyrrolidinium and 1-ethyl-3-methylimidazolium trifluoromethylsulfonate containing H_2SeO_3 with H_2O as a co-solvent (5 vol%) in open air conditions at various temperatures.[25,26] *In situ* UV-vis spectroelectrochemistry of diethyl selenite in 1-propyl-1-methylpiperidinium bis(trifluoromethylsulfonyl)amide revealed deposition of amorphous selenium consisting of Se_8 rings and polymeric Se chains.[27] The previous studies indicate that electrodeposition of Se is quite complicated and that the morphology and structure of Se deposits are affected by Se species, ionic liquids and temperature.

In the present study, the electrodeposition of selenium was investigated in BMPTFSA using $SeCl_4$ as the source of Se species. Due to various oxidation states of Se and weak Lewis acidity of $SeCl_4$, $SeCl_4$ dissolved in IL may form several different species. $SeCl_4$ could form stable chloro-complex in the presence of excess chloride in BMPTFSA. Therefore, the electrochemical behavior of selenium was also investigated in BMPTFSA containing excess chloride. The coordination environment of the dissolved Se(IV) species in BMPTFSA containing excess chloride was also studied using Raman spectroscopy.

4.2 Experimental

4.2.1 Preparation of Electrolyte

4.2 1.1 Preparation of $SeCl_4$/BMPTFSA

A calculated amount of $SeCl_4$ was dissolved into BMPTFSA to obtain 0.01 M $SeCl_4$/BMPTFSA. The mixture was stirred several days at room temperature. A pale yellowish electrolyte was obtained.

4.2.1.2 Preparation of $SeCl_4$/BMPCl/BMPTFSA

BMPTFSA containing 0.04 M $SeCl_4$ and 0.15 M BMPCl was prepared by dissolving a calculated amount of $SeCl_4$ and BMPCl into BMPTFSA. The mixture was stirred several days at 60°C. A yellow transparent electrolyte was obtained.

4.2.2 Solvation Study

Raman spectra of BMPTFSA with and without $SeCl_4$ and BMPCl were obtained using a Raman spectrometer equipped with Nd:YAG laser operating at 532 nm.

4.2.3 Characterization of the Deposits

All the electrochemical measurements were conducted with a single-compartment three-electrode cell whereas, the electrodeposition experiments were conducted with a double-compartment three-electrode cell as described in chapter 2. The electrodeposits washed with dehydrated acetonitrile and dried in the air were characterized by SEM, EDX, XRD, XPS and Raman spectrometer. Raman spectra of the deposits were conducted using a laser operating at 532 nm.

4.3 Results and Discussion

4.3.1. Electrochemical Behavior of Se(IV) in BMPTFSA

Figure 4.1 shows the linear sweep voltammogram (LSV) of a GC electrode in BMPTFSA containing 0.01 M $SeCl_4$ at 25°C. The potential was swept to the negative direction from the open circuit potential at the scan rate of 50 mV s^{-1}. The LSV shows three reduction peaks C1, C2 and C3. $SeCl_4$ has been reported to dissolve as $[SeCl_3]^+$ with liberation of Cl^- in acetonitrile.[28] The peak potential of C2 is close to that for reduction of $[SeCl_6]^{2-}$ to Se(0), as described below. Therefore, dissolution of $SeCl_4$ in BMPTFSA without Cl^- is considered explained by the following reaction.

$$3SeCl_4 \rightarrow 2[SeCl_3]^+ + [SeCl_6]^{2-} \qquad (4.1)$$

The peak C3 was able to be assigned to further electroreduction of Se to Se (–II), as described below. Formation of $[SeCl_6]^{2-}$ is expected to be favored in the presence of excess chloride ions. Therefore, electroreduction of $[SeCl_6]^{2-}$ to Se(0) (peak C2) and Se(0) to Se (–II) (peak C3) has been studied in details in BMPTFSA with excess chloride ions. Since potentiostatic bulk electrolysis at the peak potential of C1 resulted in deposition of elemental Se (data shown below), the peak C1 is considered to be ascribed to reduction of $[SeCl_3]^+$ to Se(0). In the present section, the electroreduction of $[SeCl_3]^+$ to Se(0) has been focused. Figure 4.2 shows the cyclic voltammograms of a GC electrode in 0.01 M $SeCl_4$/BMPTFSA at various scan rates. In addition to the cathodic current peak due to the electroreduction of $[SeCl_3]^+$ to Se(0), an anodic current peak was also observed within the scanned potential region of the cyclic voltammograms, which may be due to the dissolution of the deposited selenium. However, according to the literature,[29] the anodic current peak A1 at about 0.2 V could also be due to the oxidation of Cl^- to Cl_3^-. Figure 4.3 compares the cyclic voltammograms of a GC electrode in BMPTFSA containing 0.01 M $SeCl_4$ and that in BMPTFSA containing 0.05 M BMPCl at the scan rate of 10 mV s^{-1}. The cyclic voltammograms of a GC electrode in 0.05 M BMPCl/BMPTFSA gave an anodic current peak assignable to the oxidation of Cl^- to Cl_3^- at about 0.6 V.[29] Therefore, the observed anodic current peak at about 0.2 V in 0.01 M $SeCl_4$/BMPTFSA system can be assigned to the dissolution of the deposited selenium.

The large separation between the cathodic and anodic peak potentials, as seen in Figure 4.2, and the shifting of the peak potential of the cathodic peak C1 towards negative direction with an increase in the scan rates suggested the irreversible nature of the electroreduction process of Se(IV) to Se(0) on a GC electrode. Figure 4.4 shows the dependence of the cathodic peak potential, E_{pc}, on the logarithm of scan rate for the reduction of Se(IV) on a GC electrode. The peak potential was found to depend linearly on the logarithm of scan rates as shown in Figure 4.4, indicating the electrode reaction can be regarded as electrochemically irreversible.[30] The product of the transfer coefficient, α, and the number of electrons in the rate-determining process, n_a, was estimated to be 0.28 from the slope according to the eq. 3.4.

The diffusion coefficient of $[SeCl_3]^+$ can be roughly estimated to be 1.5×10^{-7} $cm^2\ s^{-1}$ from the following relation between the peak current density j_p, and the square root of scan rate, as plotted in Figure 4.5.

$$j_{\mathrm{p}} = 2.99\times10^{5} n(\alpha n_{\mathrm{a}})^{1/2} C D^{1/2} v^{1/2} \tag{4.2}$$

The diffusion coefficient was further estimated using chroamperommetric technique. Figure 4.6 shows the chronoamperograms (*j-t*) of a GC electrode in 0.01 M $SeCl_4$/BMPTFSA at the step potential of –0.9 V. The current density was found to decrease and gradually approaches to a steady-sate value with the elapse of time, indicating the reduction of Se(IV) satisfied the Cottrell's criteria and can be regarded as the diffusion-limited process. The diffusion coefficient of $[SeCl_3]^+$ was calculated from the chronoamperometric data using the Cottrell's equation (eq. 3.5). The inset of the Figure 4.6 shows the Cottrell plot for the chronoamperogram of a GC electrode in 0.01 M $SeCl_4$/BMPTFSA at –0.9 V. From the slope of the Cottrell plot, the diffusion coefficient of $[SeCl_3]^+$ at 25°C was estimated to be 1.9×10^{-7} cm^2 s^{-1}. The diffusion coefficient values of $[SeCl_3]^+$ estimated by CV and chronoamperometric analyses were listed in Table 4.1 together with those of the tetra-chlorocomplexes of some other metals.

Table 4.1: Diffusion coefficients of $[SeCl_3]^+$ and $[MCl_4]^{-/2-}$ (M = Pd and Fe) in BMPTFSA at 25°C.

Species	**D, × 10^7 cm^2 s^{-1}**	**Method**	**Ref.**
$[SeCl_3]^+$	1.5	CV	This work
	1.9	CA	This work
$[PdCl_4]^{2-}$	1	CV	31
	0.92	CP	31
	1.2	CA	31
$[FeCl_4]^{2-}$	0.66 ± 0.02	CA	32
$[FeCl_4]^-$	1.3 ± 0.1	CA	32

*CV=Cyclic Voltammetry; CA=Chronoamperometry; CP=Chronopotentiometry

The diffusion coefficient of $[SeCl_3]^+$ seems to be larger than those of the tetra-chlorocomplexes of some other metals. According to Stokes–Einstein relation, the diffusion coefficient is inversely proportional to the size of the diffusing species. The size of the $[SeCl_3]^+$ is expected to be smaller than those of the $[MCl_4]^{-/2-}$ (M = Pd and

Fe). As a result, the diffusion coefficient value of $[SeCl_3]^+$ could be larger than those of the $[MCl_4]^{-/2-}$ (M = Pd and Fe).

4.3.2 Electrodeposition of Se in BMPTFSA

Electrodeposition of selenium was performed on a GC substrate in 0.01 M $SeCl_4$/BMPTFSA at –0.6 V. The deposit obtained at 25°C was reddish metallic gray. Figure 4.7 shows the SEM images of the deposit. The electrodeposit was characterized by EDX and XRD. Figure 4.8 shows the EDX spectrum and XRD pattern of the electrodeposited selenium on a GC electrode in 0.01 M $SeCl_4$/BMPTFSA at –0.6 V. In the EDX spectrum of the deposit, the signal attributed to Se was clearly observed in addition to that attributed to carbon derived from the GC substrate. However, in the XRD pattern only one peak was observed at 29.6° assignable to the (101) diffraction of hexagonal phase of Se (JCPDS-06-0362). Therefore, the electrodeposit was further analyzed by XPS. Figure 4.9 shows the XPS spectrum of the electrodeposit. The presence of characteristic peaks of the metallic selenium in the XPS spectrum of the deposit confirms the deposition of metallic selenium.

The solubility of $SeCl_4$ in BMPTFSA at room temperature was estimated to be 23 mM by ICP-OES measurement and that in BMPTFSA with 150 mM BMPCl was estimated to be 40 ± 2 mM. Electrodeposition of selenium was further investigated in BMPTFSA in the presence of excess chloride ions.

4.3.3 Dissolved Species of Se(IV) in BMPCl/BMPTFSA System

The coordination environment is an important factor for the electrochemical behavior of metal ions in ILs. Figure 4.10 shows the Raman spectra of neat BMPTFSA and BMPTFSA containing 0.04 M $SeCl_4$ and 0.15 M BMPCl. Raman spectrum of BMPTFSA containing 0.04 M $SeCl_4$ and 0.15 M BMPCl shows Raman bands at 151, 237 and 288 cm^{-1}. The Raman bands for an octahedrally coordinated chlorocomplex of Se(IV), $[SeCl_6]^{2-}$, in solid and liquid states are listed in Table 4.2.[28,33] Since the observed Raman bands in BMPTFSA containing 0.04 M $SeCl_4$ and 0.15 M BMPCl were consistent with those of $[SeCl_6]^{2-}$ as listed in Table 4.2, the dissolved species of Se(IV) in BMPTFSA containing $SeCl_4$ with excess chloride ions was identified as $[SeCl_6]^{2-}$, which forms according to the eq. 4.3. The small difference in the observed Raman band positions compared to those listed in Table 4.2 may arise due to the interaction of the octahedral complex with the IL.

$$SeCl_4 + 2Cl^{-} \rightarrow [SeCl_6]^{2-} \qquad (4.3)$$

Table 4.2: Raman bands of $[SeCl_6]^{2-}$ in BMPTFSA containing 0.04 M $SeCl_4$ and 0.15 M BMPCl together with those in solid and liquid samples reported in literature.

	$\nu_1(A_{1g})$ (cm^{-1})	**$\nu_2(E_g)$ (cm^{-1})**	**$\nu_2(F_{2g})$ (cm^{-1})**	**Ref.**
$SeCl_4$ in BMPCl/BMPTFSA	288	237	151	This work
K_2SeCl_6 (solid)	299	255	165	28,33
Rb_2SeCl_6 (solid)	290	248	164	33
Cs_2SeCl_6 (solid)	280	242	162	33
$[SeCl_6]^{2-}$ in CH_3CN	286	257	—	33

4.3.4. Electrochemical Behavior of Se(IV) in BMPCl/BMPTFSA System

Figure 4.11 shows the cyclic voltammograms of a GC electrode in BMPTFSA, BMPTFSA containing 0.15 M BMPCl and BMPTFSA containing 0.04 M $SeCl_4$ and 0.15 M BMPCl at 25°C. The potentials were initially swept to the negative direction from the open circuit potentials at the scan rate of 50 mV s^{-1}. The cyclic voltammogram of 0.04 M $SeCl_4$ and 0.15 M BMPCl in BMPTFSA (Figure 4.11(c)) shows three cathodic peaks C1, C2 and C3 during the cathodic scan, and three anodic peaks A1, A2 and A3 during the anodic scan. The cathodic current peak C1 was assigned to reduction of $[SeCl_6]^{2-}$ to Se(0) since the deposit obtained by the potentiostatic electrolysis at C1 was confirmed as metallic Se by various techniques, as described below. Thus, the cathodic reaction for the peak C1 is represented by the following four-electron transfer reaction.

$$[SeCl_6]^{2-} + 4e^{-} \rightarrow Se + 6Cl^{-} \qquad (4.4)$$

Se is known to be further reduced to Se(–II).[8,26] However, Se(–II) is expected to react with $[SeCl_6]^{2-}$ present in the IL. In order to examine the redox reaction between Se(0) and Se(–II), cyclic voltammetry of Se deposited on a GC electrode in the IL was conducted in BMPTFSA with and without 0.15 M BMPCl, as shown in Figure 4.12. Although no cathodic and anodic current peaks were observed in the potential range from –2.0 to –1.0 V on a GC electrode in BMPTFSA and BMPTFSA containing 0.15 M BMPCl, as shown in Figure 4.11(a) and 4.11(b), respectively, a cathodic current peak was observed at about –1.8 V, which was close to the peak potential of C3 in Figure 4.11(c), for Se deposited on a GC electrode in both ILs without $[\mathrm{SeCl_6}]^{2-}$. Thus, the cathodic current peak at about –1.8 V was ascribed to reduction of Se(0) to Se(–II), represented as follows.

$$\mathrm{Se(0)} + 2e^- \rightarrow \mathrm{Se(-II)} \qquad (4.5)$$

The anodic current peak A* at about –1.2 V was able to be attributed to anodic oxidation of Se(–II) to Se(0). Little difference in the potentials of the cathodic and anodic current peaks suggested little influence of free $\mathrm{Cl^-}$ on the dissolved species of Se(–II). On the other hand, the anodic peak A* was not found in the presence of $[\mathrm{SeCl_6}]^{2-}$ as can be seen in Figure 4.11(c), probably due to proportionation reaction of Se(–II) and $[\mathrm{SeCl_6}]^{2-}$, as represented by the following reaction.[18,25]

$$2\mathrm{Se(-II)} + [\mathrm{SeCl_6}]^{2-} \rightarrow 3\mathrm{Se(0)} + 6\mathrm{Cl^-} \qquad (4.6)$$

Therefore, the cathodic current peak C3 at about –1.8 V in Figure 4.11(c) was ascribed to reduction of deposited Se(0) to Se(–II), which reduces $[\mathrm{SeCl_6}]^{2-}$ in the IL to form Se(0) according to eq. (4.6). The overall reaction is identical to eq. (4.4). On the other hand, it was difficult to identify the reaction for the cathodic current peak C2 at about –1.6 V, which may be related to reduction of some oxychloro species of Se because of the high reactivity of $\mathrm{SeCl_4}$ with moisture.[8] The similar cathodic current peak was also observed in 1-ethyl-3-methylimidazolium trifluoromethylsulfonate containing $\mathrm{SeCl_4}$.[25]

The anodic current peak A2 at about 0.6 V was assigned to oxidation of $\mathrm{Cl^-}$ to $\mathrm{Cl_3^-}$ since the similar anodic current peak was also observed in BMPTFSA containing BMPCl, as shown in Figure 4.11(b).[29] The anodic current peaks A1 and A3 at about 0.2 and 1.0 V, respectively, were considered to be related to anodic oxidation of Se. The anodic current peak A1 was observed in the presence of free $\mathrm{Cl^-}$, as shown in Figures 4.11(b) and 4.11(c), while the anodic current peak A3 was observed regardless of the presence of free $\mathrm{Cl^-}$, as seen in Figures 4.11(c) and 4.12(a). Thus, the anodic current peak A1 was considered to be assigned to oxidation of Se to $[\mathrm{SeCl_6}]^{2-}$. On the other hand, the anodic current peak A3 might be due to oxidation of Se to some Se species other than $[\mathrm{SeCl_6}]^{2-}$ since the local concentration of free $\mathrm{Cl^-}$ at the electrode surface was expected to be low during the cyclic voltammetry at the peak potential of A3 due to consumption of free $\mathrm{Cl^-}$ by the preceding anodic reactions represented by A1 and A2. However, further study is necessary to clarify the anodic reactions of Se in this system. Figure 4.13 shows the linear sweep voltammograms of a GC electrode in BMPTFSA containing 0.04 M $SeCl_4$ and 0.15 M BMPCl at various scan rates. The peak potential of the cathodic wave C1 was shifted to the more negative side with an increase in the scan rate, suggesting the irreversible nature of the electrode reaction between $[SeCl_6]^{2-}$ and Se(0). However, the quantitative analysis of the cyclic voltammograms was avoided because of ohmic drop due to low conductivity of the IL and the possibility of existence of other Se(IV) species, as described above. The irreversibility of the electrode reaction is also demonstrated by the large separation of the potentials between cathodic and anodic peaks, as seen in Figure 4.11(c).

4.3.5 Electrodeposition of Se in BMPCl/BMPTFSA System

Electrodeposition of selenium was performed on a GC substrate in BMPTFSA containing 0.04 M $SeCl_4$ and 0.15 M BMPCl at –1.4 V. The deposit obtained at 25°C was reddish metallic grey while that at 50°C was metallic grey. Figure 4.14(a) shows the EDX spectra of the deposits. The signal attributed to Se was clearly observed in the deposits obtained at 25 and 50°C in addition to that attributed to carbon derived from the GC substrate. Figure 4.14(b) shows the XRD patterns of the deposits obtained at 25 and 50°C. Two peaks at 23.5 and 29.6° in the deposit obtained at 50°C were assigned to (100) and (101) diffractions of hexagonal phase of Se (JCPDS-06-0362). An additional peak at 20.7° in addition to the peaks attributed to hexagonal phase of Se was observed in the deposit obtained at 25°C. The peak was assignable to (112) diffraction of monoclinic phase of Se (JCPDS 24-1202) since deposition of polymorphic Se has been reported at room temperature.[23,25,26] Figure 4.15 shows the SEM images of the deposits obtained at 25 and 50°C. Small particles and needles were observed in the deposit obtained at 25°C, while more compact and leaf or flower-like particles were observed in the deposit obtained at 50°C. The difference in the crystal phases and morphology of Se deposits at different temperature may be related to the rate of crystal growth and/or electrical conductivity of Se. Se is a semiconductor with a low electrical conductivity at room temperature. However, the electrical conductivity of Se increases with elevating temperature above 40°C,[34] resulted in facile crystal growth and formation of coarser particles by cathodic reduction of $[SeCl_6]^{2-}$ on the deposited Se. In addition, the steady-state current density during the potentiostatic electrodeposition at 50°C was higher than that at 25°C, reflecting the difference in the electronic conductivity of Se in addition to a decrease in the viscosity of the IL.

Figure 4.16 shows the Raman spectra of the deposits. Two Raman bands at 144 and 236 cm^{-1} observed in the deposits obtained at 25 and 50°C were consisted with those observed for hexagonal (trigonal) Se, 143(E), 233(E) and 237(A1) cm^{-1}.[27,35,36] Since the Raman band typical to amorphous Se at 250 cm^{-1} (Se_8, A1, E2) was not observed in Figure 4.16, the deposits were considered mainly composed of crystalline Se. Figure 4.17 shows the XPS spectra of the electrodeposits. The presence of characteristic peaks of the metallic selenium in the XPS spectrum of the deposits confirm the deposition of metallic selenium. Figure 4.18 shows the deconvoluted XPS spectra of the 3d region of Se for the deposits obtained at 25 and 50°C. These XPS spectra were taken after Ar^+ etching for 15 sec. The distorted peak was deconvoluted to two components corresponding to Se $3d_{5/2}$ and Se $3d_{3/2}$ orbitals of metallic Se, by the least-square fitting.[27] It is worth mentioning there was no additional peak assignable to selenium oxide, suggesting high purity of the deposited selenium.

4.4 Conclusions

The electrodeposition of metallic Se was possible in an amide-type RTIL, BMPTFSA. Electrochemical reaction of Se(IV)/Se on a GC electrode was an electrochemically irreversible process. Diffusion coefficient of Se(IV) was estimated to be $\sim 10^{-7}$ cm^2 s^{-1} at 25°C. The solubility of $SeCl_4$ in BMPTFSA with excess Cl^- was higher than that in BMPTFSA. $SeCl_4$ was found to be dissolved in the IL with excess Cl^- by forming $[SeCl_6]^{2-}$. Electrochemical reduction of $[SeCl_6]^{2-}$ was possible in the IL, resulting in deposition of metallic Se. Electrodeposition of crystalline selenium was confirmed at 25°C. Compact and granular deposits were able to be obtained by elevating temperature at 50°C, where the electrical conductivity of Se increased compared with room temperature. Reduction of Se to Se(–II) was confirmed at the potential more negative than the reduction of $[SeCl_6]^{2-}$. However, proportionation reaction of Se(–II) and $[SeCl_6]^{2-}$ led to deposition of Se.

4.5 References

1. L. Colmenares, Z. Jusys, and R. J. Behm, *J. Phys. Chem. C*, **111**, 1273–1283 (2007).
2. S. Kasap, J. B. Frey, G. Belev, O. Tousignant, H. Mani, L. Laperriere, A. Reznik, and J. A. Rowlands, *Phys. Status Solidi Basic Res.*, **246**, 1794–1805 (2009).
3. V. S. Saji and C. W. Lee, *Rsc Adv.*, **3**, 10058–10077 (2013).
4. W. C. Butterman and J. R. D. Brown, *U.S. Geological Survey, Open-File Report 03-018, Mineral Commodity Profile - Selenium*, (2004).
5. S. Zein El Abedin, A. Y. Saad, H. K. Farag, N. Borisenko, Q. X. Liu, and F. Endres, *Electrochim. Acta*, **52**, 2746–2754 (2007).
6. N. M. Dimitrijevic and P. V. Kamat, *Langmuir*, **4**, 782–784 (1988).
7. U. Farva and C. Park, *Mater. Lett.*, **64**, 1415–1417 (2010).
8. C. Pai, C.-J. Su, Y.-T. Hsieh, P.-Y. Chen, and I.-W. Sun, *J. Electrochem. Soc.*, **162**, D243–D249 (2015).
9. H. W. Schock, *Appl. Surf. Sci.*, **92**, 606–616 (1996).
10. J. Pola, Z. Bastl, J. Subrt, and A. Ouchi, *Appl. Organomet. Chem.*, **14**, 715–720 (2000).
11. K. Bindu, M. Lakshmi, S. Bini, C. S. Kartha, K. P. Vijayakumar, T. Abe, and Y. Kashiwaba, *Semicond. Sci. Technol.*, **17**, 270–274 (2002).
12. P. Nagels, E. Sleeckx, R. Callaerts, and L. Tichy, *Solid State Commun.*, **94**, 49–52 (1995).
13. E. Chatterjee and S. P. Sen Gupta, *J. Mater. Sci. Lett.*, **5**, 559–561 (1986).
14. A. V. Hippel and M. C. Bloom, *J. Chem. Phys.*, **18**, 1243–1251 (1950).
15. A. K. Graham, H. L. Pinkerton, and H. J. Boyd, *J. Electrochem. Soc.*, **106**, 651–654 (1959).
16. M. S. Kazacos, *J. Electrochem. Soc.*, **127**, 869–873 (1980).
17. C. Wei, N. Myung, and K. Rajeshwar, *J. Electroanal. Chem.*, **375**, 109–115 (1994).
18. Y. Lai, F. Liu, J. Li, Z. Zhang, and Y. Liu, *J. Electroanal. Chem.*, **639**, 187–192 (2010).
19. M. F. Cabral, V. A. Pedrosa, and S. A. S. Machado, *Electrochim. Acta*, **55**, 1184–1192 (2010).
20. H. Ohno, Ed., *Electrochemical Aspects of Ionic Liquids*, John Wiley & Sons, Inc., New Jersey, (2005).
21. F. Endres and S. Zein El Abedin, *Phys. Chem. Chem. Phys.*, **8**, 2101–2116 (2006).

22. A. P. Abbott and K. J. McKenzie, *Phys. Chem. Chem. Phys.*, **8**, 4265–4279 (2006).
23. L.-H. Chou, I.-W. Sun, and C. L. Hussey, *Molten Salts Ion. Liq. 17*, **33**, 575–579 (2010).
24. M. Steichen and P. Dale, *Electrochem. Commun.*, **13**, 865–868 (2011).
25. A. Abdel Aal, F. Voigts, D. Chakarov, and F. Endres, *J. Solid State Electrochem.*, **16**, 3027–3036 (2012).
26. A. A. Aal, F. Voigts, D. Chakarov, and F. Endres, *Electrochim. Acta*, **59**, 228–236 (2012).
27. D. W. Redman, S. Murugesan, and K. J. Stevenson, *Langmuir*, **30**, 418–425 (2014).
28. I. R. Beattie and H. Chudzynska, *J. Chem. Soc. A Inorganic, Phys. Theor.*, 984–990 (1967).
29. Q. Zhang, Y. Hua, and R. Wang, *Electrochim. Acta*, **105**, 419–423 (2013).
30. A. J. Bard and L. R. Faulkner, *Electrochemical Methods, Fundamentals and Applications*, 2nd ed., John Wiley & Sons, Inc., New York, (2001).
31. Y. Katayama, Y. Bando, and T. Miura, *Trans. Inst. Met. Finish.*, **86**, 205–210 (2008).
32. N. Tachikawa, Y. Katayama, and T. Miura, *J. Electrochem. Soc.*, **154**, F211–F216 (2007).
33. P. J. Hendra and Z. Jovic, *J. Chem. Soc. A Inorganic, Phys. Theor.*, 600–602 (1968).
34. A. K. Sharma and B. Singh, *Proc. Indian Natn. Sci. Acad.*, **46**, 362–368 (1980).
35. G. Lucovsky, A. Mooradian, W. Taylor, G. B. Wright, and R. C. Keezer, *Solid State Commun.*, **5**, 113–117 (1967).
36. Y. M. K. Nagata, T. Ishikawa, *Jpn. J. Appl. Phys.*, **24**, 1171–1173 (1985).

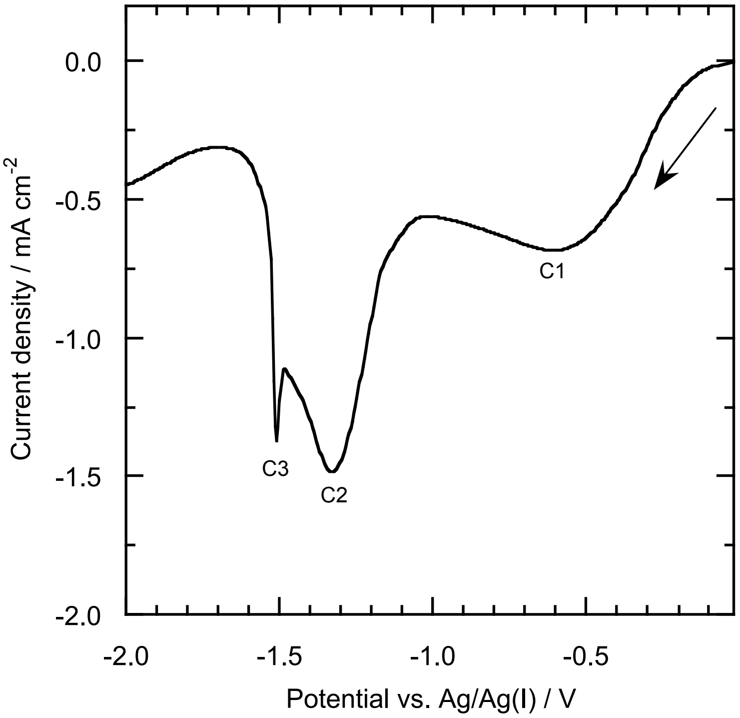

Figure 4.1: Linear sweep voltammogram of a GC electrode in 0.01 M $SeCl_4$/BMPTFSA at 25°C. Scan rate: 50 mV s^{-1}.

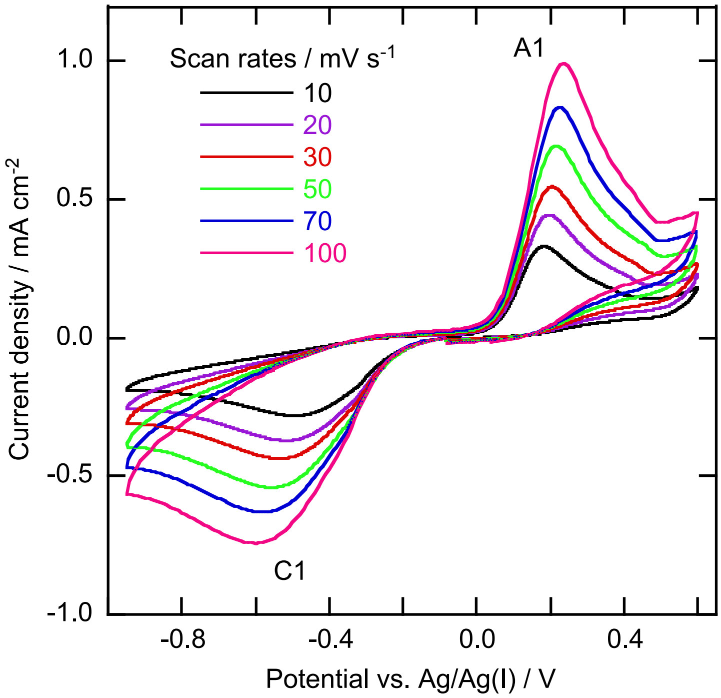

Figure 4.2: Cyclic voltammograms of a GC electrode in 0.01 M $SeCl_4$/BMPTFSA at various scan rates. Temperature: 25°C.

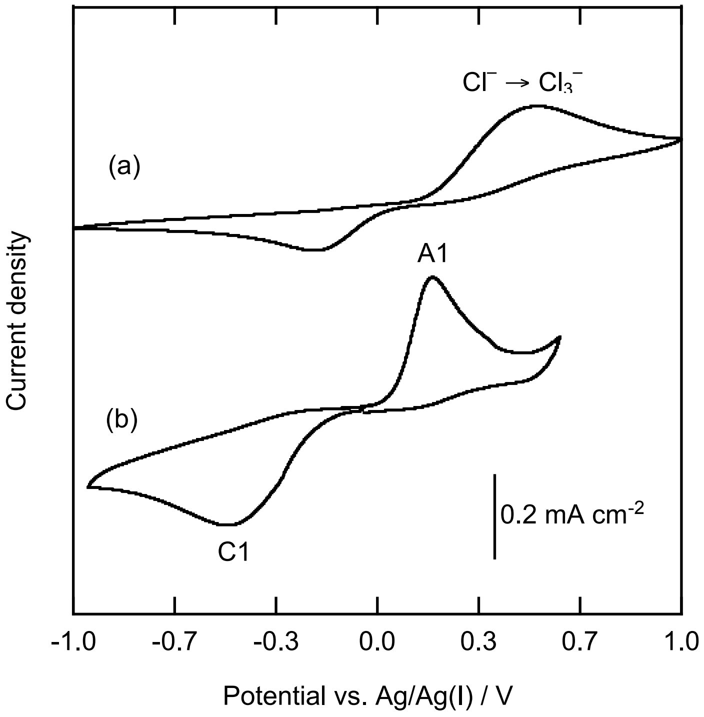

Figure 4.3: Cyclic voltammograms of a GC electrode in (a) 0.05 M BMPCl/BMPTFSA and (b) 0.01 M $SeCl_4$/BMPTFSA at the scan rate of 10 mV s^{-1}. Temperature: 25°C.

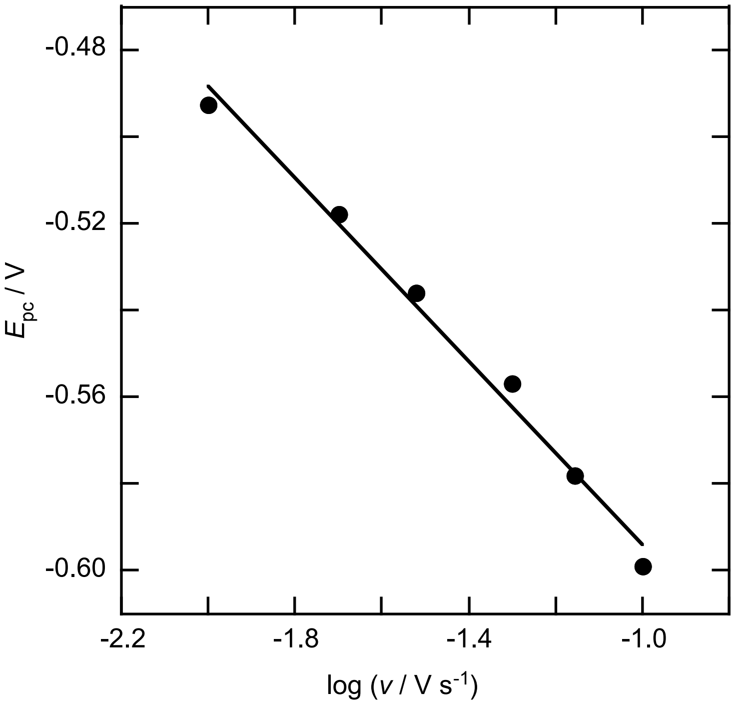

Figure 4.4: Variation of cathodic peak potentials with the logarithms of scan rates for the cyclic voltammograms of a GC electrode in 0.01 M $SeCl_4$/BMPTFSA at 25°C.

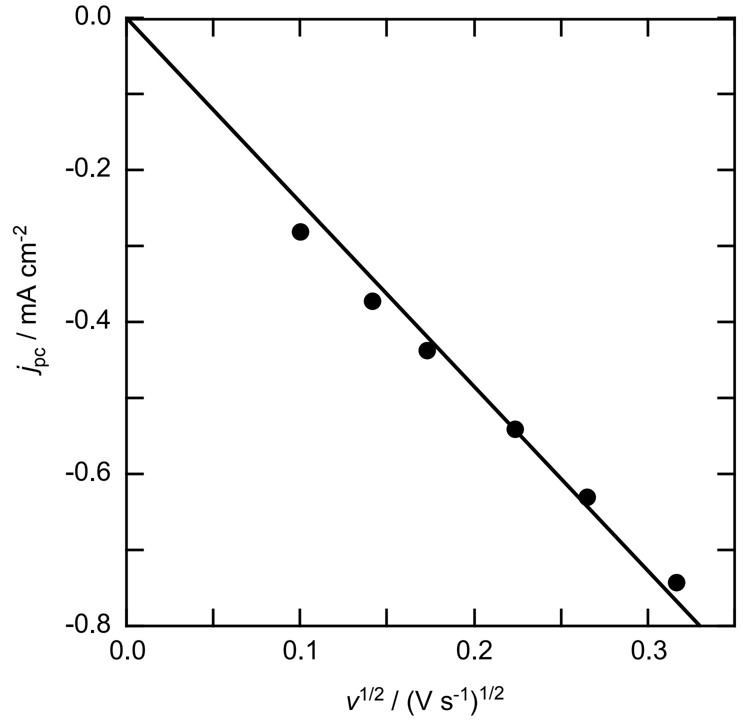

Figure 4.5: Dependence of cathodic peak current density on the square root of scan rate for the cyclic voltammograms of a GC in 0.01 M $SeCl_4$/BMPTFSA at 25°C.

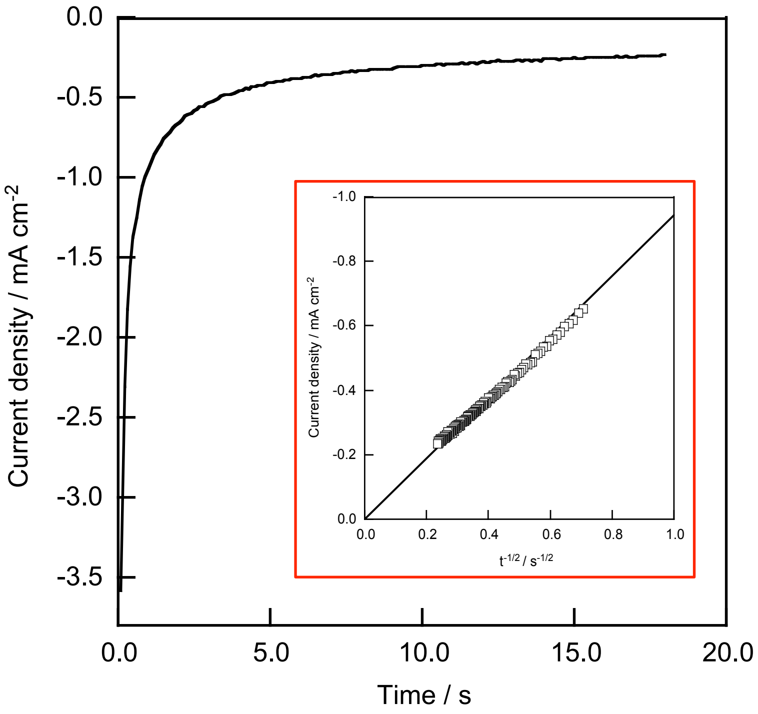

Figure 4.6: Chronoamperogram of a GC electrode in 0.01 M $SeCl_4$/BMPTFSA at the step potential of –0.9 V (Temperature: 25°C). The inset shows the Cottrell plot of the chronoamperogram.

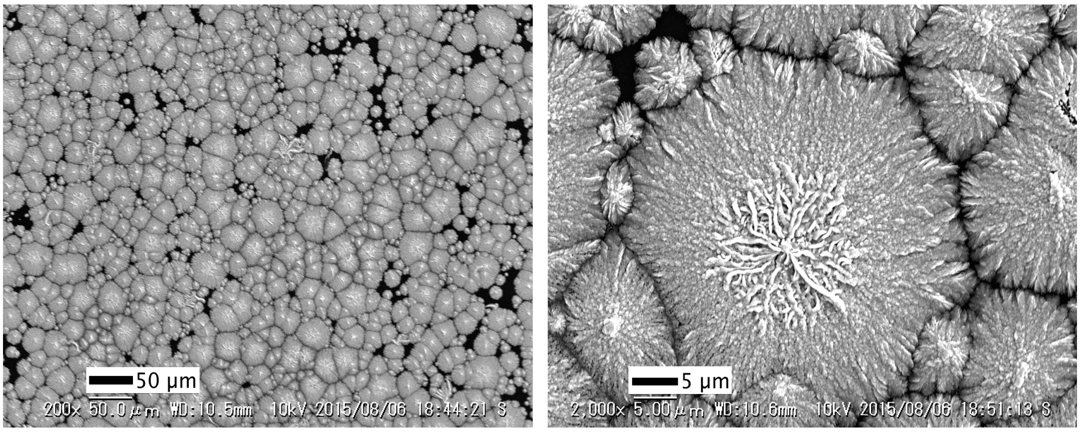

Figure 4.7: SEM images of the electrodeposits obtained by potentiostatic electrolysis on a GC electrode at −0.6 V in 0.01 M $SeCl_4$/BMPTFSA at 25°C. Electric charge: 0.8 C.

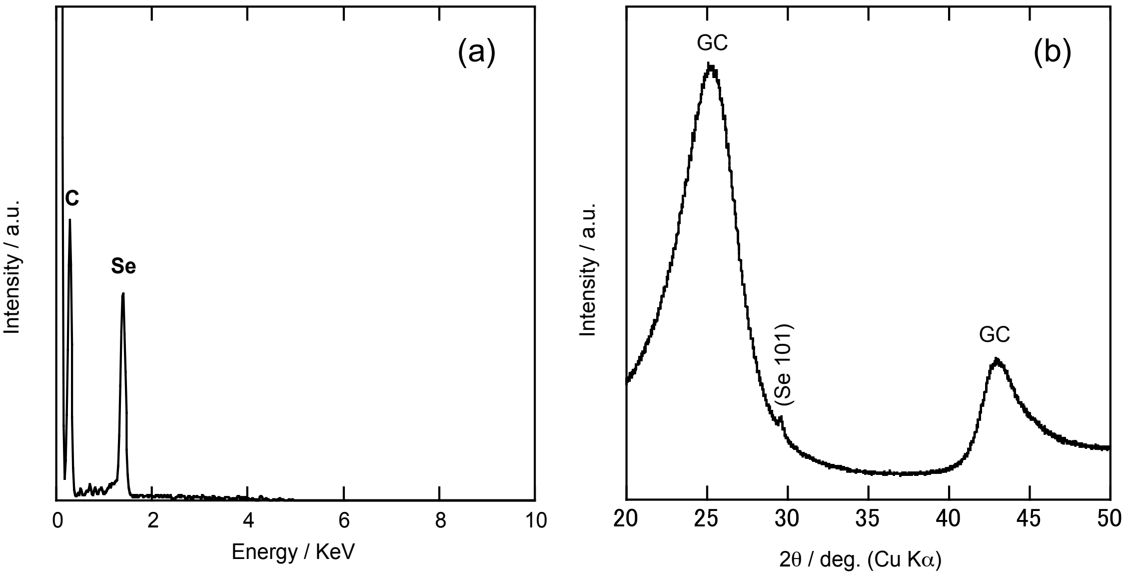

Figure 4.8: (a) EDX spectrum and (b) XRD pattern of the electrodeposit obtained by potentiostatic electrolysis on a GC electrode in 0.01M $SeCl_4$/BMPTFSA at −0.6 V (Temperature: 25°C, Electric charge: 0.8 C.).

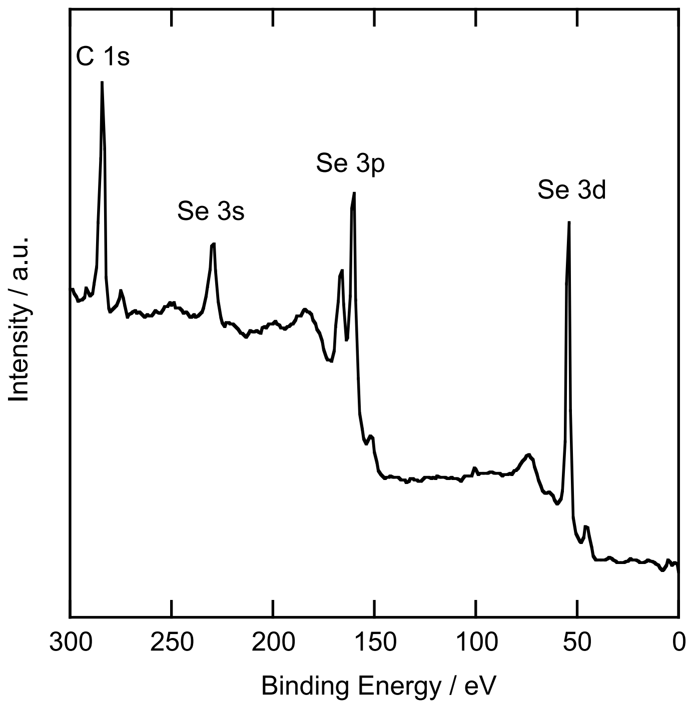

Figure 4.9: XPS spectrum of the electrodeposit obtained by potentiostatic electrolysis on a GC electrode at −0.6 V in 0.01 M $SeCl_4$/BMPTFSA at 25°C. Electric charge: 0.8 C.

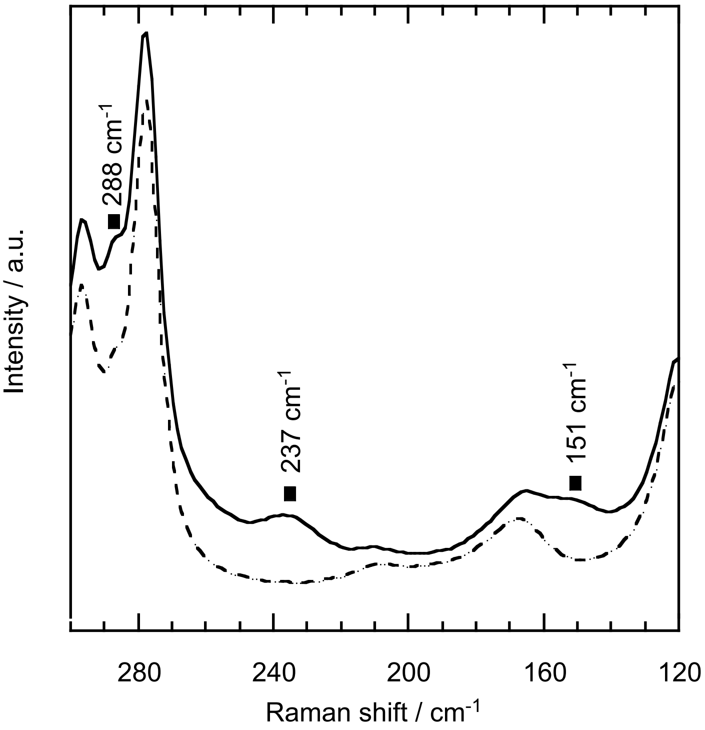

Figure 4.10: Raman spectra of BMPTFSA containing 0.04 M $SeCl_4$ and 0.15 M BMPCl (solid line) and neat BMPTFSA (dotted line) at room temperature.

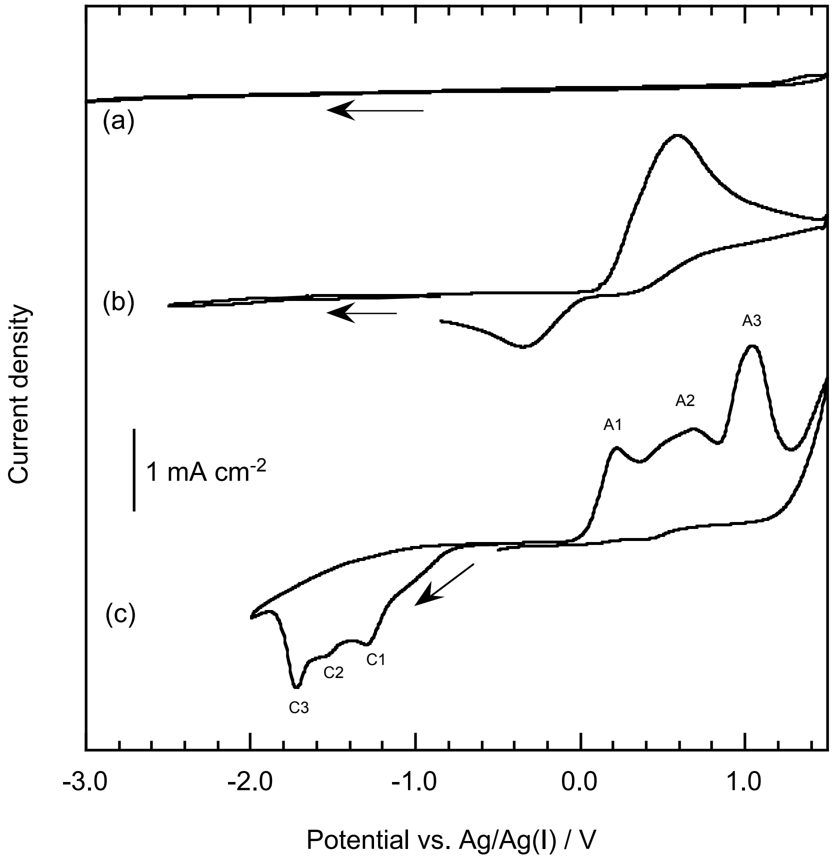

Figure 4.11: Cyclic voltammograms of a GC electrode in (a) BMPTFSA, (b) BMPTFSA containing 0.15 M BMPCl and (c) BMPTFSA containing 0.04 M $SeCl_4$ and 0.15 M BMPCl at 25°C. Scan rate: 50 mV s^{-1}.

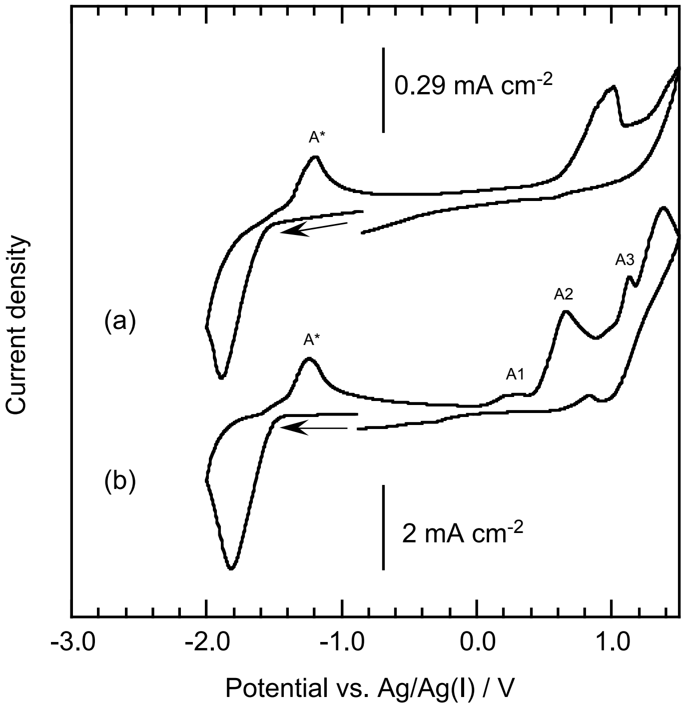

Figure 4.12: Cyclic voltammograms of Se deposited on a GC electrode in (a) BMPTFSA and (b) BMPTFSA containing 0.15 M BMPCl at the scan rate of 50 mV s^{-1}. Temperature: 25°C.

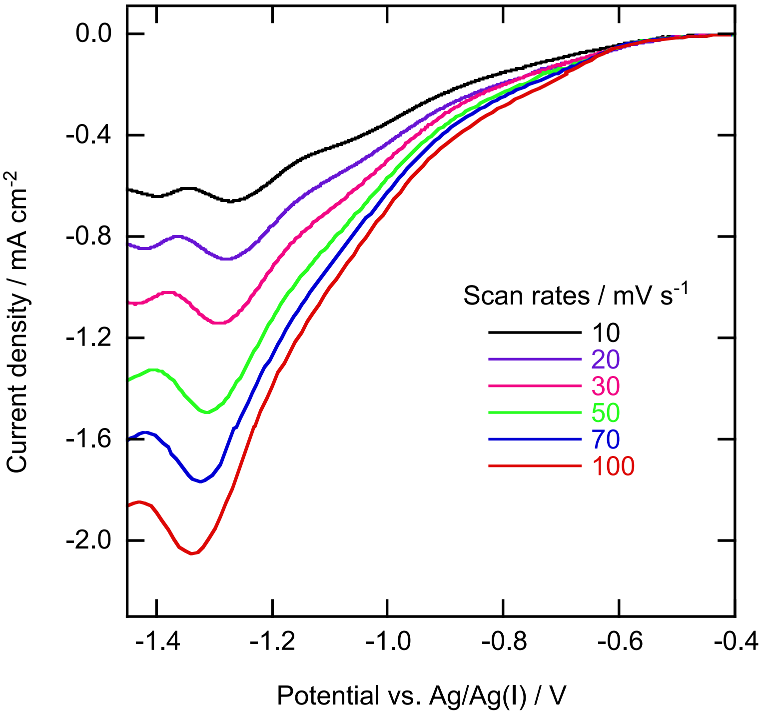

Figure 4.13: Linear sweep voltammograms of a GC electrode in BMPTFSA containing 0.04 M $SeCl_4$ and 0.15 M BMPCl at various scan rates. Temperature: 25°C.

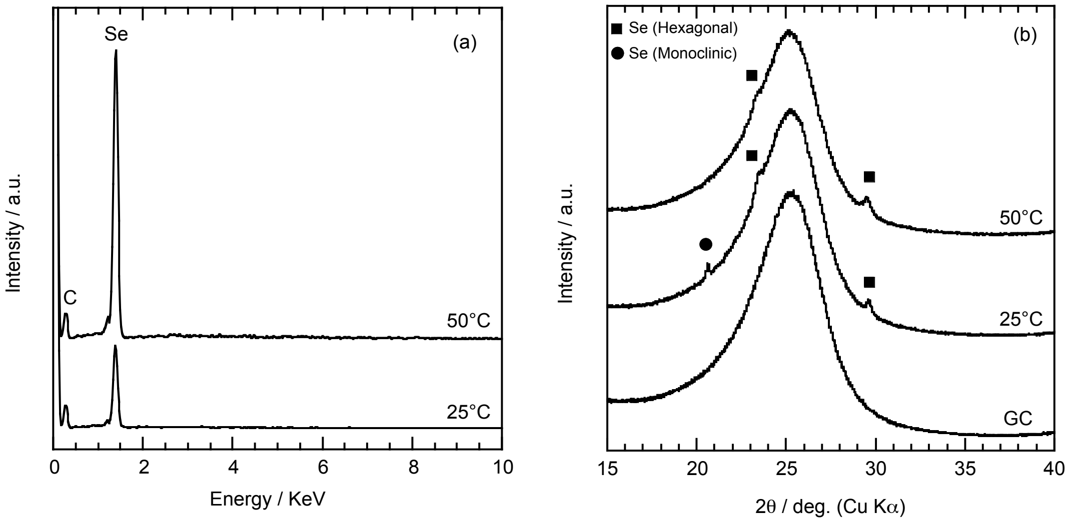

Figure 4.14: (a) EDX spectra and (b) XRD patterns of the electrodeposits obtained by potentiostatic electrolysis on a GC electrode in BMPTFSA containing 0.04 M $SeCl_4$ and 0.15 M BMPCl at –1.4 V. Electric charge: 2 C. Temperature: 25 and 50°C.

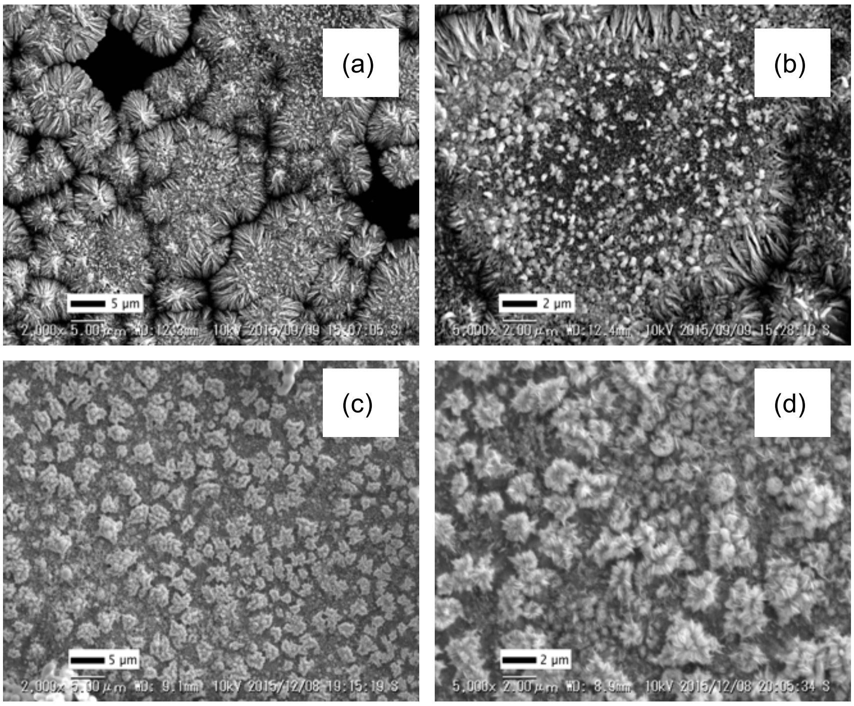

Figure 4.15: SEM images of the electrodeposits obtained by potentiostatic electrolysis on a GC electrode at –1.4 V in BMPTFSA containing 0.04 M $SeCl_4$ and 0.15 M BMPCl at (a), (b) 25°C and (c), (d) 50°C. Electric charge: 2 C.

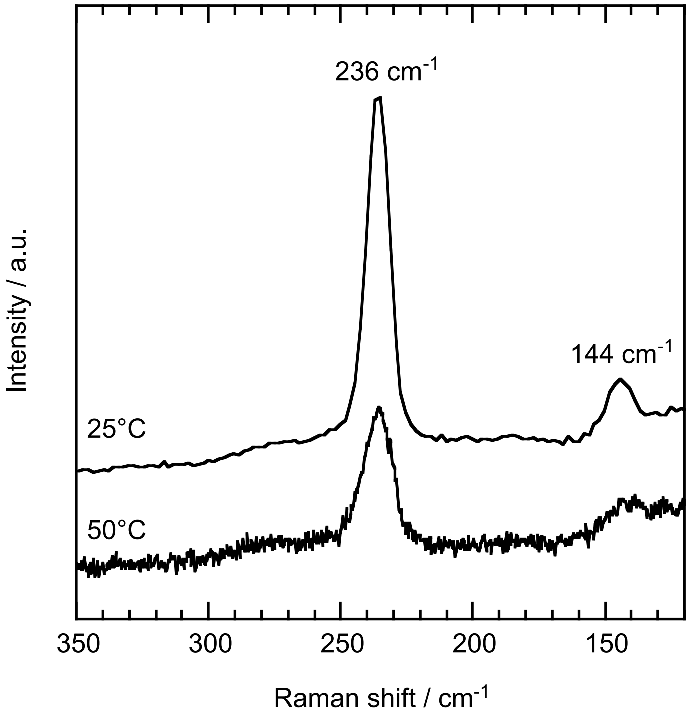

Figure 4.16: Raman spectra of the electrodeposits obtained by potentiostatic electrolysis on a GC electrode at –1.4 V in BMPTFSA containing 0.04 M $SeCl_4$ and 0.15 M BMPCl at 25 and 50°C. Electric charge: 2 C.

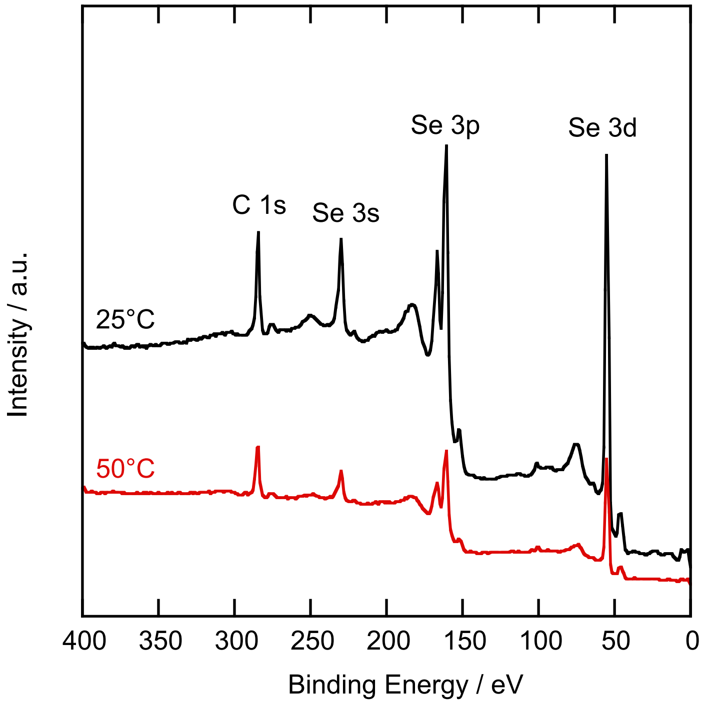

Figure 4.17: XPS spectra of the electrodeposits obtained by potentiostatic electrolysis on a GC electrode at –1.4 V in BMPTFSA containing 0.04 M $SeCl_4$ and 0.15 M BMPCl at 25 and 50°C. Electric charge: 2 C.

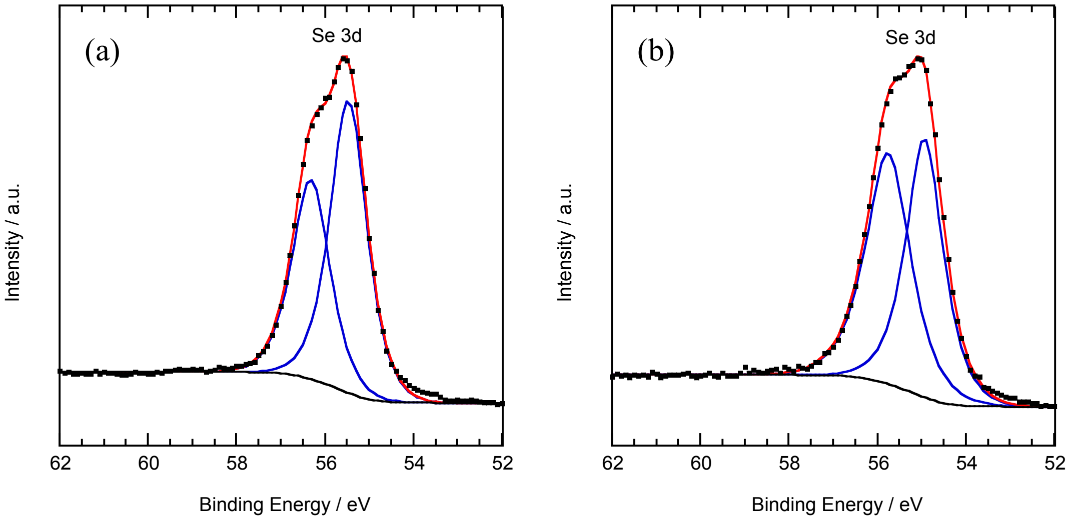

Figure 4.18: Deconvoluted XPS spectra of the Se deposits (3d region) obtained by potentiostatic electrolysis on a GC electrode at –1.4 V in BMPTFSA containing 0.04 M $SeCl_4$ and 0.15 M BMPCl at (a) 25 and (b) 50°C. Electric charge: 2 C.

Chapter 5

Electrodeposition of Cadmium from a Basic Hydrophobic Ionic Liquid

5.1 Introduction

Due to manifold applications of cadmium, the understanding of the electrochemical behavior of the Cd(II)/Cd system is important. In chapter 3, the importance and necessity of the electrodeposition of Cd in aprotic RTILs has been discussed in details. In chapter 3, the electrodeposition of metallic cadmium was successfully performed in BMPTFSA using $Cd(TFSA)_2$ as the source of Cd species. For the practical use, commercially available metal salts are generally preferable. In the present study, electrodeposition of cadmium was attempted in BMPTFSA using anhydrous $CdCl_2$, which is commercially available. $CdCl_2$ is known to dissolve as the tetrachlorocomplex in some basic room-temperature ionic liquids. Dymek et al.,[1] using NMR spectroscopy, showed that $CdCl_2$ dissolved in the basic 1-methyl-3-ethylimidazolium chloride–aluminum trichloride melt by accepting two chloride ions to form $[CdCl_4]^{2-}$. Noel and Osteryoung,[2] using pulse voltammetric technique, demonstrated that $CdCl_2$ forms $[CdCl_4]^{2-}$ in the basic 1-ethyl-3-methylimidazolium chloride–aluminum trichloride melt. Chen and Sun[3] investigated the electrochemistry of cadmium species in a basic 1-ethyl-3-methylimidazolium chloride–tetrafluoroborate room-temperature molten salt. Using amperometric titration, they have also showed that $CdCl_2$ accepts two chloride ions to form $[CdCl_4]^{2-}$. In the present study, considering the previous reports, $CdCl_2$ was dissolved in BMPTFSA with the addition of excess chloride in order to ensure the formation of a single chloro-complex in the system. In addition, with the investigation of electrodeposition of Cd using $CdCl_2$ as the source of Cd species, the possibility of formation of CdSe was also attempted in BMPTFSA in the presence of excess chloride.

5.2 Experimental

5.2.1 Preparation of Electrolyte

5.2.1.1 Preparation of $CdCl_2$/BMPCl/BMPTFSA

BMPTFSA containing 0.05 M $CdCl_2$ and 0.15 M BMPCl was prepared by dissolving a calculated amount of $CdCl_2$ and BMPCl into BMPTFSA. The electrolyte was a colorless transparent liquid at room temperature.

5.2.1.1 Preparation of $SeCl_4$/$CdCl_2$/BMPCl/BMPTFSA

BMPTFSA containing 0.02 M $SeCl_4$, 0.02 M $CdCl_2$ and 0.5 M BMPCl was prepared by dissolving a calculated amount of $SeCl_4$, $CdCl_2$ and BMPCl into BMPTFSA. The mixture was stirred several days at 50°C. A yellow transparent electrolyte was obtained.

5.2.2 Characterization of the Deposits

All the electrochemical measurements and electrodeposition experiments were conducted with a single-compartment three-electrode cell as described in chapter 2. The electrodeposits washed with dehydrated acetonitrile and dried in the air were characterized by SEM, EDX and XRD.

5.3 Result and discussion

5.3.1 Cyclic Voltammetric Study of $[CdCl_4]^{2-}$ in BMPTFSA

Figure 5.1 shows the cyclic voltammogram of a GC electrode in BMPTFSA containing 0.05 M $CdCl_2$ and 0.15 M BMPCl at the scan rate of 50 mV s^{-1}. An interesting unusual behavior with a small increase in the cathodic current below –2.3 V during the cathodic scan and followed by a cathodic and anodic current peak during the anodic scan was observed in the cyclic voltammogram. In order to understand such unusual electrochemical behavior, electrodeposition of Cd was attempted by undergoing the cathodic process at –2.3 V. In order to deposit Cd, the potential was scanned towards the cathodic direction from the open circuit potential to –2.5 V in the first place and then the potential was swept to the anodic direction and held at –2.2 V for about 2 hours. A grayish film was found on the GC substrate. XRD pattern and EDX spectrum showed the film to be metallic cadmium, as shown in Figure 5.2.

Although electrodeposition of metallic cadmium is possible from $[CdCl_4]^{2-}$ in BMPTFSA, the unusual electrochemical behavior of the $[CdCl_4]^{2-}$ species demands further electrochemical studies. Figure 5.3 shows the cyclic voltammograms of a GC electrode in BMPTFSA containing 0.05 M $CdCl_2$ and 0.15 M BMPCl at different scan rates. The shape of the cyclic voltammograms was not found to be changed significantly with the change of scan rate. For all the scan rates, the cathodic current peak during anodic scan was observed. However, at the relatively slow scan rates a cathodic current peak during cathodic scan was found at about –2.35 V. The deposit obtained by potentiostatic electroreduction at –2.35 V was confirmed as metallic Cd by XRD pattern (data shown below), suggesting the observed peak at –2.35 V was due to the reduction of Cd(II) to Cd(0). It is worth to mention that the cathodic peak current density during cathodic scan was very small compared to that observed during anodic scan, indicating hindrance of the nucleation and crystal growth process during the cathodic scan. At the negative overpotential, adsorption and orientation of the organic cations of ILs on the electrode surface has already been reported.[4,5,6] Recently, Magnussen et al.[7] investigated the potential dependent adlayer structure of the ionic liquid electrode interface using BMPTFSA. They reported that the structure of the inner layer formed by the BMP^+ changed with potential, and that a more compact inner BMP^+ layer formed at the more negative potential. In the present study, as the reduction potential of $[CdCl_4]^{2-}$ species in BMPTFSA is very negetive, a strong attraction of BMP^+ cations on the electrode surface is well expected. Therefore, the nucleation and crystal growth of cadmium during cathodic scan can be hindered due to the strong attraction and high crowding of BMP^+ cations on the electrode surface. On the other hand, the degree of interaction between the BMP^+ cations and the electrode surface is supposed to decrease during the anodic scan, facilitating the electroreduction of $[CdCl_4]^{2-}$ on the Cd nuclei formed during cathodic scan. As a result, a larger cathodic peak current was observed during the anodic scan. The anodic current peak during the anodic scan was assignable to the anodic dissolution of the deposited Cd.

The effect of temperature on the electroreduction process of $[CdCl_4]^{2-}$ was also studied. Figure 5.4 shows the cyclic voltammograms of a GC electrode in BMPTFSA containing 0.05 M $CdCl_2$ and 0.15 M BMPCl at different temperatures. The cathodic peak potentials shifted to the more positive side with elevating temperature, indicating that the overpotential for the electroreduction of $[CdCl_4]^{2-}$ decreased at higher temperature probably due to ease of nucleation. At higher temperature, a faster charge transfer process may also be a reason for the lowering of overpotential. It is worth to mention that the cathodic peak current density during the cathodic scan was found to be increased with an increase in temperature probably due to the facilitated nucleation and crystal growth process. Also the increased mobility of the electroactive species due to a decrease in viscosity at higher temperature can contribute to such increased peak current density.

Figure 5.5 shows the cyclic voltammograms of a Pt and Cd electrode in BMPTFSA containing 0.05 M $CdCl_2$ and 0.15 M BMPCl at the scan rate of 50 mV s^{-1}. The cyclic voltammogram of the Pt electrode was similar to that of GC electrode (Figure 5.1) with no cathodic current peak during cathodic scan. On the other hand, the cyclic voltammogram of the Cd electrode showed a cathodic current peak during the cathodic scan. Electrodeposition of a metal on the same metal substrate requires low energy due to no need for nucleation, resulted in a decrease in the overpotential for electrodeposition process. Although the deposition overpotential is small on the Cd substrate, the potential was negetive enough for the strong attraction of BMP^+ cations on the electrode surface. As a consequence during the anodic scan, when the degree of attraction of BMP^+ decreased, a further cathodic reduction of the $[CdCl_4]^{2-}$ was possible. Thus, a cathodic current peak was considered to increase during the anodic scan. A similar electrochemical behavior (cathodic current peak during anodic scan) of the $[CdCl_4]^{2-}$ species in a different IL, 1-butyl-3-methylimidazolium bis(trifluoromethylsulfonyl)amide (BMITFSA), was also observed as shown in Figure 5.6. However, a large cathodic current peak during cathodic scan suggests the difference in the electric double layer structure with the change of organic cation of ILs. The strength of interaction between the innermost layer of IL and the substrate as well as the electric double layer structure has been reported to be dependent on the cation type of the ionic liquid.[8]

The redox potentials of $[CdCl_4]^{2-}$/Cd in different ILs were roughly estimated and listed in Table 5.1. It can be seen from Table 5.1 that the redox potential of $[CdCl_4]^{2-}$/Cd does not change with the change of ILs, indicating the redox potentials of chlorocomplexes of metals are little affected by the ions of ILs.

Table 5.1: Redox potential, *E*, of $[CdCl_4]^{2-}/Cd$ in some ILs.

System	***E* vs. $Fc^{0/+}$ / V**	**Ref.**
BMPTFSA/BMPCl	–1.4	This work
BMITFSA/BMICl	–1.4	This work
EMICl/$AlCl_3$	–1.4	9
EMICl/BF_4	–1.4	10

5.3.2 Electrodeposition of Cd in BMPTFSA/BMPCl

Potentiostatic electrodeposition of cadmium on a GC substrate from 0.05 M $CdCl_2$ and 0.15 M BMPCl in BMPTFSA was performed at –2.35 and –2.5 V. A grayish black deposit obtained at –2.35 V was confirmed to be metallic Cd by XRD pattern, as shown in Figure 5.7.

Figure 5.8 shows the current density observed during the potentiostatic cathodic reduction on a GC electrode in BMPTFSA containing 0.05 M $CdCl_2$ and 0.15 M BMPCl at –2.35 and –2.5 V. The steady-state current density during the electrodeposition of cadmium at –2.35 and –2.5 V was similar, indicating the reduction rate of $[CdCl_4]^{2-}$ was determined by the diffusion of $[CdCl_4]^{2-}$ to give the limiting current density.

Figure 5.9 shows the SEM images of the electrodeposited Cd obtained from 0.05 M $CdCl_2$ and 0.15 M BMPCl in BMPTFSA at –2.35 and –2.5 V. The morphology of the deposits was found to depend on the deposition potential. Spongy- and/or needle-like deposit was found at –2.35 V. Whereas, granular deposit was obtained at –2.5 V. The crystallite size was calculated for (101) plane using Scherrer equation (eq. 3.8). The crystallite size of the deposit obtained at –2.35 V was found to be larger (61 nm) than that for the deposit obtained at –2.5 V (44.8 nm), indicating the hindrance of crystal growth at more negative potential. Although –2.35 V is sufficiently negative and the cyclic voltammograms indicated the accumulation of BMP^+ cations on the electrode surface at this potential region, at the more negative potential the molar ratio of BMP^+ near the electrode surface is expected to increase in order to compensate the excess negative charge. Such excess crowding of BMP^+ cations near the electrode surface at the more negative potential can hinder the crystal growth. As a result the morphology of the deposit can be changed.

5.3.3 Chemical Deposition of CdSe/Se on Cd Substrate

Figure 5.10 shows the cyclic voltammogram of a GC electrode in BMPTFSA containing 0.02 M $CdCl_2$, 0.02 M $SeCl_4$ and 0.5 M BMPCl at 25°C. Three cathodic current peaks, C1, C2 and C3, were observed in the CV. The cathodic current peak C1 and C2 were assignable to the electroreduction of Se(IV) to Se(0) and Se(0) to Se(-II), respectively. On the other hand, the cathodic current peak C3 was considered due to the electroreduction of Cd(II) to Cd(0). Thus, the cyclic voltammetric result indicates that the electrodeposition of Cd and Se is possible in the system. However, the reduction potential of Se(0) to Se(-II) is more positive than the oxidation potential of Cd(0) to Cd(II) as shown in Figure 5.11. Therefore, a spontaneous chemical reaction is supposed to occur between metallic Cd and Se(IV) species in BMPTFSA in the presence of excess chloride according to the following reactions.

$$\mathrm{Cd(0)} \rightarrow [\mathrm{CdCl_4}]^{2-} + 2e^- \qquad (5.1)$$

$$[\mathrm{SeCl_6}]^{2-} + 6e^- \rightarrow \mathrm{Se(-II)} \qquad (5.2)$$

$$[\mathrm{CdCl_4}]^{2-} + \mathrm{Se(-II)} \rightarrow \mathrm{CdSe} \qquad (5.3)$$

A metallic Cd substrate with a diameter of 14 mm was immersed into BMPTFSA containing 0.02 M $SeCl_4$ and 0.15 M BMPCl at 25°C. After 12 hours, the metallic Cd substrate was removed from the ionic liquid. A thick red film was found on the top of the silvery white metallic Cd substrate. The film was then characterized by XRD. Figure 5.12 shows the XRD patterns of the as deposited film on the Cd substrate. From Figure 5.12, it can be seen that the deposited red film on the Cd substrate gave several diffraction peaks in addition to those for the Cd substrate. The diffraction peaks of metallic Se and CdSe are very close and the observed diffraction peaks could be assigned both to CdSe and/or hexagonal Se. Therefore, the chemically deposited film could be a mixture of CdSe and Se. Thus, it was considered that the chemical deposition of CdSe occurred along with the chemical deposition of Se through the reaction between Se(-II) and $[SeCl_6]^{2-}$.

5.4 Conclusions

Cyclic voltammograms of $[CdCl_4]^{2-}$ species showed an unusual electrochemical behavior, regardless of electrode materials and ionic liquids, probably related to the attraction of BMP^+ on the electrode surface. The cathodic peak potential shifted to the more positive side with elevating temperature, indicating the overpotential for the electroreduction of $[CdCl_4]^{2-}$ decreased at higher temperature possibly due to the ease of nucleation and/or faster charge transfer process. Electroeposition of Cd was also found to be favored on a Cd substrate. The morphology of the deposits obtained by potentiostatic cathodic reduction was found to depend on the applied potential probably related to the influence of potential on the electric double layer structure due to the difference in accumulation of cations on the electrode surface. Metallic Se was found to be chemically deposited on a Cd substrate through the chemical reaction between the Cd substrate and Se(IV) species in BMPTFSA in the presence of excess chloride.

5.5 References

1. C. J. Dymek, G. F. Reynolds, and J. S. Wilkes, *J. Electrochem. Soc.*, **134**, 1658–1663 (1987).
2. M. A. M. Noel and R. A. Osteryoung, *J. Electroanal. Chem.*, **284**, 413–429 (1990).
3. P. Y. Chen and I. W. Sun, *Electrochim. Acta*, **45**, 3163–3170 (2000).
4. R. Hayes, N. Borisenko, M. K. Tam, P. C. Howlett, F. Endres, and R. Atkin, *J. Phys. Chem. C*, **115**, 6855–6863 (2011).
5. S. R. Rubero and S. Baldelli, *J. Phys. Chem. B*, **108**, 15133–15140 (2004).
6. S. Baldelli, *Acc. Chem. Res.*, **41**, 421–431 (2008).
7. R. Wen, B. Rahn, and O. M. Magnussen, *Angew. Chemie - Int. Ed.*, **54**, 6062–6066 (2015).
8. R. Atkin, S. Z. E. Abedin, R. Hayes, L. H. S. Gasparotto, N. Borisenko, and F. Endres, *J. Phys. Chem. C*, **113**, 13266–13272 (2009).
9. M. A. M. Noel and R. A. Osteryoung, *J. Electroanal. Chem. Interfacial Electrochem.*, **293**, 139–150 (1990).
10. P. Y. Chen and I. W. Sun, *Electrochim. Acta*, **45**, 3163–3170 (2000).

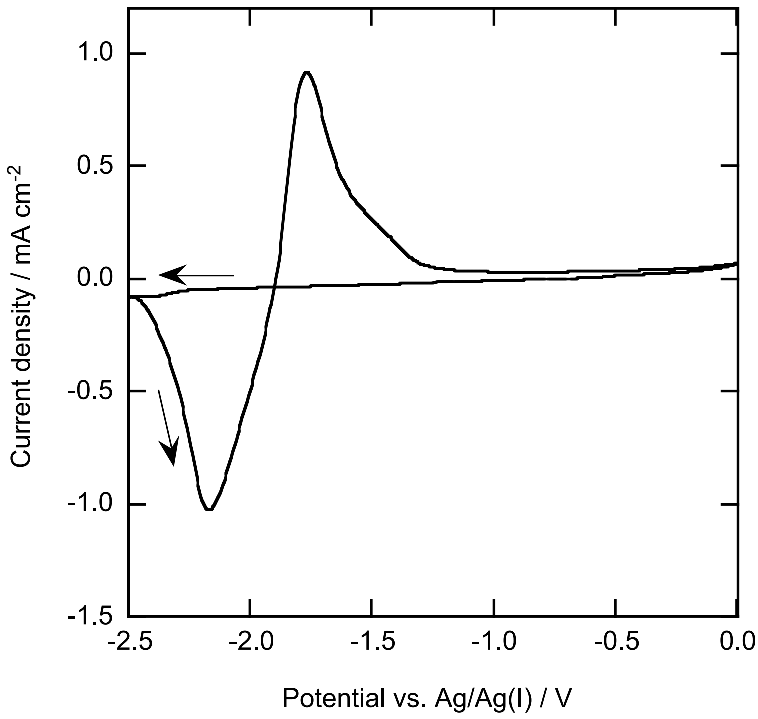

Figure 5.1: Cyclic voltammogram of a GC electrode in BMPTFSA containing 0.05 M $CdCl_2$ and 0.15 M BMPCl at the scan rate of 50 mV s^{-1}. Temperature: 25°C.

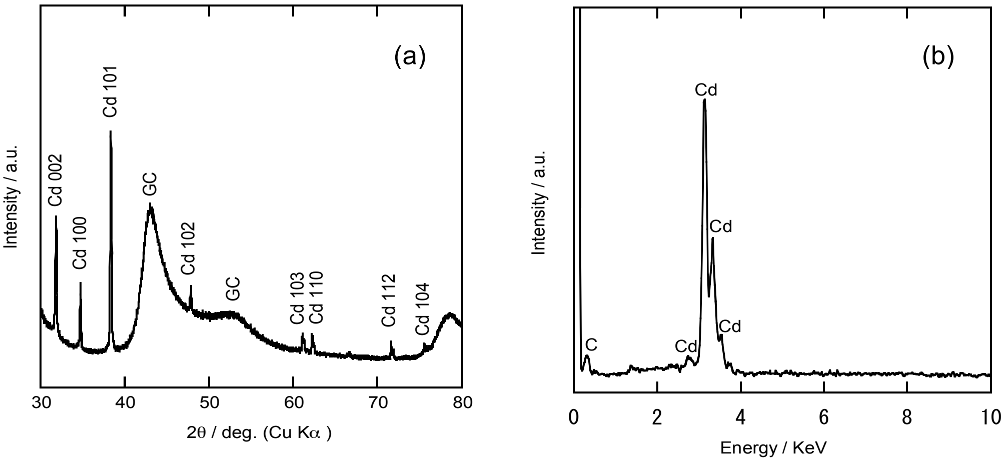

Figure 5.2: (a) XRD pattern and (b) EDX spectrum of the electrodeposit obtained on a GC electrode in BMPTFSA containing 0.05 M $CdCl_2$ and 0.15 M BMPCl. The potential was scanned towards the cathodic direction from the open circuit potential to –2.5 V in the first place, then swept towards the anodic direction and held at –2.2 V. Temperature: 25°C.

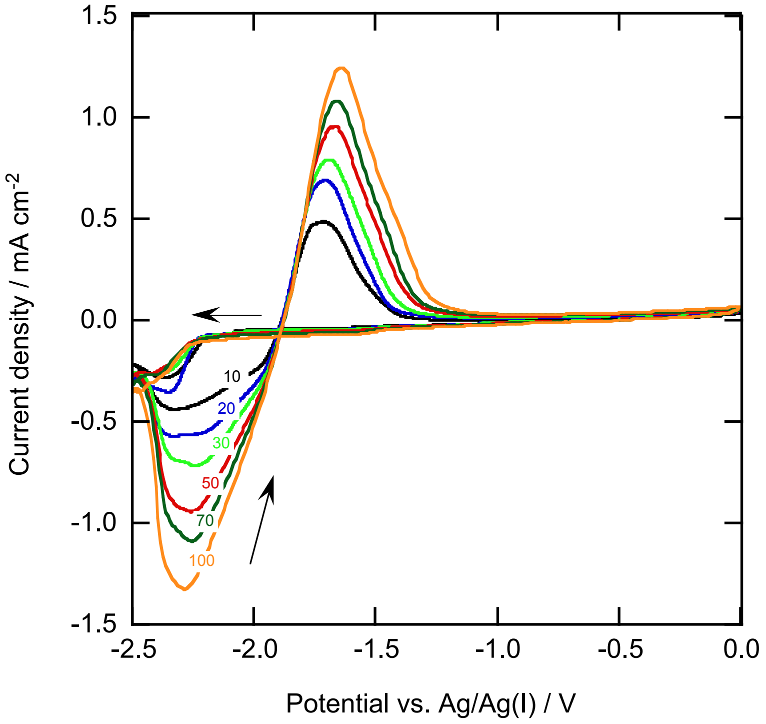

Figure 5.3: Cyclic voltammograms of a GC electrode in BMPTFSA containing 0.05 M $CdCl_2$ and 0.15 M BMPCl at different scan rates. Temperature: 25 °C.

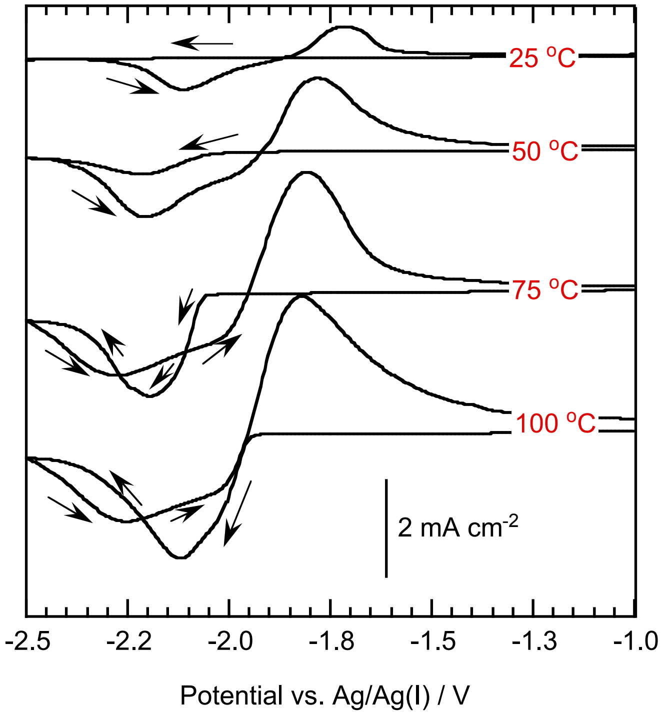

Figure 5.4: Cyclic voltammograms of a GC electrode in BMPTFSA containing 0.05 M $CdCl_2$ and 0.15 M BMPCl at different temperatures. Scan rate: 50 mV s^{-1}.

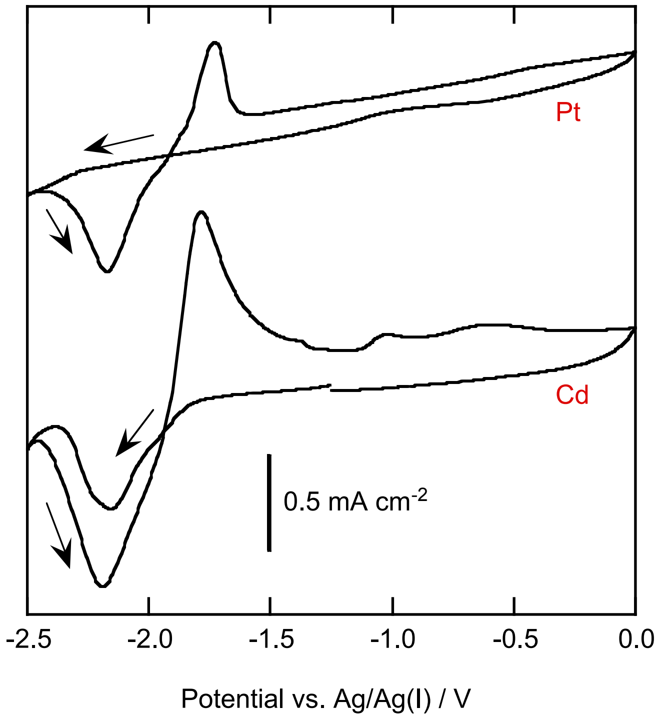

Figure 5.5: Cyclic voltammograms of a Pt and Cd electrode in BMPTFSA containing 0.05 M $CdCl_2$ and 0.15 M BMPCl at the scan rate of 50 mV s^{-1}. Temperature: 25°C.

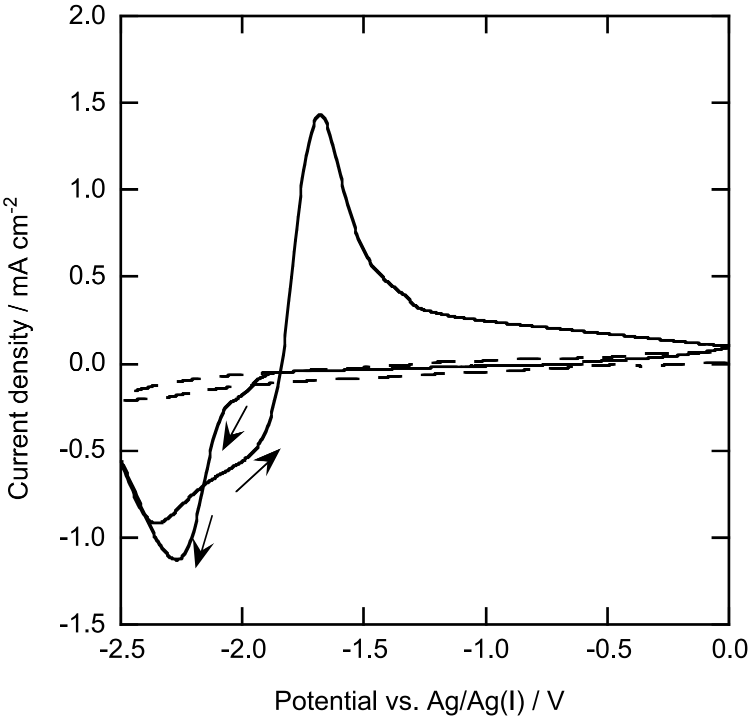

Figure 5.6: Cyclic voltammograms of a GC electrode in BMITFSA containing 0.05 M $CdCl_2$ and 0.15 M BMICl at the scan rate of 50 mV s^{-1}. The dashed line shows the cyclic voltammogram of a GC electrode in neat BMITFSA. Temperature: 25°C.

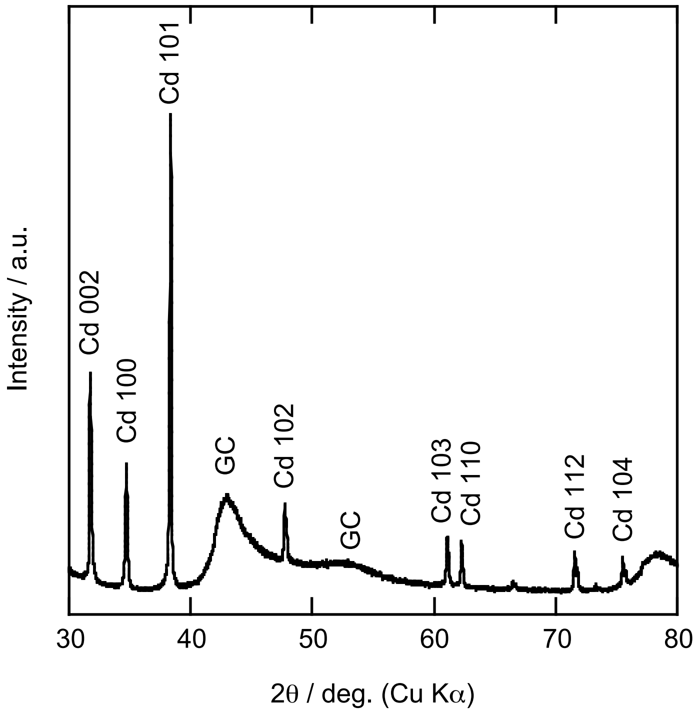

Figure 5.7: XRD pattern of the Cd deposit obtained on a GC electrode in BMPTFSA containing 0.05 M $CdCl_2$ and 0.15 M BMPCl at –2.35 V. Temperature: 25°C.

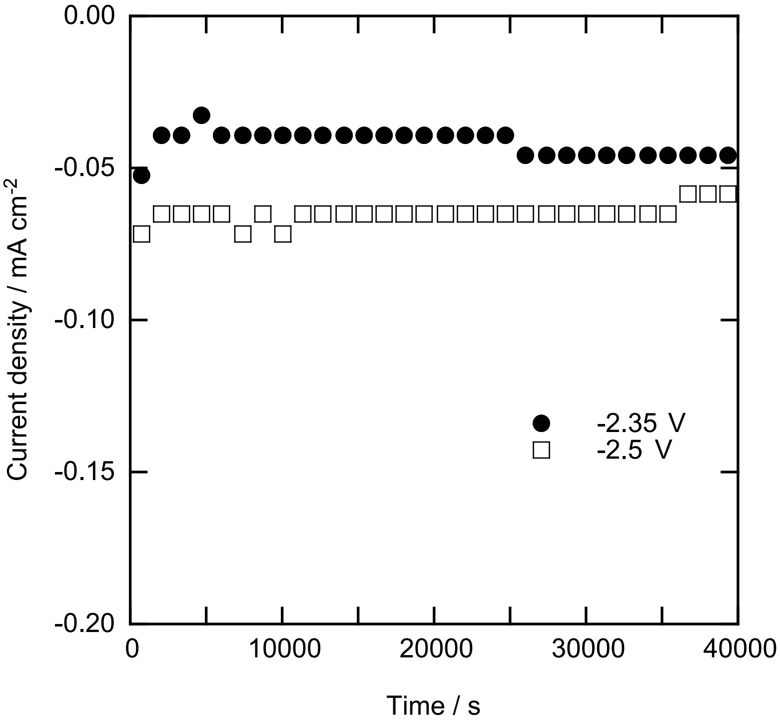

Figure 5.8: Current density during the potentiostatic cathodic reduction on a GC electrode in BMPTFSA containing 0.05 M $CdCl_2$ and 0.15 M BMPCl at –2.35 and –2.5 V. Temperature: 25°C.

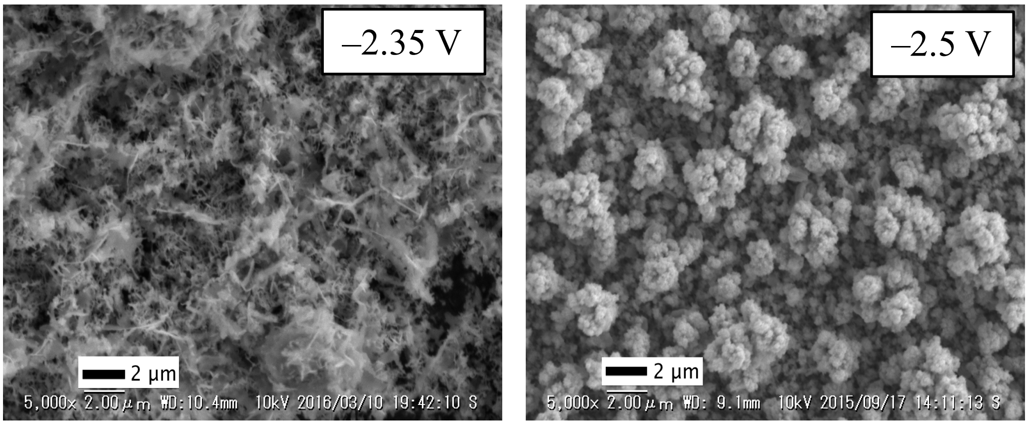

Figure 5.9: SEM images of the electrodeposits Cd obtained on a GC electrode in BMPTFSA containing 0.05 M $CdCl_2$ and 0.15 M BMPCl at –2.35 and –2.5 V. Temperature: 25 ^{o}C.

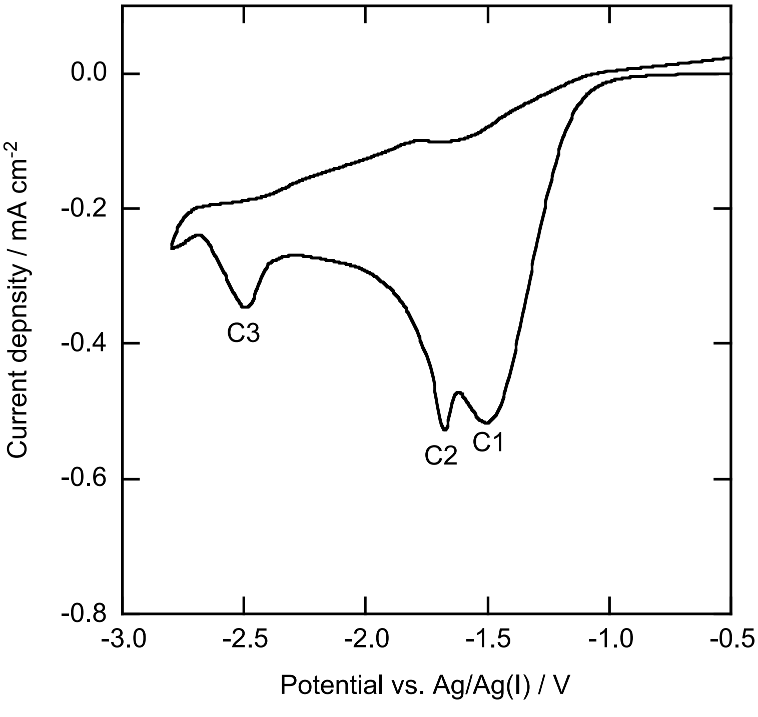

Figure 5.10: Cyclic voltammogram of a GC electrode in BMPTFSA containing 0.02 M $CdCl_2$, 0.02 M $SeCl_4$ and 0.5 M BMPCl at 25°C. Scan rate: 50 mV s^{-1}.

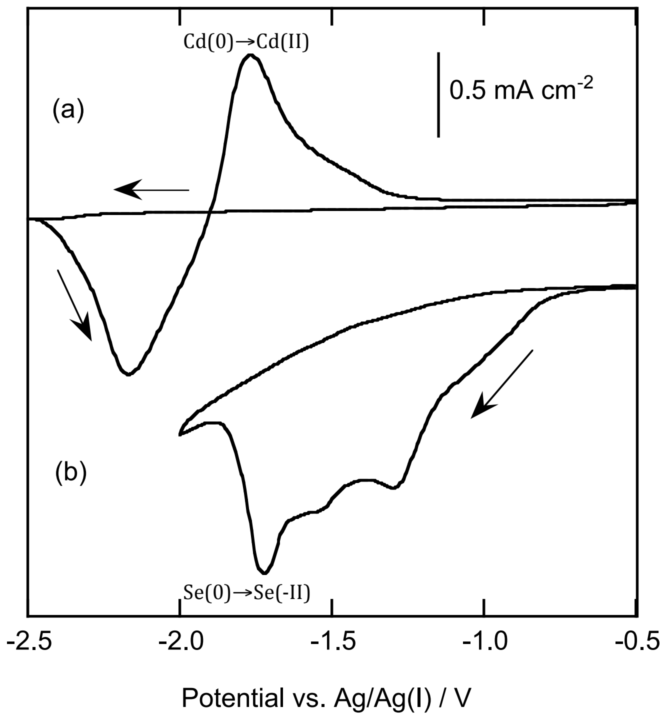

Figure 5.11: Cyclic voltammograms of a GC electrode in BMPTFSA containing (a) 0.05 M $CdCl_2$ and 0.15 M BMPCl and (b) 0.04 M $SeCl_4$ and 0.15 M BMPCl at 25°C. Scan rate: 50 mV s^{-1}.

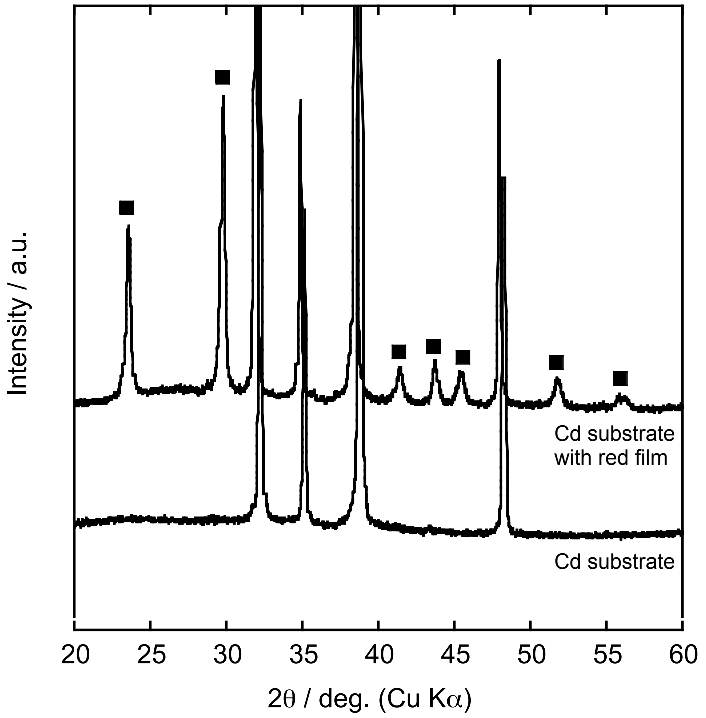

Figure 5.12: XRD patterns of the Cd substrate and the chemically deposited red film on the Cd substrate at 25°C.

Chapter 6

Conclusions and Perspectives

6.1 Conclusions

Electrodeposition of cadmium and selenium was investigated in BMPTFSA. The solvation structure of cadmium and selenium species was also studied in the IL.

$Cd(TFSA)_2$ in BMPTFSA was found to be coordinated by three $TFSA^-$ and probably exists as $[Cd(TFSA)_3]^-$. The electrodeposition of metallic Cd was possible in the IL. The redox potential Cd(II)/Cd in BMPTFSA was more positive than those in other conventional systems, indicating the weak coordination ability of $TFSA^-$. On the other hand, the redox potential of $[CdCl_4]^{2-}$/Cd was close to those reported in the ILs with excess chloride, indicating the redox potentials of chlorocomplexes of metals are little affected by the ions of ILs. The CVs of the Cd(II) species in BMPTFSA in the presence of excess chloride showed interesting unusual electrochemical behavior probably related to the adsorption of BMP^+ on the negatively polarized electrode surface. Moreover, the deposition potential for $[CdCl_4]^{2-}$ was more negative than that of $[Cd(TFSA)_3]^-$, reflecting the difference in the thermodynamic stability of the divalent Cd species with the change of coordination environment.

The electrochemical behavior of selenium species was also found to change in a greater extent with the addition of excess chloride ions. Formation of $[SeCl_6]^{2-}$ was identified in the presence of excess chloride ions. The solubility of $SeCl_4$ was higher in BMPTFSA with excess Cl^- than that in neat BMPTFSA. The electrodeposition of metallic Se was possible in BMPTFSA in both absence and presence of excess chloride. Reduction of Se to Se(–II) was confirmed at the potential more negative than the reduction potential of $[SeCl_6]^{2-}$. However, proportionation reaction of Se(–II) and $[SeCl_6]^{2-}$ led to deposition of Se. In addition, chemical deposition of CdSe along with the formation of metallic Se was suggested on a Cd substrate through the chemical reaction between the Cd substrate and $[SeCl_6]^{2-}$ in BMPTFSA in the presence of excess chloride.

On the other hand, morphology and crystal structure of the deposits were found to change with the electrodeposition parameters. Specially, nucleation process and morphology of the cadmium electrodeposits were found to be affected by the applied potential under diffusion-controlled region probably due to the difference in accumulation of cations of IL on the negatively polarized electrode surface. It is worth to mention that for ILs, the electrode-electrolyte interfacial structure is exclusively different from that of a conventional solution system. In the case of conventional solution, the electrode surface is expected to contact with solvent molecules whereas, in the case of ILs, the electrode surface is expected to contact with the cations and anions of ILs, as shown in the Figure 6.1. Therefore, electrodeposition processes like diffusion of ad-atoms, nucleation, and crystallization are considered to be significantly affected by the accumulated ions of the IL. In addition, the composition of the cations and anions will also change depending on the electrode potential, as shown in Figure 6.2. Therefore, a change in the electric double layer structure due to the difference in the population of cations and anions of IL with the applied potential could be the key factor behind the morphological variation. Furthermore, formation of Cd nanoparticles and their dispersion into the IL at the more negative potential region was possible due to the strong accumulation of cations of IL on the electrode surface.

The results revealed that BMPTFSA can be a promising electrolyte not only for the electrodeposition of cadmium and selenium but also for other metals. Moreover, this IL can be a medium for electrochemical preparation of various metals nanoparticles without any additional stabilizer.

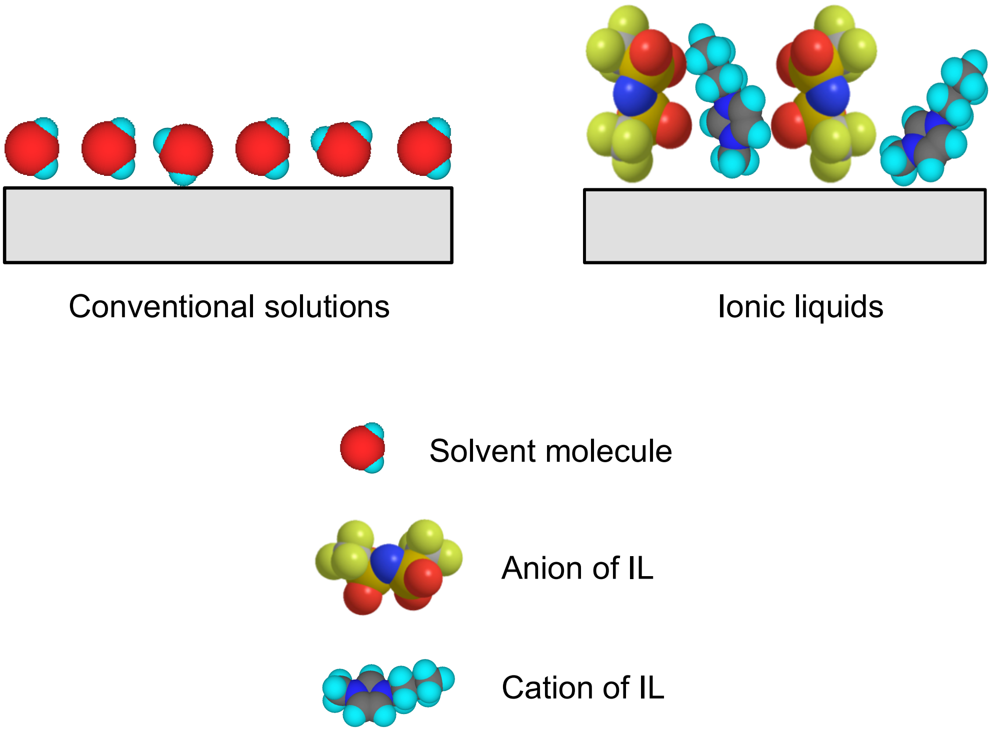

Figure 6.1: Schematic illustration of the electrode-electrolyte interface in conventional solutions and ionic liquids.

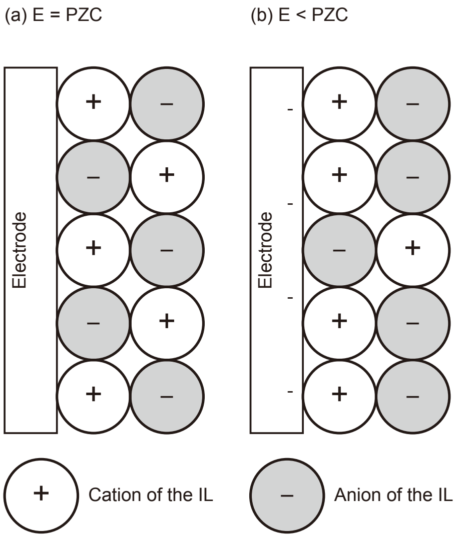

PZC=Potential of zero charge

Figure 6.2: Schematic illustration of the change of electric double layer structure with potential in ionic liquid system.

6.2 Perspectives

Electrodeposition of cadmium and selenium was successfully performed in BMPTFSA. However, further detail investigation of the effect of several electrodeposition parameters on the morphology and crystal structure of the deposits is necessary in order to optimize the metal deposition condition in BMPTFSA.

In the present study, electroreduction process was found to be significantly affected by the solvation states of the metal ions. Therefore, in order to use BMPTFSA for electrodeposition and/or electroplating of metals, it is important to control the solvation states of the metal ions dissolved in BMPTFSA. It is also worth to mention that the accumulation of BMP^+ often makes it difficult to obtain smooth and compact electrodeposits on substrates due to hindrance of nucleation and crystal growth. In that case, the effects of some organic additives, *e.g.* acetone and acetonitrile, that could form metal ion complexes with overall positive charge in BMPTFSA, would be interesting to examine in order to obtain smooth films of the deposit. In such a system, the metal ion complex with an overall positive charge has the possibility to approach at a nearer position to the electrode surface compared to that of a metal ion complex with an overall negative charge. The presence of metal ion complexes with overall positive charge to the electrode surface will decrease in the population of BMP^+ near the electrode surface. A decreased population of BMP^+ near the electrode surface may favor the crystal growth process as the presence of BMP^+ on the electrode surface inhibits the crystal growth process. Therefore, the favorable crystal growth environment in the presence of such organic additives may give smooth and compact metal films.

On the other hand, some additives, *e.g.* coumarin, benzyl alcohol, and thiourea, are known to be preferentially adsorbed on the peaks rather than recesses of the electrode surface. The use of such additives for obtaining flat and smooth metal films has been known to be particularly beneficial. Therefore, electrodeposition of metals in BMPTFSA should be studied in the presence of such additives.

In the present study, electrodeposition has been performed in constant current and constant potential modes. Besides, pulse electrodeposition technique is known as a useful technique to improve the morphology. Therefore, electrodeposition of metals in BMPTFSA should also be investigated using pulse electrodeposition technique. In pulse electrodeposition technique, very high instantaneous current densities can be attained. The high instantaneous current density therefore could enhance the nucleation rate. Moreover, a continuous change of the concentration of electroactive species near the electrode surface during the pulse electrodeposition may lead to a homogeneous distribution of the electrodeposits. Therefore, pulse plating of metals in BMPTFSA could be a potential method to improve the morphology of the deposits.

In general, metal deposition in ILs is greatly affected by the viscosity of the ILs. At high temperature, lowering of viscosity of ILs will increase the mobility of the metal species as well as facilitate the crystal growth process. It is to be mentioned that less volatility of ILs is advantageous for electrodeposition of metals at higher temperature since no change in the composition of electrolytes is expected in contrast to conventional solutions. Therefore, electrodeposition of metals in BMPTFSA could be investigated at high temperature.

In BMPTFSA, electrode reactions occurring at a negative potential region were found to be strongly affected by the accumulation of BMP^+ on the electrode surface. Such accumulation of BMP^+ is considered utilizable for electrochemical preparation of metal nanoparticles. Therefore, it is also worth to examine the preparation of different metal nanoparticles in BMPTFSA.

Publications

1. Articles on periodicals (related to thesis)

1. Shimul Saha, Naoki Tachikawa, Kazuki Yoshii, and Yasushi Katayama; Electrodeposition of selenium in a hydrophobic room-temperature ionic liquid, *J. Electrochem. Soc.*, **163**, D259–D264 (2016).
2. Shimul Saha, Naoki Tachikawa, Kazuki Yoshii, and Yasushi Katayama; Electrochemical Behavior of Cadmium in 1-Butyl-1- methylpyrrolidinium Bis(trifluoromethylsulfonyl)amide Room-temperature Ionic Liquid, *Electrochim. Acta*, **183,** 42–48 (2015).

2. Other articles on periodicals

1. Shimul Saha, Sharmin Sultana, Md. Mominul Islam, M. Muhibur Rahman, M. Yousuf A. Mollah, and Md. Abu Bin Hasan Susan; Electrodeposition of cobalt with tunable morphology from reverse micellar solution, *Ionics*, **20**, 1175–1181 (2014).
2. Sharmin Sultana, Shimul Saha, Md. Mominul Islam, M. Muhibur Rahman, M. Yousuf A. Mollah, and Md. Abu Bin Hasan Susan; Electrodeposition of nickel from reverse micellar solutions of cetyltrimethylammonium bromide, *J. Electrochem. Soc.*, **160**, D524-D529 (2013).
3. Md. Abu Bin Hasan Susan, Shimul Saha, S. Ahmed, F. Begum, M. Muhibur Rahman, and M. Yousuf A. Mollah; Electrodeposition of cobalt from a hydrophilic ionic liquid at ambient condition, *Mater. Res. Innov.*, **16**, 345–349 (2012).

3. Presentations at international conferences

1. Shimul Saha*, Naoki Tachikawa, Kazuki Yoshii, Luca Magagnin, and Yasushi Katayama; Electrochemical Behavior of Cadmium Chloro-complex in a Hydrophobic Room-temperature Ionic Liquid, 16th Asian Chemical Congress, Dhaka, Bangladesh, March 16-19 (2016).
2. Shimul Saha*, Naoki Tachikawa, Kazuki Yoshii, and Yasushi Katayama; Electrochemical Behavior of Divalent Cadmium Species in a Room-temperature

Ionic Liquid, 6th International Congress on Ionic Liquids, Jeju, Korea, June 16-20 (2015).

3. Shimul Saha*, Takuho Taguchi, Naoki Tachikawa, Kazuki Yoshii, and Yasushi Katayama; Electrochemical Behavior of Cadmium in 1-Butyl-1-methylpyrrolidinium Bis(trifluoromethylsulfonyl)amide Room-temperature Ionic Liquid, 10th International Symposium on Electrochemical Micro and Nanosystem Technology, Okinawa, Japan, November 5-8 (2014).

4. Presentations at domestic meetings

1. Shimul Saha*, Naoki Tachikawa, Kazuki Yoshii, Luca Magagnin, and Yasushi Katayama; Electrochemical Behavior of Cadmium Chloro-Complex in an Amide-type Ionic Liquid, The 47th symposium on Molten Salt Chemistry, Kobe, Japan, October 28-29 (2015).
2. Shimul Saha*, Takuho Taguchi, Naoki Tachikawa, Kazuki Yoshii, and Yasushi Katayama; Influence of Current Density and Potential on Electrodeposition of Cadmium and Formation of Cadmium Nano-particles in an Amide-type Ionic Liquid, 82nd Spring Meeting of The Electrochemical Society of Japan, Yokohama, Japan, March 15-17 (2015).
3. Shimul Saha*, Takuho Taguchi, Naoki Tachikawa, Kazuki Yoshii, and Yasushi Katayama; Electrodeposition of Cadmium from 1-Butyl-1-methylpyrrolidinium Bis(trifluoromethylsulfonyl)amide Ionic Liquid, Fall Meeting of The Electrochemical Society of Japan, Hokkaido, Japan, September 27-28 (2014).

Acknowledgements

I would like to express my gratitude to my supervisor, **Professor Yasushi KATAYAMA**, Department of Applied Chemistry, Faculty of Science and Technology, Keio University for his guidance and cooperation during my graduate studies at the Keio University. I am grateful to him for his patience and instructions with the mistakes in my papers and thesis. I am thankful to **Emeritus Professor Takashi MIURA** for his proper advice to make my life comfortable in Japan.

I would like to express my sincere gratitude to **Research Associate Kazuki YOSHII,** Department of Applied Chemistry, Faculty of Science and Technology, Keio University and **Dr. Naoki TACHIKAWA** to help me throughout this study. I am very grateful to the all members in my laboratory to help me not only in my study but also in my daily life.

I would like to acknowledge four judges, **Professor Hiroaki IMAI**, **Professor Naoki YOSHIOKA**, **Professor Takashi YAMAMOTO**, and **Professor Luca Magagnin**, for their thoughtful suggestions and comments on my thesis.

I am highly grateful to the “Ministry of Education, Culture, Sport, Science and Technology (MEXT)” for Japanese Government Scholarship. I also wish to thank the Keio University for exemption of tuition fee for my doctoral course. I would like to acknowledge “Impulsing Paradigm Change through Disruptive Technologies (ImPACT)” program from Cabinet Office, Government of Japan and “Keio Leading-edge Laboratory of Science and Technology (KLL)” for their financial support.

Finally, I would like to thank my respected parents for their faith on me and allowing me to be as ambitious as I wanted.